Physics Department, University of Neuchâtel

EXPERIMENTAL STUDY OF NEUTRINO-ELECTRON SCATTERING AT LOW ENERGY WITH THE MUNU EXPERIMENT

Zornitza Daraktchieva

Physics Department, University of Neuchâtel

EXPERIMENTAL STUDY OF NEUTRINO-ELECTRON SCATTERING AT LOW ENERGY WITH THE MUNU EXPERIMENT

PhD thesis by

Zornitza DARAKTCHIEVA
Master of Science, University of Sofia, Bulgaria
Bulgarian nationality

presented at
the Faculty of Sciences, University of Neuchâtel
for the Degree of Doctor ès Sciences

accepted by proposition of the jury:
Prof. J.-L. Vuilleumier, thesis advisor
Dr. C. Broggini
Prof. J. Busto
Dr. D. Twerenbold
Prof. V. Zacek

Neuchâtel, October 2004

IMPRIMATUR POUR LA THESE

Experimental study of neutrino-electron scattering at low energy with the MUNU experiment

Mme Zornitza DARAKTCHIEVA

UNIVERSITE DE NEUCHATEL

FACULTE DES SCIENCES

La Faculté des sciences de l'Université de Neuchâtel, sur le rapport des membres du jury

MM. J.-L. Vuilleumier (directeur de thèse), D. Twerenbold, C. Broggini (Padoue I) et J. Busto (Marseille)

autorise l'impression de la présente thèse.

Neuchâtel, le 26 octobre 2004

La doyenne:

Prof. M. Rahier

to my husband Maren, my daughter Jasmin and my parents

List of contents

Introduction

Neutrinos are the most mysterious particles in the Universe with their tiny masses, small magnetic moments and the possibilities to oscillate.

The neutrino was proposed as a solution to the beta decay puzzle in 1930 by Wolfgang Pauli. The physicists at these days were embarrassed by the nuclear beta decay, in which a neutron transforms into a proton and emits an electron in the same time. If it was two-body decay, the laws of energy and momentum conservation predicted a monochromatic electron peak. Surprise came to the physicist since the energy of the radiated electron was found to follow a continuous spectrum. In order to conserve the law of conservation of energy Pauli postulated a new neutral particle with spin ½, later called neutrino by Enrico Fermi. At this time nobody believed that the neutrino is more tha an elegant solution of the problem.

Neutrinos interact so weakly with the matter that even Pauli suggested that nobody could detect them at all. In 1956 however the antineutrinos from a nuclear reactor were detected by Cowan and Reines [1].

Since then neutrinos have revealed a small part of their nature.

The Standard Model, which was formulated in the 60's postulates 6 neutrino flavours: electron neutrino and antineutrino, muon neutrino and it antineutrino and tau neutrino and it anti neutrino. Within the Standard Model the neutrinos are massless, interact only via weak interactions with matter and have no magnetic moments.

The discovery of neutrino oscillations, predicted by Pontecorvo in the late 50's marked a new era in Neutrino Physics. It was demonstrated in series of experiments that the neutrinos oscillate: atmospheric neutrinos (1998 the Super-Kamiokande experiment, [2]), solar neutrinos 2001 (SNO [3] and Super Kamiokande [4] experiments) and reactor neutrinos (2003 KamLAND experiment [5]).

Why are neutrino oscillations so important?

The powerful demonstration of neutrino oscillations from the atmospheric, solar and reactor neutrinos implies finite neutrino masses and mixing. Up to now their exact values and physical origin are not known. Experimental studies of the intrinsic neutrino properties and interactions can reveal the fundamental nature of the neutrino.

If neutrinos do possess masses the question of the magnetic moments of the neutrinos arises immediately. The fundamental magnetic moments are associated with the mass eigenstates as it is shown in [6-9].

The neutrino magnetic moment matrix μ_{jk} (j,k =1,2,3) can either be Dirac like, in which both static and transition moments may be non zero, or Majorana like, in which case the transition moments can be possible, while the static moments are zero.

Astrophysical observations suggest that it is more probable that the magnetic moment matrix is Dirac like than it is Majorana like [10-13].

The best existing limits on the neutrino magnetic moment are coming from the astrophysics and cosmology but are model dependent. For example, stellar cooling, involving Dirac and Majorana neutrinos requires $\mu_\nu < 1.10^{-11}\ \mu_B$ [11], while ^{4}He nucleosynthesis admits $\mu_\nu < 5.10^{-11}\ \mu_B$ [10]. The absence of neutrinos from the SN1987A is interpreted as a further restriction and is used to set the limits: $\mu_\nu < 2.10^{-12}\ \mu_B$ [14], $\mu_\nu < 1.10^{-13}\ \mu_B$ [13] and $\mu_\nu < 5.10^{-13}\ \mu_B$ [12]. The data analyses of SN1987A however depend on the assumption that only Dirac neutrinos are involved. The other astrophysical limit $\mu_\nu < 2.10^{-12}\ \mu_B$ is coming from the luminosity of red giant [15] and also depends on various parameters.

Therefore the direct laboratory measurements are preferable, because they are under better control and could provide unambiguous information on neutrino magnetic moment.

The experimental study of $(\nu_e - e)$ or $(\overline{\nu_e} - e)$ scattering could provide more information on the electromagnetic properties of the neutrino. Any deviation of the measured cross-section from the one expected with weak interaction alone can be connected with a new Physics.

CHAPTER I

MUNU experiment

I.1. Theoretical motivations of the experiment

The neutrino magnetic moment could be studied by electron antineutrino electron $\left(\overline{\nu_e} - e\right)$ elastic scattering. This process is fundamental, since it provides important information on neutrino properties and was measured by Reines group for the first time [16]

The MUNU [17] experiment probes the existence of a magnetic moment by comparing the measured energy spectrum of the recoil electrons, with the one that takes into account the weak and electromagnetic interactions.

The differential cross section for the $\left(\overline{\nu_e} - e\right)$ scattering is given by

$$\frac{d\sigma}{dT_e} = \frac{G_F{}^2 m_e}{2\pi}\left[\left(g_V + g_A\right)^2 + \left(g_V - g_A\right)^2\left(1 - \frac{T_e}{E_\nu}\right)^2 + \left(g_A{}^2 - g_V{}^2\right)\frac{m_e T_e}{E_\nu{}^2}\right] + \tag{1}$$

$$+ \frac{\pi\alpha^2\mu_\nu{}^2}{m_e{}^2}\frac{1 - \frac{T_e}{E_\nu}}{T_e} \tag{1}$$

In (1) the first line is the weak contribution to the cross section (from the Standard model alone) [18], while the second line is the contribution from the magnetic moment [19]. Here E_ν is the incident neutrino energy, T_e is the electron recoil energy, μ_ν is the magnetic moment of the neutrino, and the electroweak coupling constants are given by

$$g_V = 2\sin^2\theta_W + \frac{1}{2}; \quad \text{where} \quad \theta_W = 29°$$

$$g_A = -\frac{1}{2}$$

The relative contribution of the magnetic moment term increases with a decrease of both the neutrino energy and the electron recoil energy. Therefore it is important to have a low neutrino energy source combined with a low electron detection threshold.

The measured magnetic moment μ_e depends on the mixing matrix U_{ek} and on the propagation properties of neutrinos (if the distance L from the source to the detector is large). For vacuum oscillations one may write (2):

$$(\mu_e)^2 = \sum_j \left| \sum_k U_{ek} e^{ip_k L} \mu_{jk} \right|^2 \tag{2}$$

with $p_k \cong E_\nu - \frac{m_k^2}{2E_\nu}$ the moment of neutrino ν_k with mass m_k.

For reactor experiments, the distance between source and detector is L ~ 0 and the measured magnetic moment μ_{reac} depends on the mixing matrixes U_{ek} (neutrino mixing matrix) and μ_{jk} (magnetic moment matrix) alone, and it is given by (3).

$$(\mu_{reac})^2 = \sum_j \left| \sum_k U_{ek} \mu_{jk} \right|^2 \tag{3}$$

I.2. Nuclear reactor as a neutrino source

I.2.1. Reactor in Bugey (France)

The electron antineutrino source of the MUNU experiment is a nuclear reactor, situated in Bugey (France) with an average power of 2775 MWth. The reactor operates for a period of 11 months, followed by a shutdown of 1 month. It emits neutrinos in the energy region 0÷8 MeV.

The neutrinos are mostly produced in the beta decay of the fission fragments of the following four major fissile elements in the fuel, with an average composition in the beginning of the operating period: ^{235}U (54%), ^{239}Pu (33%), ^{241}Pu (6%) and ^{238}U (7%).

How are neutrinos produced in ^{235}U decay chain for example? When ^{235}U captures a thermal neutron, a highly exited compound nucleus $^{236}U^{*}$ is formed.

$^{235}\mathrm{U} + \mathrm{n} \rightarrow {}^{236}\mathrm{U}^{*}$

The excited nucleus $^{236}U^{*}$ predominantly undergoes fission (in 85% of the cases) for instance.

$^{236}\mathrm{U}^{*} \rightarrow {}^{139}\mathrm{La} + {}^{95}\mathrm{Mo} + 2\mathrm{n}$

The most probable immediate products of this process are e.g. the two fission fragments: ^{139}La and ^{95}Mo. Each of these fragments undergoes about three β decay before becoming a stable nuclide. In each β decay one neutrino is produced. This process gives 6 electron antineutrinos per fission. For other fissile elements, for instance, neutrinos are also produced by beta decay of their fission fragments. The total flux of neutrinos in the core of the reactor is about $5.10^{20}\,\overline{\nu_e}$ per second.

I.2.2. Reactor neutrino spectrum

Good knowledge of reactor spectrum is of great importance for the MUNU experiment, since we use the reactor antineutrino spectrum for our calculations of the expected recoil electron spectrum.

According to [20, 21] the spectrum of reactor antineutrinos is given by (4)

$$\rho(E_\nu) = {}^{F}\rho(E_\nu) + {}^{C}\rho(E_\nu) \qquad (4)$$

In (4) the first term describes the emission from the fission fragments, while the second one corresponds to the radiative capture of fast neutrons by various nuclei, including the fission fragments.

The component ${}^{F}\rho(E_\nu)$ is due to beta decay of the fission fragments of ^{235}U, ^{239}Pu, ^{241}Pu and ^{238}U.

The second term in (4) ${}^{C}\rho(E_\nu)$ can be broken down to the sum ${}^{C}\rho = {}^{H}\rho + \Delta^{F}\rho$, where ${}^{H}\rho$ corresponds to the decay of the heavy isotopes ^{239}U, ^{239}Np and ^{237}U, produced during the reactor operating period, while $\Delta^{F}\rho$ corresponds to the spectrum of fission fragments for neutron captures by these fragments.

At energy above 1.5 MeV the neutrinos are predominantly produced in the beta decay of the fission fragments of ^{235}U, ^{239}Pu, ^{241}Pu and ^{238}U. This part of the neutrino spectrum could be reconstructed by using a procedure described in [22].

Above 1.8 MeV there are measurements of the neutrino spectrum at reactors by using $\bar{\nu}_e + p \longrightarrow e^+ + n$ reaction. These measurements show good agreement with the predictions [23-28].

On the contrary, the low part of the neutrino spectrum with neutrino energy (E_ν) below 2 MeV, also called the 'soft' part of the spectrum, has never been measured and there exist only less precise calculations which differ from one another up to 30 % [19, 21, 29]. The reason for this deviation could be found in the underestimation of the significant contribution from the ${}^{239}\text{U}\rightarrow{}^{239}\text{Np}\rightarrow{}^{239}\text{Pu}$ chain produced via fast neutron radiative capture in ^{238}U at energy below 1.5 MeV.

$$
\begin{aligned}
{}^{238}\text{U} + \text{n} &\rightarrow {}^{239}\text{U} + \gamma \\
{}^{239}\text{U} &\rightarrow {}^{239}\text{Np} + \text{e}^- + \bar{\nu}_e \\
{}^{239}\text{Np} &\rightarrow {}^{239}\text{Pu} + \text{e}^- + \bar{\nu}_e
\end{aligned}
$$

The calculations of the spectra of the four fissile isotopes at $E_\nu < 2$ MeV calculated by Vogel and Engel [19] are presented in Fig.1.

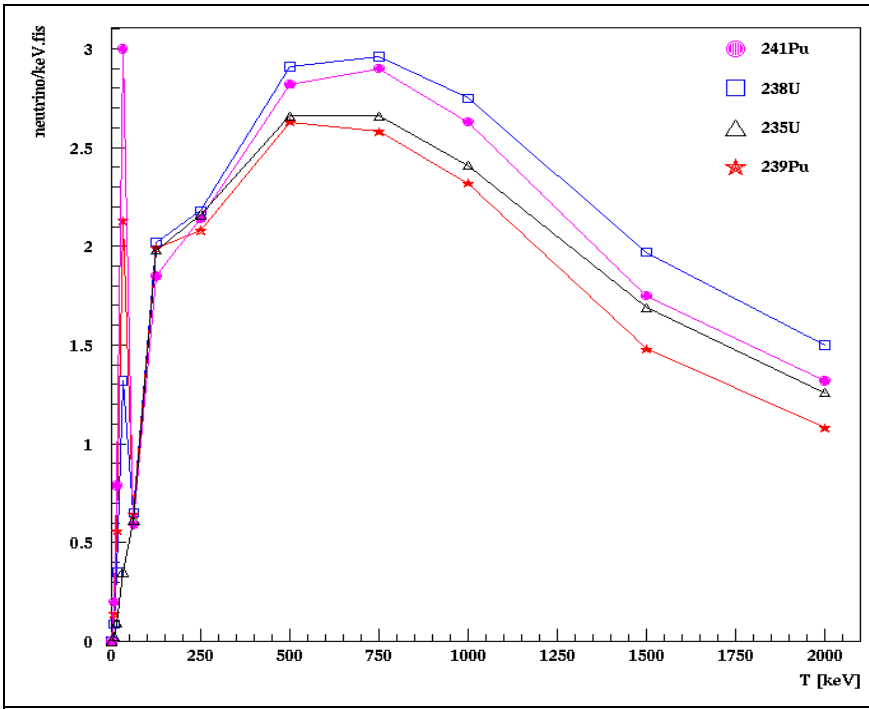

Fig.1.The spectra of 4 fissile elements calculated by Vogel and Engel.

The total reactor neutrino spectrum for $E_\nu < 2$ MeV, calculated by Kopeikin [21] by taking into account the neutron capture in ^{238}U, is presented in Fig.2.

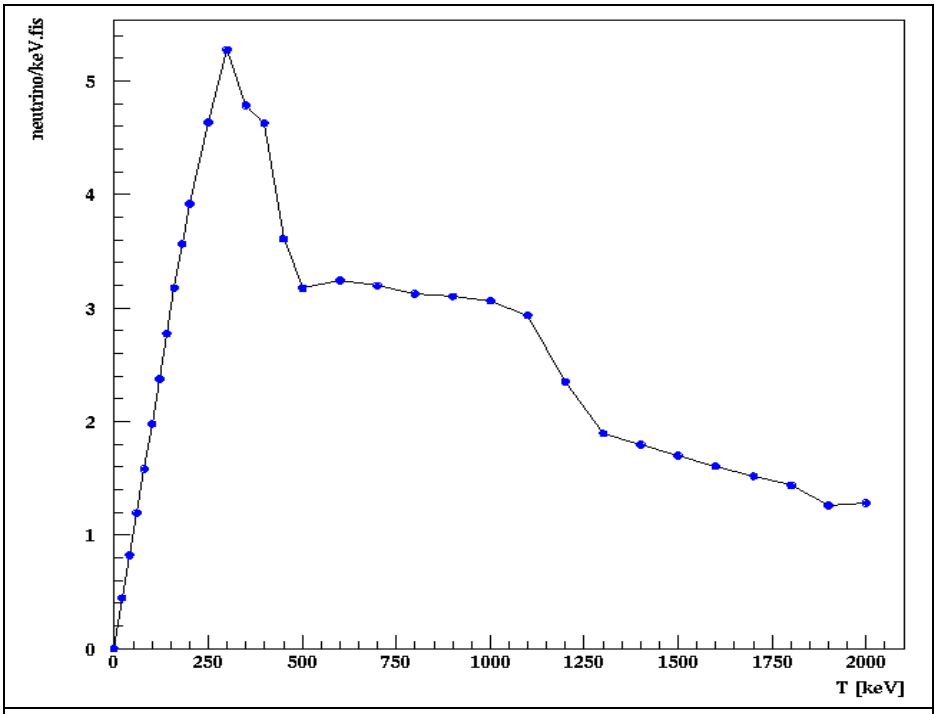

Fig.2. The reactor antineutrino spectrum, calculated by Kopeikin.

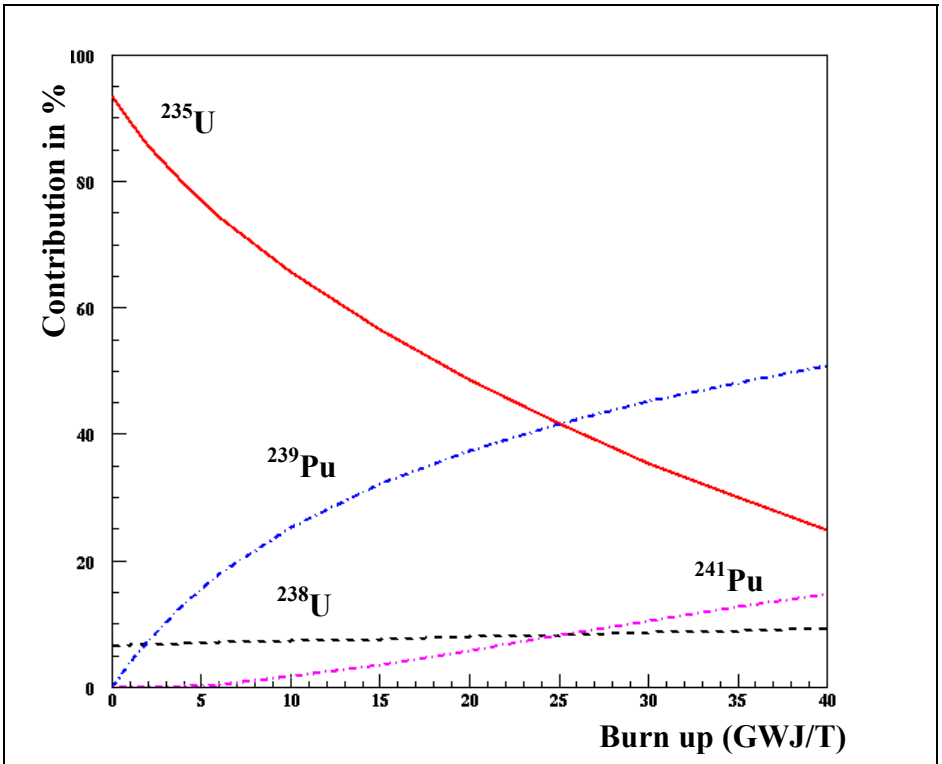

Fig.3.Contributions of the four fissile isotopes to the total fission number as a function of burn up.

The composition of the four major fissile elements in the reactor core varies with times (Fig.3) and the burning of ^{235}U and the accumulation of ^{239}Pu change the total spectrum during the reactor operation period. The time variations of the fuel are given in [30].

The situation is complicated further because of the fact that at low energies the neutrino spectrum has a strong time dependence; it never comes to saturation and is does not vanish after the reactor is shut down [31, 32].

The reactor neutrino spectrum of the MUNU experiment is calculated [33] by taking into account the following parameters(see fig.4):

- 2775 MWth reactor average power;
- fission fragments average contribution over an annual reactor cycle: ^{235}U (60 %), ^{239}Pu (28 %), ^{241}Pu (5 %), ^{238}U (7 %);
- additional neutron capture in ^{238}U.

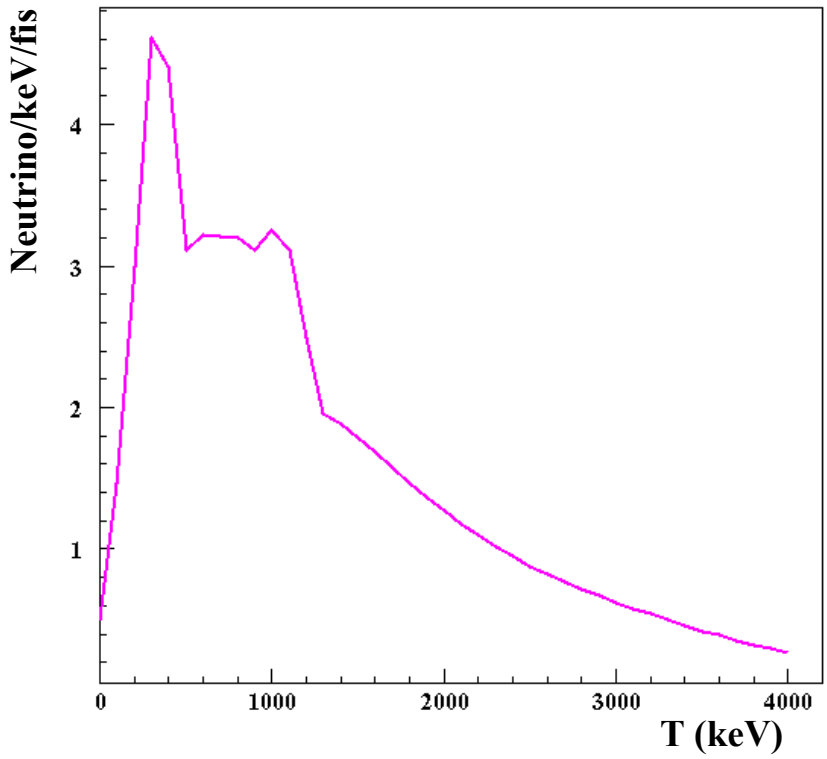

Fig.4. The calculated reactor neutrino spectrum of MUNU experiment.

I.3. MUNU detector

The MUNU Collaboration has built a detector in which the topology of events is registered. Due to the tracking capability of the detector we can measure not only the recoil energy of the electron, but also for the first time its scattering angle. The advantage of the latter is a better event selection and background rejection on-line. The background being isotropic or at least symmetric with regards to reactor axis, while the signal is only in the forward direction. Additionally, we can reconstruct the incoming neutrino energy by using the recoil energy of electrons together with its scattering angle.

Technical details of the MUNU detector have already been present [17, 34].

In this part we give a brief description of the detector, which is made from radiochemically clean materials and is situated at 18 m from the reactor core. The lab has an overburden of steel, concrete and water corresponding to 20 meter water equivalent. The neutrino flux in the lab is found to be 10^{13} ν/cm^2. s.

The detector consists of tree parts: a Time Projection Chamber (TPC), an anti-Compton detector and Passive Shielding. The picture of the MUNU detector is shown in Fig. 5.

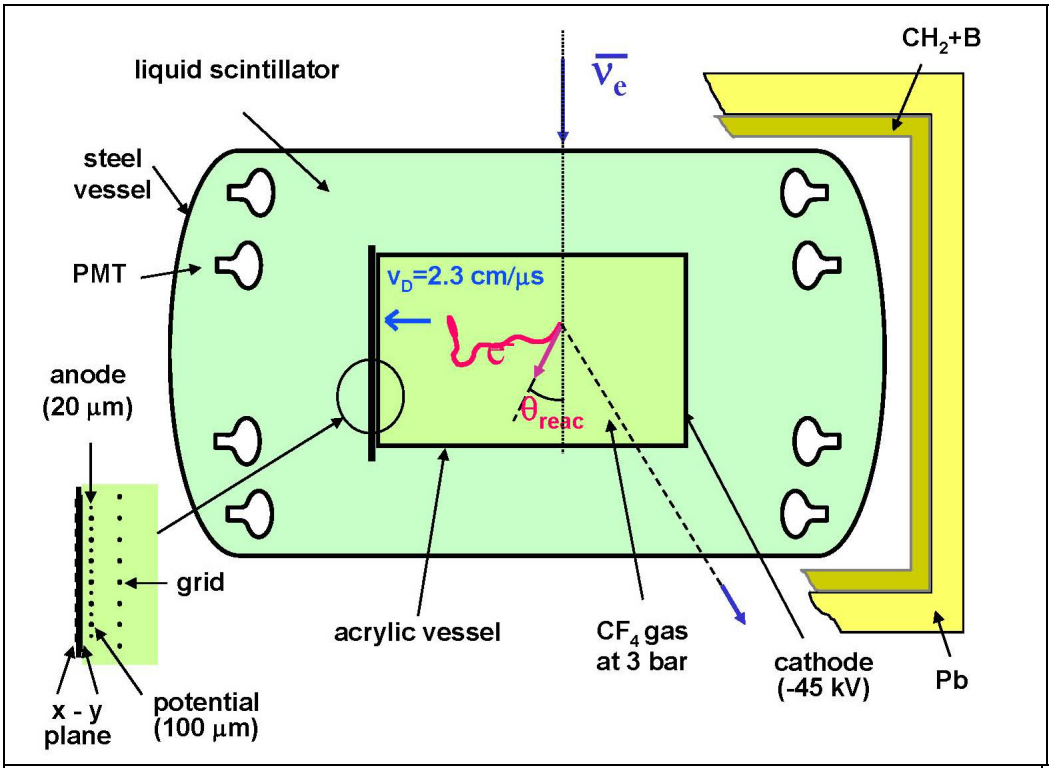

Fig. 5. MUNU Detector

I.3.1 Time Projection Chamber (TPC)

The main part of the detector is a Time Projection Chamber filled with 11.4 kg of CF4 gas at 3 bar pressure (3.8 kg of CF4 at 1 bar pressure). The gas was selected, because of its high electron density (1.06 x 10^{21} electrons per cm^3 at STP), good drifting properties, low Z (which reduces multiple scattering) and its absence of free protons, which eliminates backgrounds from the $\bar{\nu}_e + p \longrightarrow e^+ + n$ reaction.

The gas is contained in a cylindrical, transparent acrylic vessel, with an active volume of $1m^3$, a length of 162 cm and a diameter of 90 cm (Fig.6). The TPC is orthogonal to the neutrino flux of the reactor and is absolutely symmetric with respect to the reactor-detector axis.

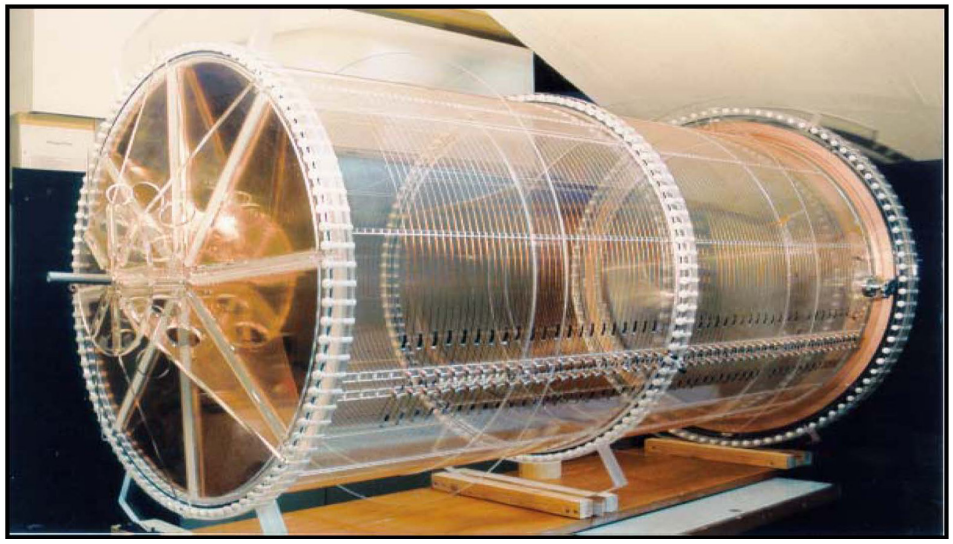

Fig.6. Acrylic vessel and field shaping rings are shown

At one side of the TPC, a cathode is mounted and held at a negative high voltage of up to −80 keV. At the other side of the TPC, an anode Multi Wire Proportional Plane is mounted, which consists of grid wires, anode wires and a *x*-*y* pick up plane (with perpendicular *x* and *y* stripes). The anode plane contains anode wires with a spacing of 4.95 mm. The anode wires (20 μm ϕ each) are separated by potential wires (100 μm ϕ each).

The *x*-*y* plane (Fig.7) is located at 3 mm behind the anode plane. There are 512 strips, 256 *x* and 256 *y* in total. The spacing between the strips is 3.5 mm. Field shaping rings made from copper strips are wrapped around the acrylic vessel. The cathode, the shaping rings and the grid define a homogeneous drift field inside of the acrylic vessel.

At 3-bar pressure the TPC was operated with a drift field of 206 V cm^{-1} and a total drift time of 74.8 μs, which gives a drift velocity of 2.14 cm. μs^{-1}.

The drift volume of the TPC acts as a target for the neutrinos and as detector for the recoiling electrons at the same time. When a neutrino interacts with an electron from the gas,

the electron starts to move and produces a track (due to its ionization of the gas along its trajectory). The secondary ionization electrons from the track drift to the anode where they are collected by the anode wires and multiplied. The integrated anode signal corresponds to the total deposited energy. The *x* - *y* plane provides a spatial information on the tracks in the x and y directions by measuring the induced charge. The third projection z is obtained from the time evolution of the signal.

The signals from the x and y strips and the anode are amplified with preamplifiers. They are sampled at 80 ns sampling time with 8 bit FADCs with a logarithmic response.

The CF4 gas was constantly purified with a commercial high temperature getter made by SAES followed by a cold trap. This allows good charge collection and minimizes the background originating from the radon chain.

Due to the tracking capabilities of the TPC we could easily identify single electrons originating from inside of the fiducial volume. This allows us to reject the background, such as β and α activities from the side walls, Compton electrons, e^{+}–e^{-} pairs inside of the volume and cosmic muons.

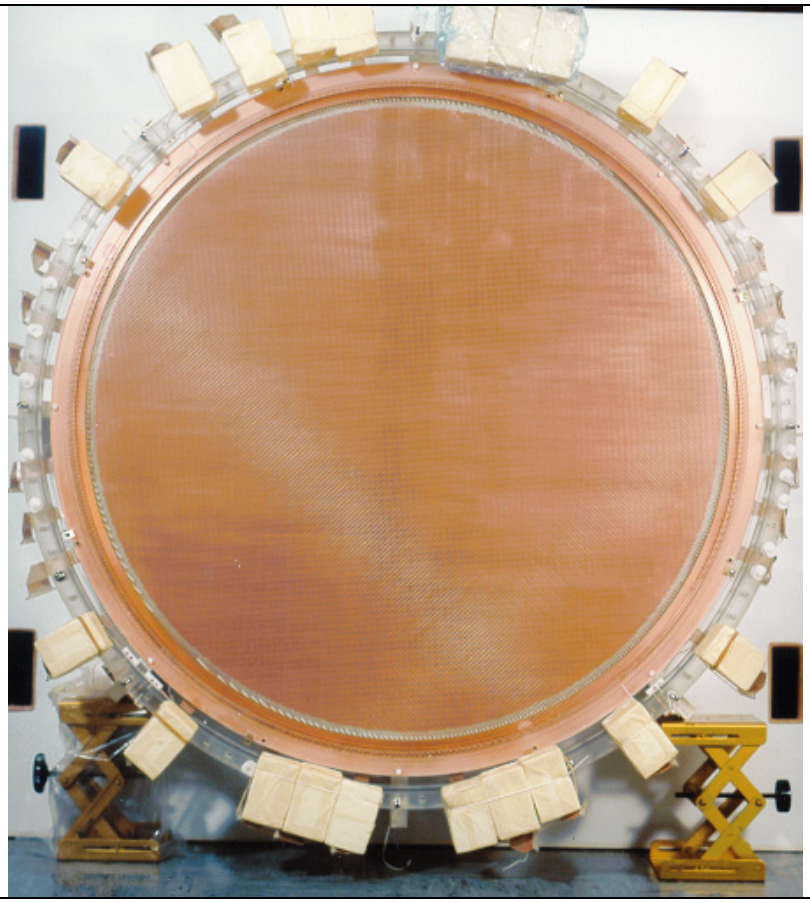

Fig.7 .x-y plane is shown.

I.3.2 Anti Compton detector

The second part of the detector is an Anti Compton detector which surrounds the TPC and consists of 10 m^3 of mineral oil based liquid scintillator (NE235, provided by Nuclear Enterprise, Scotland) with an attenuation length of 8 m at 430 nm.

The scintillator is contained in a steel vessel (380 cm length and 200 diameter) and is viewed by 48 photomultipliers (PM's) (20 cm diameter, EMI 9351), 24 each on the cathode and anode sides. The picture of the steel vessel is shown in Fig.8.

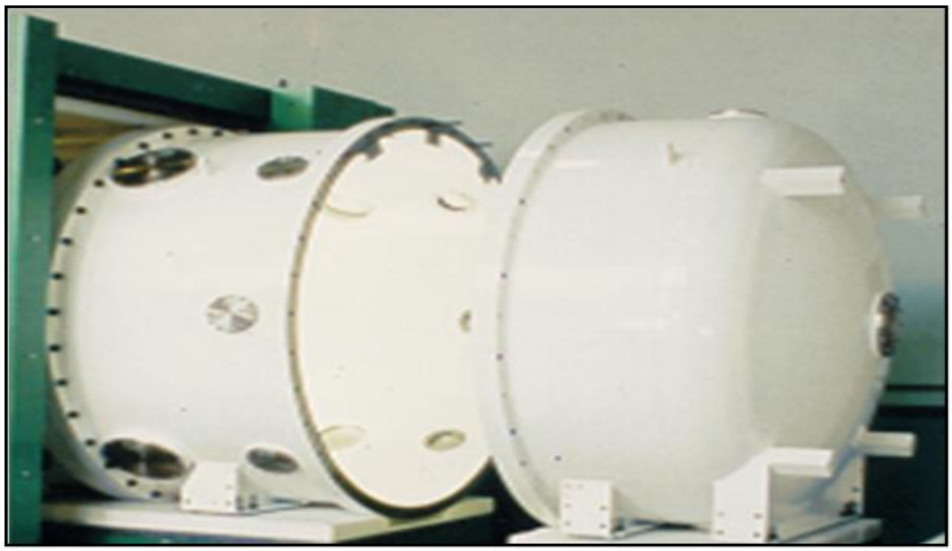

Fig.8. Steel vessel of the anti-Compton is shown

The photomultipliers are sampled with the same FADCs as the TPC x-y strips and the anode.

The anti-Compton detector serves to identify and reject Compton electrons produced by γ-rays originating from inside and outside of the TPC with 99 % efficiencies [35]. At the same time it serves to veto the cosmic muons.

Since the TPC walls are made of transparent acrylic, the scintillator could see the primary light of heavily ionizing particles, such as alphas in the gas. However, the primary light of the minimum ionizing particles, such as electrons and muons could not be seen because of the acrylic wavelength cut below ~ 400 nm.

The scintillator could see, however, the light produced by the avalanche found close to the anode plane in the TPC. This provides additional information on the charge collected by the anode.

I.3.3. Passive shielding

The third part of the detector is the Passive Shielding.

The liquid scintillator and the steel vessel serve as low activity shielding. In addition, there are 8 cm of polyethylene to absorb neutrons entering from outside of the detector. The first and the last cm are loaded with boron. There is also 15 cm of Pb in the form of bricks to absorb external gammas.

CHAPTER II

Visual scanning procedure

II.1. DISP program

There are 6 main triggers which allow one to save the different events and copy them to the disk [36]:

the ‘’**low Anti-Compton**’’ trigger corresponds to an energy threshold of 100 keV and a multiplicity criteria seeking at least 5 phototubes hit

the ‘’**high Anti-Compton**’’ trigger corresponds to an energy threshold of 300 keV and a multiplicity criteria seeking at least 8 phototubes hit

the ‘’**muon’**’ trigger corresponds to an energy threshold of the PM’s (Photomultipliers) in the order of 22 MeV

the ‘’**TPC**’’ trigger corresponds to an energy threshold of 150 keV in the TPC

the ‘’**TPC veto muon**’’ select the events that are not muons by applying an anticoincidence of 200 μs between the signal **‘’TPC’’** and the signal ‘’**muon**’’

the ‘’**neutrino**’’ trigger selects the electrons in the TPC which are not in coincidence with gamma in the scintillator. This trigger is a combination of the triggers ‘’**TPC veto muon’’** and ‘’**low Anti Compton**’’ having an anticoincidence of 80 μs. The energy threshold is 150 keV.

The images of the traces which particles have produced in the TPC can be ‘photographed’ with the help of signals on 256 *x* and 256 *y* strips as a function of time *z*.

The program which is used for the visual scanning of events is called DISP [37]. It displays, in fact, event by event offline.

By using the program DISP the operator firstly classifies an event as electron, muon, gamma (Compton electron), alpha etc. The tracks of the events differ from one another in shape (resulting in the different multiple scattering) and colour (corresponding to the deposited energy) in the TPC. The capacity of the MUNU detector to reveal a clear signature

of different events gives one the possibility to select easily the neutrino candidate and reject the background.

II.1.1 Selection of the events

There are 15 possibilities for classification of the events with the program DISP.

Here it will be explained what kind of signature have the main classes of events in the TPC and how they differ visually from one to another.

II.1.1.1. class ‘‘muon’’

The muons deposit energy of the order of 22 MeV in the Anti Compton detector. A cosmic muon produces a large prompt signal on the anode and in the photomultipliers (PM’s) at the beginning (Fig.9). The form of the track of a cosmic muon in the TPC is a straight line as it shown in Fig.9.

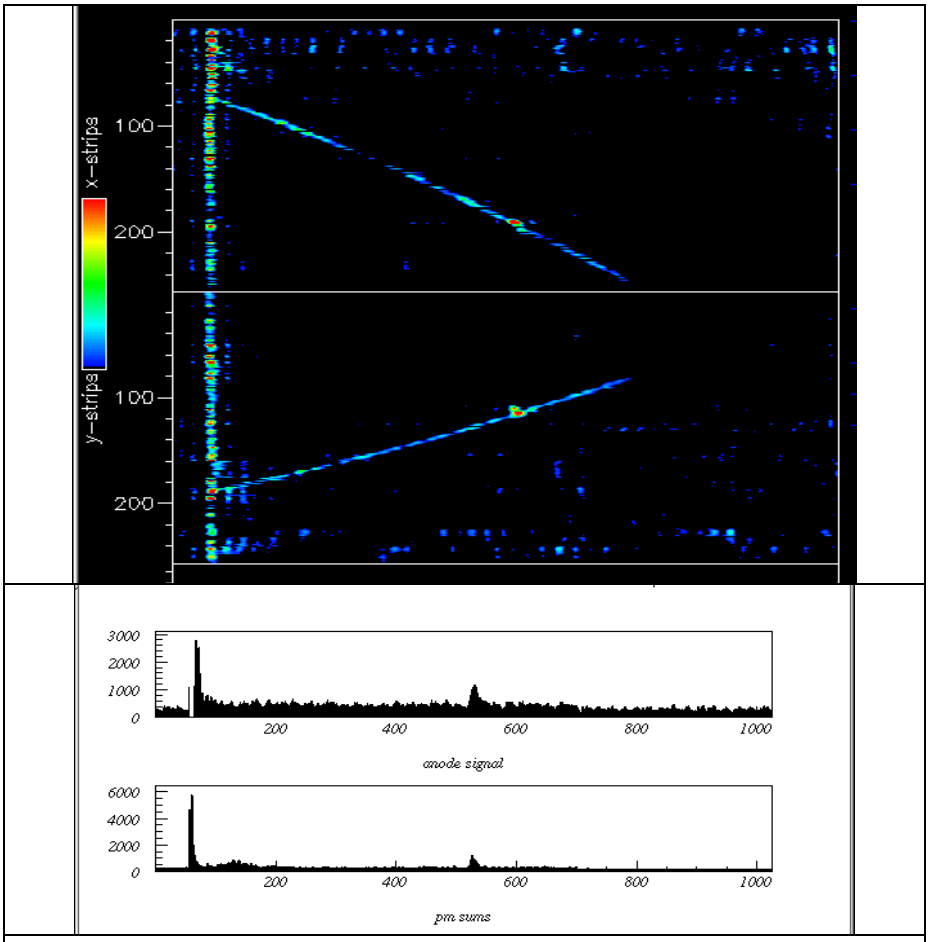

Fig.9. A cosmic muon. The xz, yz projections (Cf. II.1.2), signals produced by muon on the anode and on the PM’s (bottom figure) are shown on top, middle and bottom of the figure, respectively..

II.1.1.2. class ‘‘gamma’’

A Compton electron is distinguished from a normal electron by the deposited energy in the Anti Compton detector. The light signal of the scattered γ is measured by PM’s (Photomultipliers), before the signal produced by the avalanche light with a time delay proportional to the distance to the anode.

In Fig.10 is shown a Compton electron, together with the signals, produced in PM’s and on the anode.

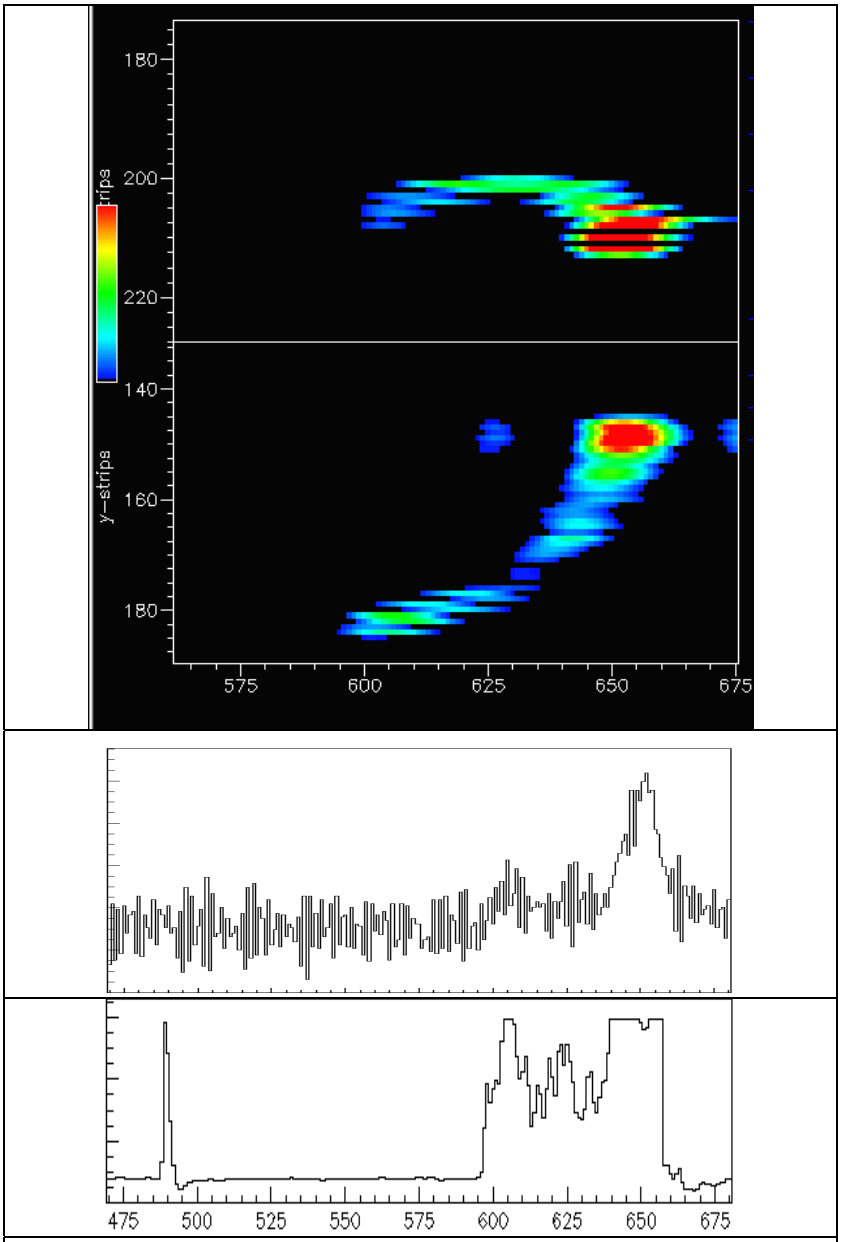

Fig.10. A Compton electron, with anode signal and PM’s sum, is shown on top, middle and bottom of the figure, respectively. In the PM’s the signal of the scattered γ (z =4 80, 1 *zbin* = 0.16 cm) is registered before the start of the signal produced by the electron on the anode (z = 600) with a time delay of z=120.

II.1.1.3. class ‘‘alpha’’

If the event is an alpha particle, then it deposits all of its energy at one point. In Fig 11 is shown an alpha particle in the TPC.

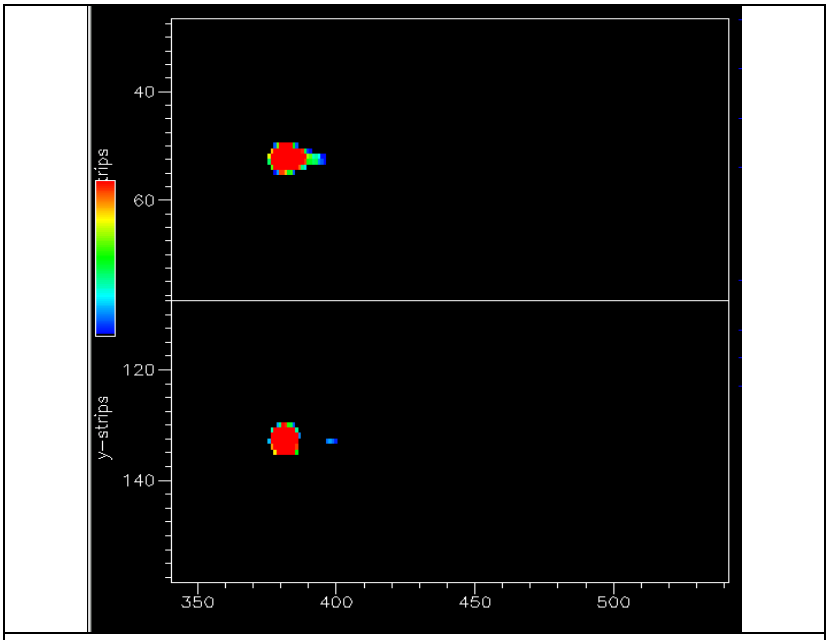

Fig.11. An alpha particle. The *xz* and *yz* projection on top, and bottom of the figure, respectively.

II.1.1.4. class ‘‘e^+e^-’’

There is also e^+e^- pairs in the TPC .The example in Fig.12 shows clearly 2 tracks.

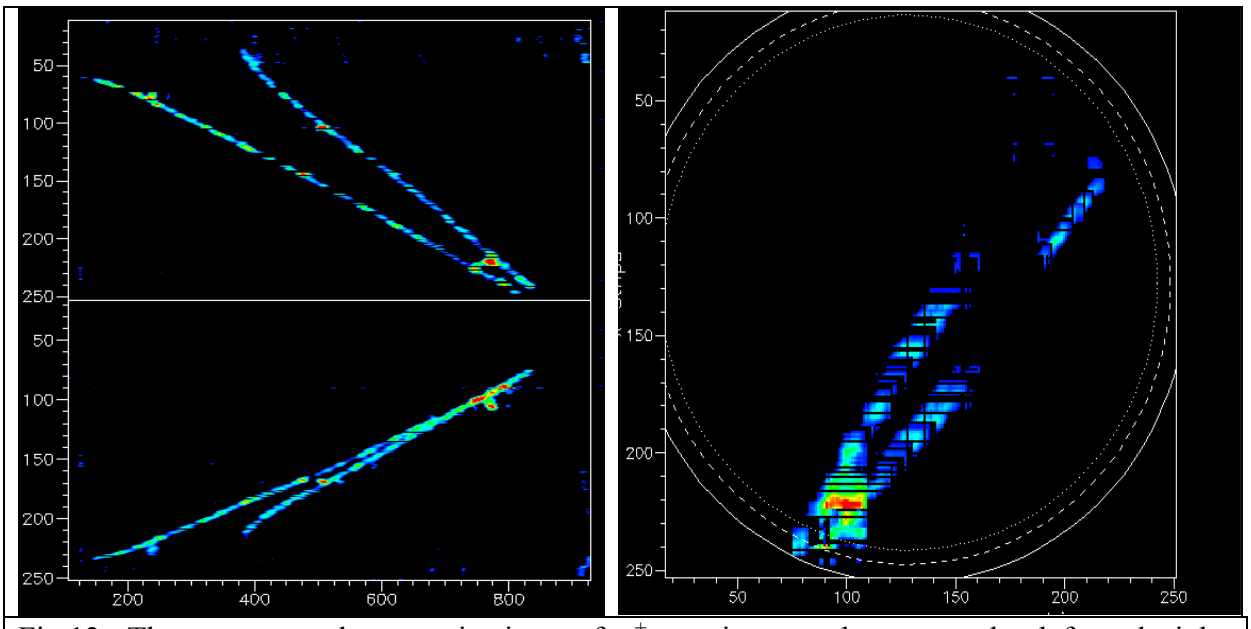

Fig.12. The xz, yz and xy projections of e^+e^- pairs are shown on the left and right, respectively.

Rare events

TPC could also ‘photograph’ some rare events, for example protons, as it is shown in fig.13.

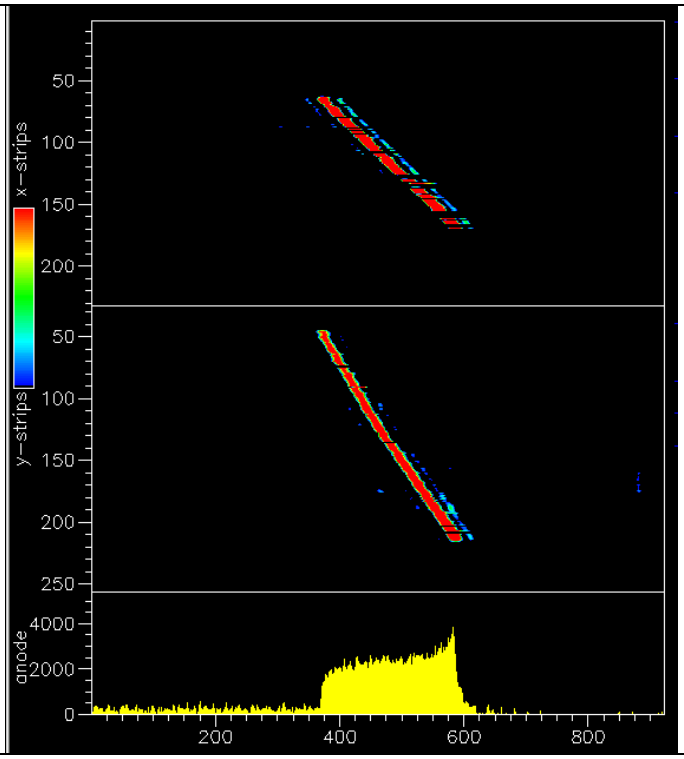

Fig.13. A proton: xz, yz projections and anode signal are shown on top, middle and bottom of the figure, respectively.

If the event is an electron it is classified according to its position in the detector volume: inside of the detector (R ≤42 cm) or outside the detector (R>42 cm).

II.1.1.5. class ‘‘electron out’’

An electron is classified in this class, if it is outside of the fiducial volume (R>42 cm).

If the electron is inside of the detector volume (R<42 cm) it could be classified as:

II.1.1.6. class ‘‘other 1’’

An electron, which has both no start and no end clearly identified, is classified in this class. The picture of such an electron is shown in Fig.14.

II.1.1.7. class ‘‘other 2’’

An electron, which has two ends (blobs), is classified in this class and the picture of such an electron is shown in Fig.15.

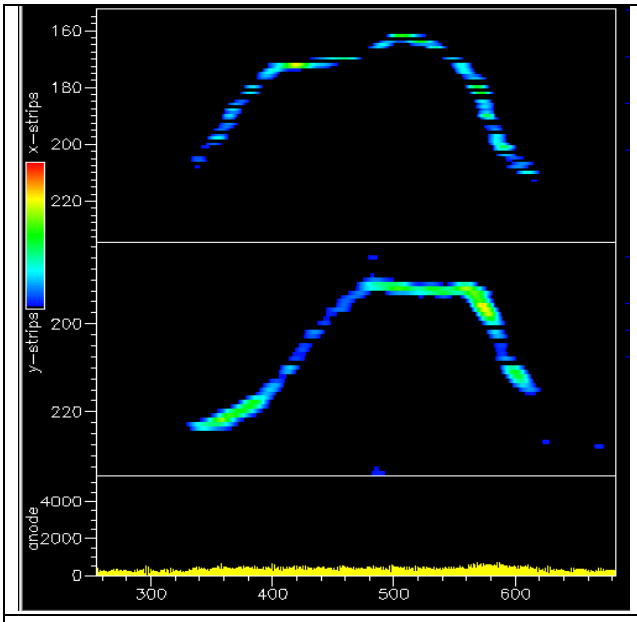

Fig.14. Electron with no start and no end (other 1) is shown

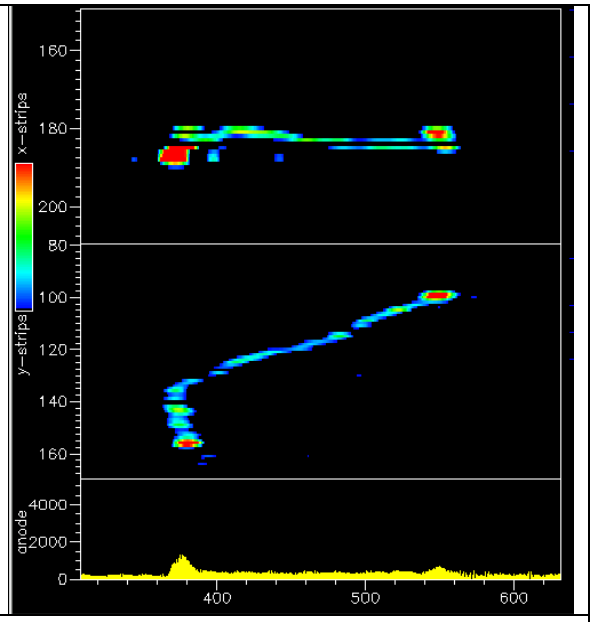

Fig.15.Electron with two blobs (other 2) is shown

II.1.1.8. class ‘‘electron in’’

An electron is classified as ‘electron in’ if:

- **it has no energy deposition in the Anti Compton detector**
- **it is inside of the fiducial volume (R< 42 cm)**
- **it has clearly distinguishable start and end (blob).**

The end of the track is identified from the increased energy deposition, which resulted from the higher stopping power.

There is a colour code in which the energy is translated to the colour. The red colour corresponds to the highest energy, while the blue colour corresponds to the smallest energy in the DISP (see the small window in the left side of the fig.16).

When an event is classified as ‘electron in’ the operator determines visually the tangent at the start of the electron track. From this the angles θ_{rea} (the angle between the electron direction and the reactor core-detector axis) and θ_{det} (the angle between the electron direction and the TPC axis) are determined.

One fully contained single electron and the tangent of the first cm of the track in *xz, yz,* and *xy* projections of the track are presented in Fig.16.

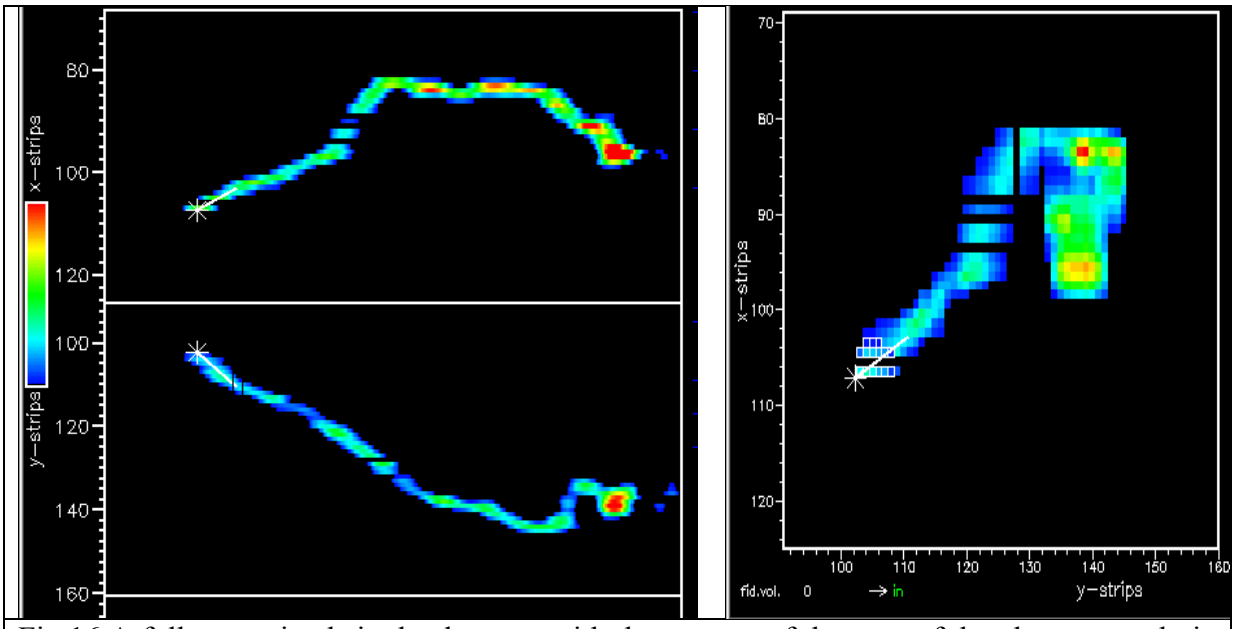

Fig.16.A fully contained single electron, with the tangent of the start of the electron track, in *xz* (top left), *yz* (bottom left) and *xy* (right) projections.

II.1.2 Determination of the angles with the program DISP

We will use the drawing of an electron track together with the tangent of the start of this track in the *XZ* and *YZ* projections (Fig.17) in order to explain the determination of the angles θ_{det}, φ_{det} and θ_{rea}. *X* axis coincides with *x* strips and *Y* axis coincides with *y* strips on the *xy* plane. *Z* axis is determined by the drift time and it is not a real axis in the space.

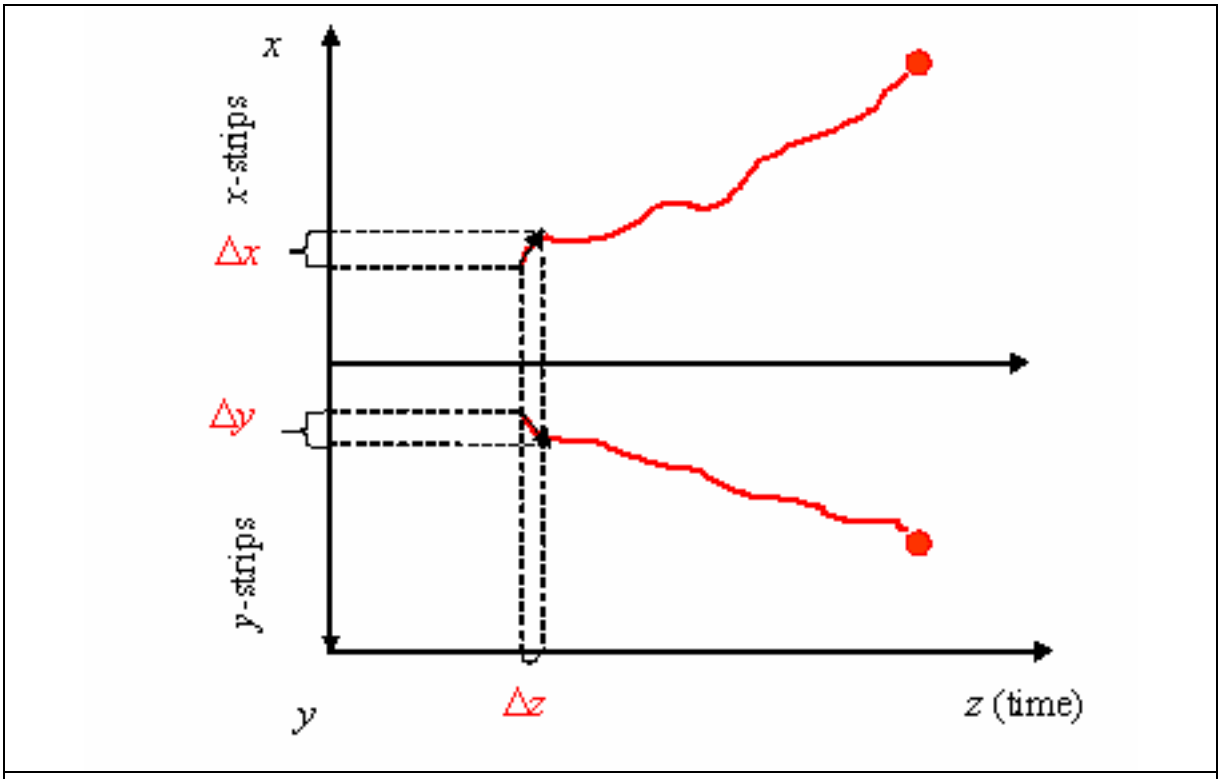

Fig.17. *Δx, Δy and Δz* projections of the tangent of the first cm of the track of one single contained electron

a) θ_{det} angle

θ_{det} is the angle between $\vec{L}$ (the electron direction) and *z* axis of the detector (see fig.17).

One obtains θ_{det} angle by using the *Δx, Δy* and Δ*z* projections, the coordinate system of the detector and the notations in Fig.18.

$$\cos\theta_{\det} = \frac{L_Z}{\left|\vec{L}\right|}, \qquad (5)$$

$\vec{L}_X$, $\vec{L}_Y$ and $\vec{L}_Z$ are the projections of vector $\vec{L}$ on x, y, and z respectively.

Where $L_X = \Delta x \qquad L_Y = \Delta y \qquad L_Z = \Delta z$

$$\left|\vec{L}\right| = \sqrt{(\Delta x)^2 + (\Delta y)^2 + (\Delta z)^2}$$

$$\theta_{\det} = \arccos \frac{\Delta z}{\sqrt{(\Delta x)^2 + (\Delta y)^2 + (\Delta z)^2}} \qquad (6)$$

b) $\varphi_{\det}$ angle

φ_{det} is the angle between $\vec{L}_{xy}$ and $\vec{L}_x$, where $\vec{L}_{xy}$ is the projection of the vector $\vec{L}$ (electron direction) on xy plane and $\vec{L}_x$ is the projection of the vector $\vec{L}$ on x axis, respectively.

Similarly to the θ_{det} one can obtain φ_{det} by using the Δx, Δy and Δz projections, coordinate system of the detector and notations in Fig.18.

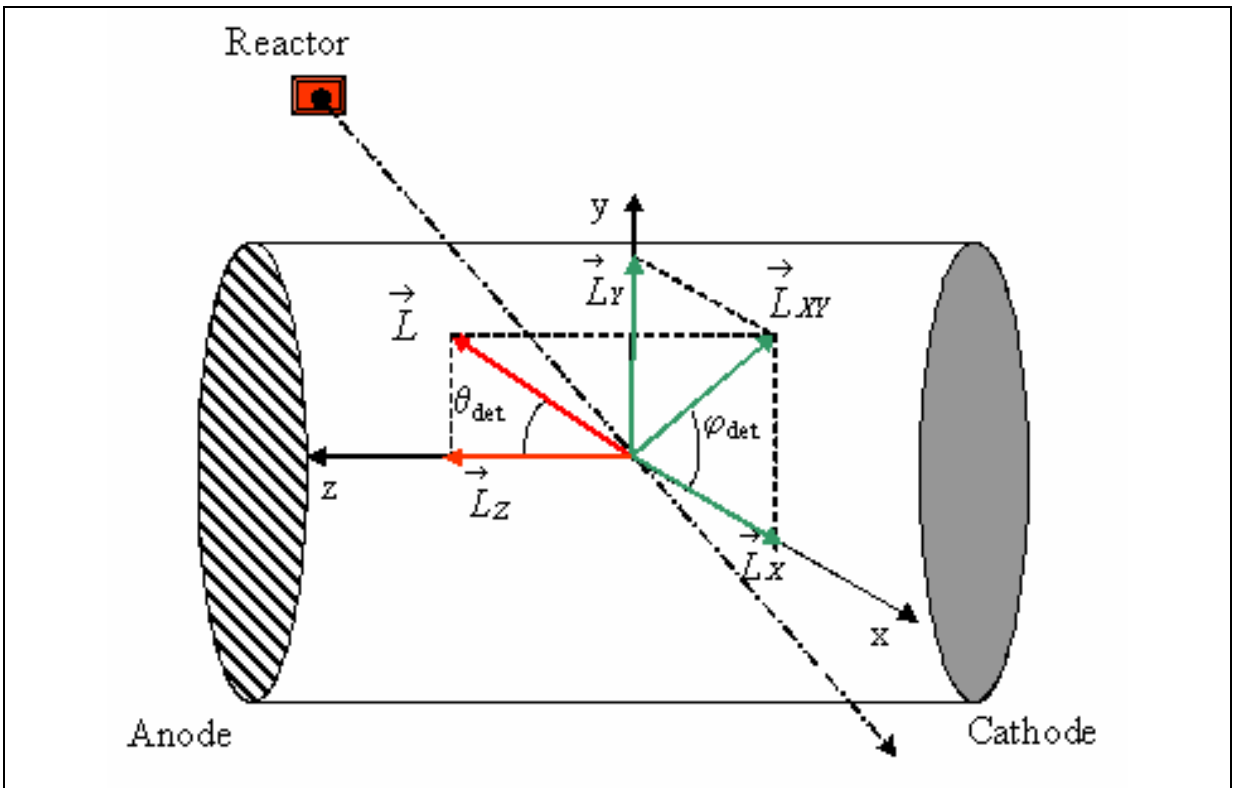

Fig.18. The detector coordinate system.

$$\cos\varphi_{\det} = \frac{L_X}{\left|\vec{L}_{XY}\right|}, \tag{7}$$

As far as $L_X = \Delta x$ and $\left|\vec{L}_{XY}\right| = \sqrt{(\Delta x)^2 + (\Delta y)^2}$

Equation (7) can be written as

$$\varphi_{\det} = \arccos\frac{\Delta x}{\sqrt{(\Delta x)^2 + (\Delta y)^2}} \tag{8}$$

c) θ_{rea} angle

θ_{rea} is the angle between vector $\vec{L}$ (the electron direction) and the reactor direction *r*.

Now we use the same coordinate system of the detector as we did earlier, but with one important difference: the reactor direction, which is used as a reference in Fig.19. The reactor direction lays in *xy* plane and makes the following angles with the detector: θ_{drea} = 90° and φ_{drea} = -46.5°. By using the notations in Fig.19 one obtains the θ_{rea} angle.

$$\cos\theta_{rea} = \frac{\left|\vec{R}\right|}{\left|\vec{L}\right|} \tag{9}$$

Vector $\vec{R}$ is the projection of the vector $\vec{L}$ on reactor direction.

$$R_Y = \cos\varphi_{drea} R \tag{10}$$

$$-R_X = \sin\varphi_{drea} R \tag{11}$$

We multiply Eq. (10) by $cos\varphi_{drea}$ and Eq. (11) by $sin\varphi_{drea}$, and add them. The result is given in the equation (12).

$$R_Y \cos\varphi_{drea} - R_X \sin\varphi_{drea} = (\cos^2\varphi_{drea} + \sin^2\varphi_{drea})R \tag{12}$$

In Eq. (12) $\cos^2\varphi_{drea}+\sin^2\varphi_{drea}=1$.

R_X and R_Y are the projections of the vector $\vec{R}$ on *x* and on *y*, respectively

$$R_X = \Delta x \qquad R_Y = \Delta y$$

Finally we obtained for R

$$\Delta y \cos\varphi_{drea} - \Delta x \sin\varphi_{drea} = R \tag{13}$$

For the θ_{rea} angle the final result is

$$\theta_{rea} = \arccos \frac{\Delta y \cos\varphi_{drea} - \Delta x \sin\varphi_{drea}}{\sqrt{(\Delta x)^2 + (\Delta y)^2 + (\Delta z)^2}} \tag{14}$$

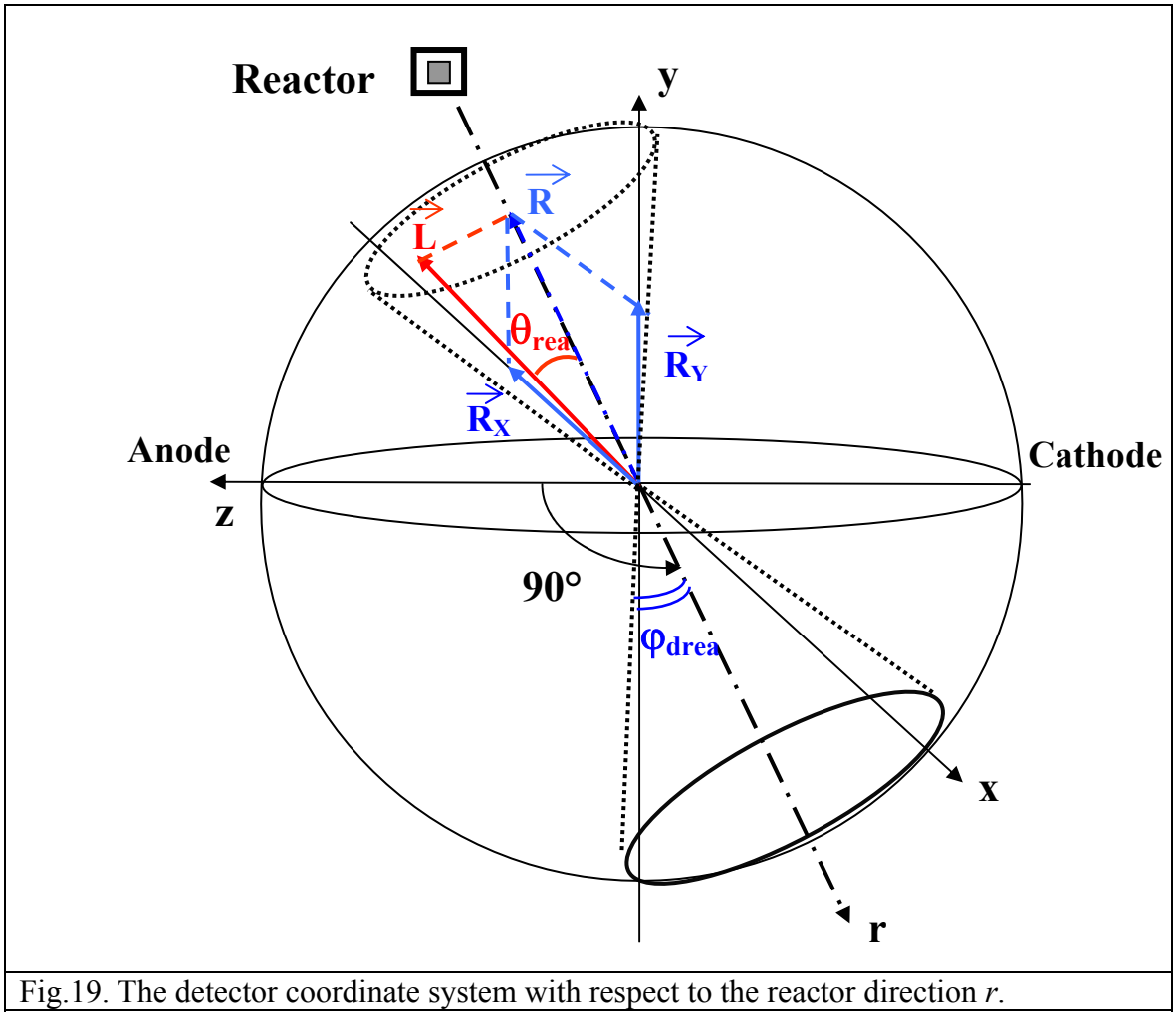

Fig.19. The detector coordinate system with respect to the reactor direction *r*.

II.2. Determination of the initial neutrino energy from Kinematics

The determination of the initial neutrino energy (E_ν) from the Kinematics of the electron antineutrino – electron elastic scattering is used to select the neutrino candidates and reject the background.

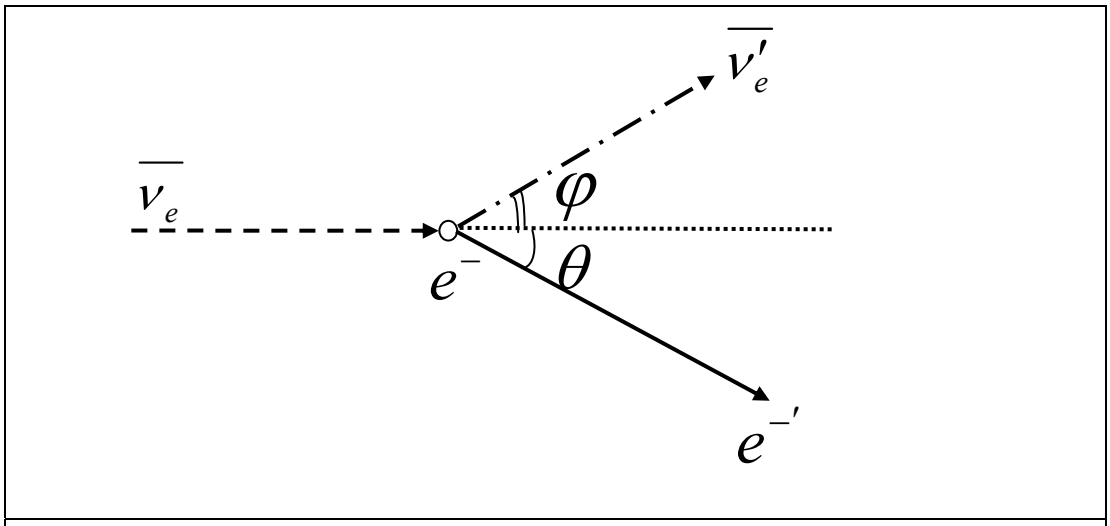

Fig.20. Scheme of electron antineutrino - electron interaction.

To determine initial neutrino energy we use four-vector notations Eq. (15) for electron antineutrino ($\overline{\nu}_e$) – electron (e^-) elastic scattering, the scheme of which is presented in Fig.20.

$$\frac{E^2}{c^2} - p^2 = m^2c^2 \tag{15}$$

In the initial state, the target particle (electron) is at rest and the neutrino is moving in the laboratory frame. One could write for the initial energy of the electron E_e

$$E_e = m_e c^2 \qquad (\vec{p}_e = 0) \tag{16}$$

In the final state the energy of the electron is expressed by(17).

$$\frac{E'^2_e}{c^2} - p'^2_e = m_e^2 c^2 \qquad (\vec{p}_e{}' \neq 0) \tag{17}$$

For the energy of the neutrino in the initial E_ν and in the final state E'_ν one could write the expressions (18) and (19), respectively.

$$\frac{E_\nu^2}{c^2} - p_\nu^2 = 0 \qquad (18)$$

(m_ν=0)

$$\frac{E_\nu'^2}{c^2} - p_\nu'^2 = 0 \qquad (19)$$

From the Kinematics of the elastic scattering of the electron antineutrino and electron, one could deduce the expressions Eq. (20) and (21) from the conservation laws of energy and momentum, respectively.

$$E_\nu + E_e = E'_\nu + E'_e \qquad (20)$$

$$\vec{p}_\nu = \vec{p'}_\nu + \vec{p'_e} \qquad (21)$$

Where E_ν and E'_ν are the neutrino energies before and after scattering, E_e and E'_e are the electron energies before and after scattering, p_ν and p'_ν are the momentum of the neutrino before and after scattering, p_e and p'_e are the momentum of the electron before and after scattering respectively.

We express E'_ν from (20)

$$E_\nu - E'_\nu + E_e = E'_\nu \qquad (22)$$

and $\vec{p'_\nu}$ from (21)

$$\vec{p}_\nu - \vec{p'_e} = \vec{p'}_\nu \qquad (23)$$

We square (22) and multiply the product by $1/c^2$, after that we subtract from this product the squared product of equation (23). As a result, we obtain with $E_e = m_e c^2$

$$\frac{(E_\nu - E'_e + m_e c^2)^2}{c^2} - (\vec{p}_\nu - \vec{p'_e})^2 = \frac{E_\nu'^2}{c^2} - \vec{p'}_\nu^{\,2} \qquad (24)$$

The right side, which is equal to $m_\nu^2 c^2$ and it vanishes ($m_\nu = 0$). Consequently, one may write (24) as

$$\frac{(E_\nu - E'_e + m_e c^2)^2}{c^2} = (\vec{p}_\nu - \vec{p}'_e)^2 \tag{25}$$

with

$$(\vec{p}_\nu - \vec{p}'_e)^2 = p_\nu p'_e \cos\theta \tag{26}$$

$$\theta = \angle(\vec{p}_\nu, \vec{p}_e)$$

From (17), (18), (25) and (26), the neutrino energy E_ν can be easily derived. One gets

$$E_\nu = \frac{m_e c^2 (E'_e - m_e c^2)}{-(E'_e - m_e c^2) + \cos\theta \sqrt{E'^2_e - m_e^2 c^4}} \tag{27}$$

To simplify the reading, the above formula is usually expressed as

$$E_\nu = \frac{m_e c^2}{\cos\theta \sqrt{\frac{E'_e + m_e c^2}{E'_e - m_e c^2}} - 1} \tag{28}$$

It is important to mention here that we cannot measure the energy of the electron E'_e in the detector, but its kinetic energy T_e ($T_e = E'_e - m_e c^2$). With the help of Eq. (28), the final expression for the neutrino energy can be stated as:

$$E_\nu = \frac{m_e c^2}{\cos\theta \sqrt{\frac{T_e + 2m_e c^2}{T_e}} - 1} \tag{29}$$

Where m_e is the mass of the electron and θ is the angle between the electron and the initial neutrino direction. But since we cannot measure the angle θ we will assume that this angle is the same as the θ_{rea} angle (the angle between the electron direction and reactor direction) (14), which we measure with the MUNU detector.

II.2.1. Forward and Backward kinematical cones

The forward and backward kinematical cones are defined with the help of the neutrino initial energy E_ν (29) and the scattering angle between the electron and the reactor direction θ_{rea} (14).

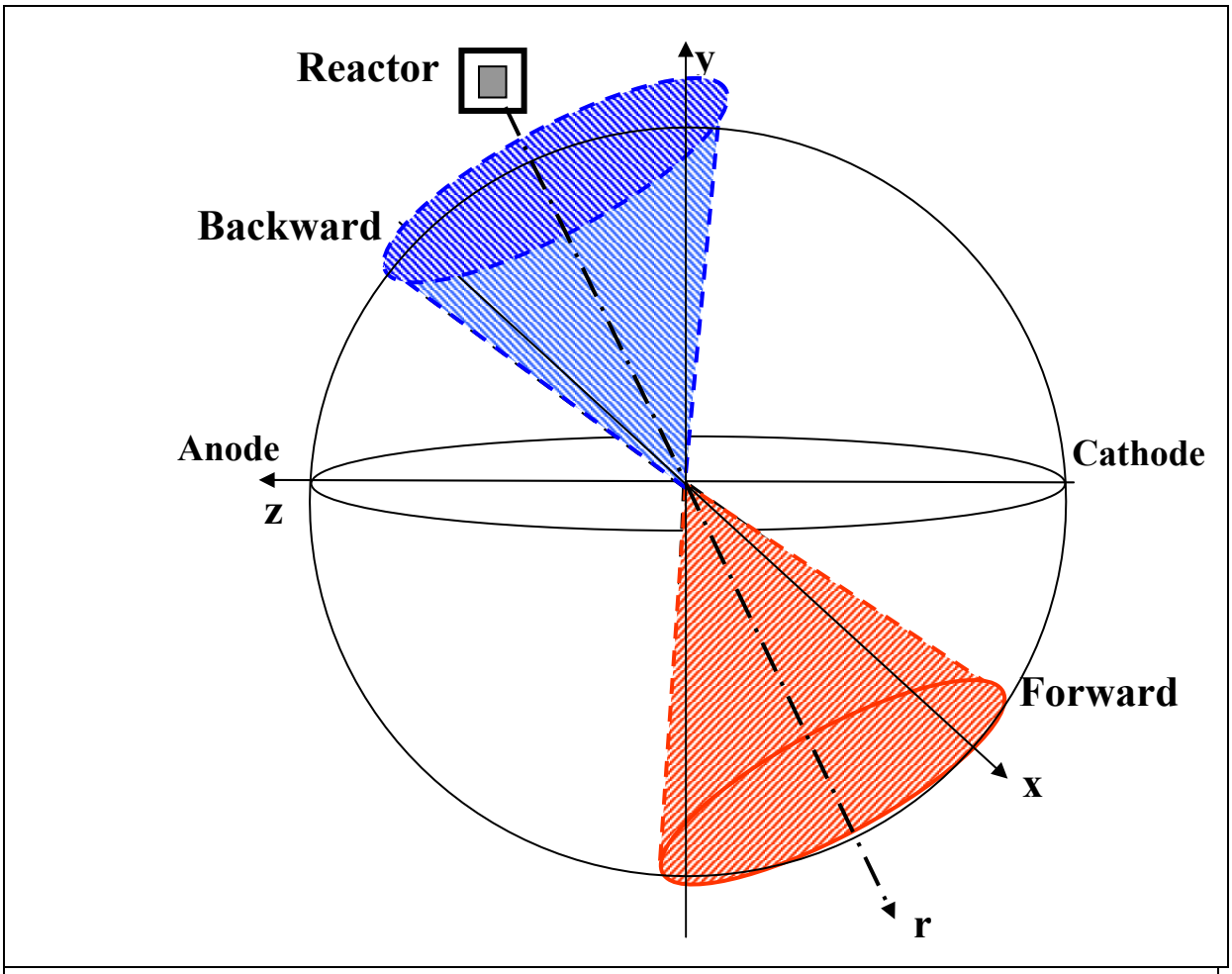

Fig.21. The forward and backward kinematical cones in the detector system.

The neutrino energy E_ν is positive, hence the maximal scattering angle is:

$$\theta_{reac\max} = a\cos\sqrt{\frac{T_e}{T_e + 2m_e c^2}} \qquad (30)$$

The **forward cone** is defined in the interval: $0 < \theta_{reac} < \theta_{reacmax}$ while the **backward cone** is defined in the interval: $\pi - \theta_{reacmax} < \theta_{reac} < \pi$.

The **forward electrons** which are inside of the forward kinematical cone, presented in fig.21 at the figure bottom, are the ones that have positive neutrino energy $E_\nu > 0$ and positive $\cos(\theta_{rea}) > 0$. In the forward cone there are signal plus background events.

The **backward electrons**, which are inside of the backward kinematical cone, presented in fig.21 at the figure top are the ones that have positive neutrino energy $E_\nu > 0$ and negative $\cos(\pi - \theta_{rea}) < 0$. In the backward cone there are only background events.

CHAPTER III

3 bar data analysis

III.1. Visual scan of MC events

The data samples are produced with the help of a Monte Carlo program (GEANT 3 code, [36, 38]). The electrons are scanned in the same way as the real data. The acceptances are derived by comparison of the simulated values with the ones obtained with the DISP program (Cf.II.1).

An example of a 1 MeV Monte Carlo electron of 3 bar pressure is presented in fig.22. The electronic noise is simulated and included in the simulation as well.

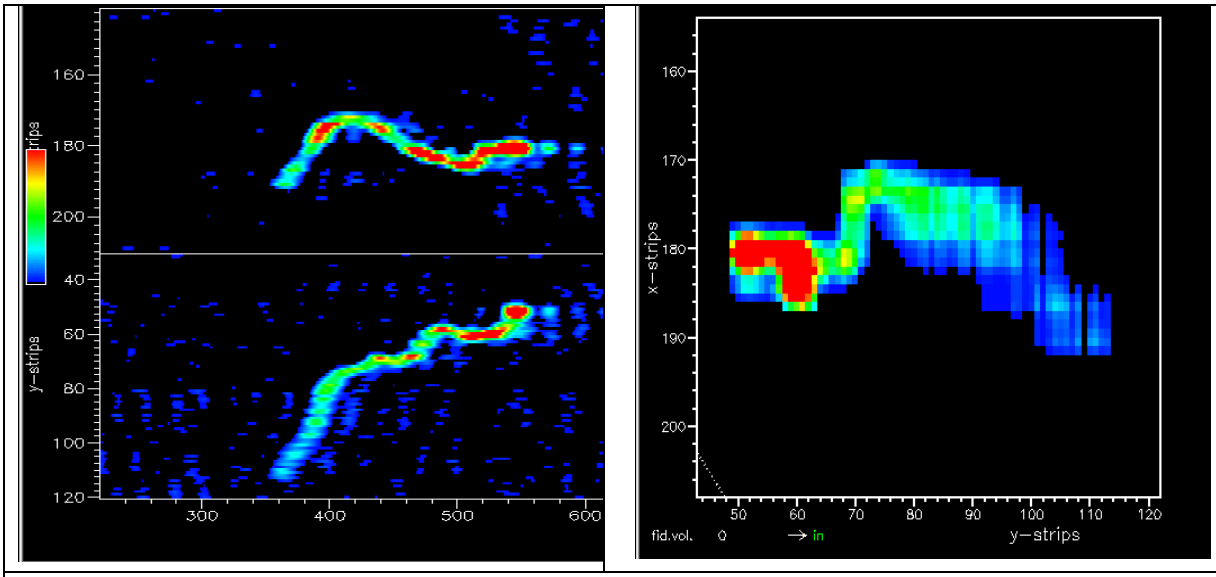

Fig.22. A 1 MeV Monte Carlo electron at 3-bar pressure: *xz* (top left), *yz* (bottom left) and *xy* (right) projections.

III.1.1. Angular resolutions of θ_{det}, θ_{rea} and φ_{det} angles

Electrons, with both the **reactor core direction** and energies between **700 keV and 2200 keV,** are simulated inside the TPC (Time Projection Chamber).

The simulated electrons are scanned with the program DISP. The angular resolutions of θ_{det}, θ_{rea} and φ_{det} angles (Cf.II.1.2) are estimated from the scanning.

The error on an arbitrary angle α could be defined as:

$$\Delta(\alpha) = \alpha_{MC} - \alpha_{DISP} \tag{31}$$

In (31) α_{MC} is the simulated value of the angle, while α_{DISP} is the value of the reconstructed angle obtained by the visual scan with DISP.

The errors on the angle α ($\Delta\alpha$) have a Gaussian distribution. The angular resolution $\sigma(\alpha)$ is the sigma of this Gaussian.

The error distributions on the angles θ_{det} ($\Delta\theta_{det}$), θ_{rea} ($\Delta\theta_{rea}$) and φ_{det} ($\Delta\varphi_{det}$) are shown in Fig.23, fig.24 and fig.25 respectively.

The angular resolutions of the angles are 10.6° (θ_{det}), 9.9° (θ_{rea}) and 13.2° (φ_{det}).

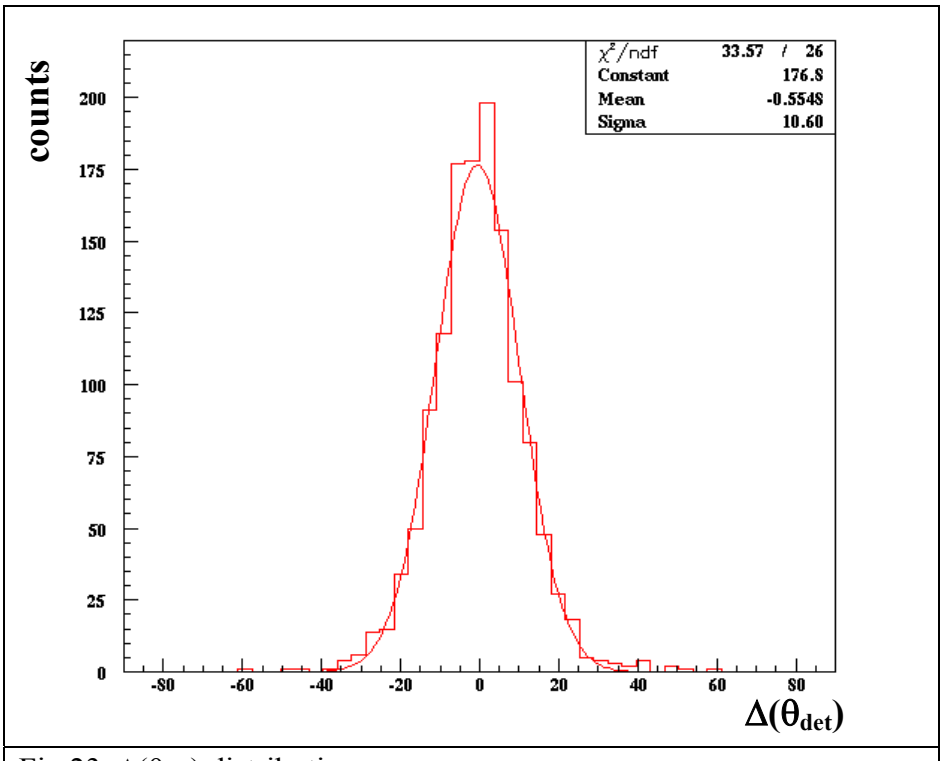

Fig.23. $\Delta(\theta_{det})$ distribution

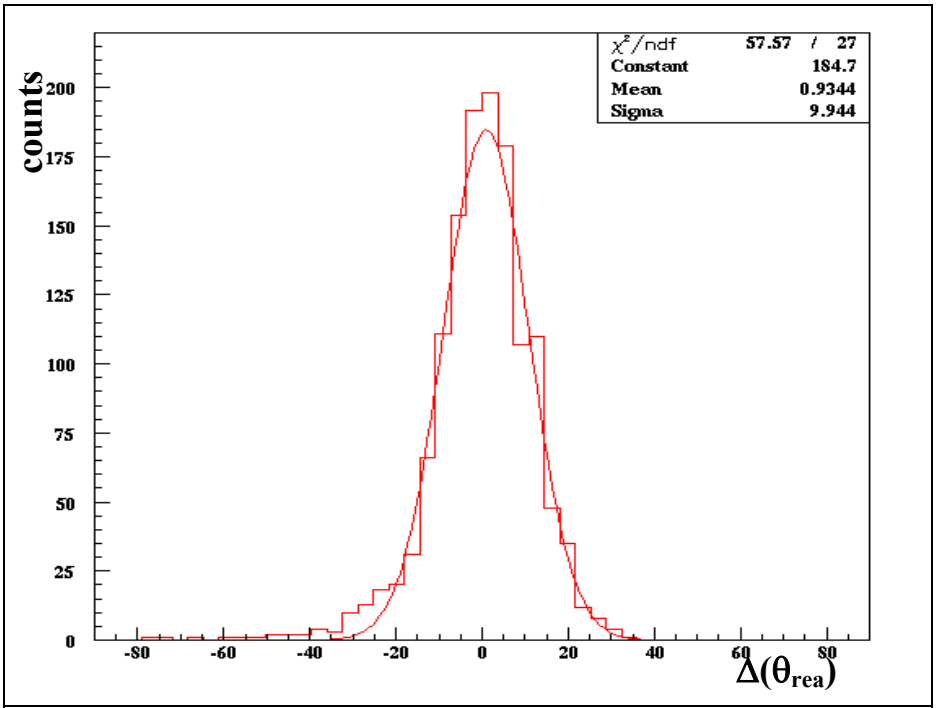

Fig.24. $\Delta(\theta_{rea})$ distribution.

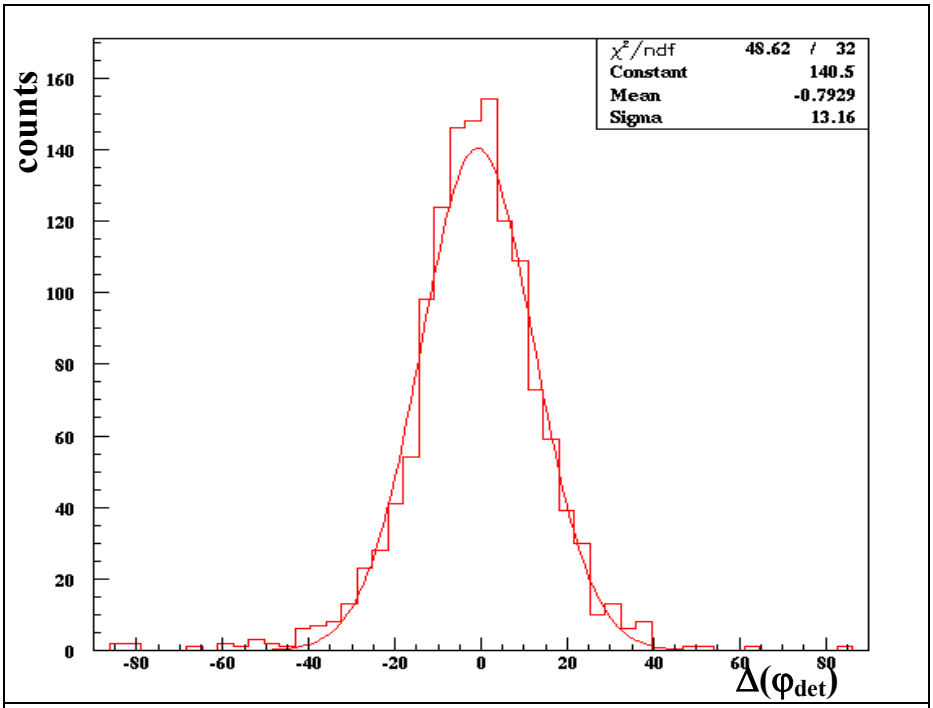

Fig.25. $\Delta(\varphi_{det})$ distribution.

III.1.1.1. Energy dependence of the angular resolutions

The angular resolutions of the angles depend on the energy.

For example the angular resolution of the angle θ_{det}, $\sigma(\theta_{det})$ at 700 keV is 13 %, at 900 keV is 11 %, at 1 MeV is 10.5 % and at 2 MeV is 7 % (Fig.26).

The angular resolution of θ_{rea}, $\sigma(\theta_{rea})$, at 700 keV is 12.5 %, at 900 keV is 11 %, at 1 MeV is 10 % and at 2 MeV is 7 % (Fig.27).

The angular resolution of φ_{det}, $\sigma(\varphi_{det})$ at 700 keV is 15 %, at 900 keV is 14 %, at 1 MeV is 13 % and at 2 MeV is 7 % (Fig.28).

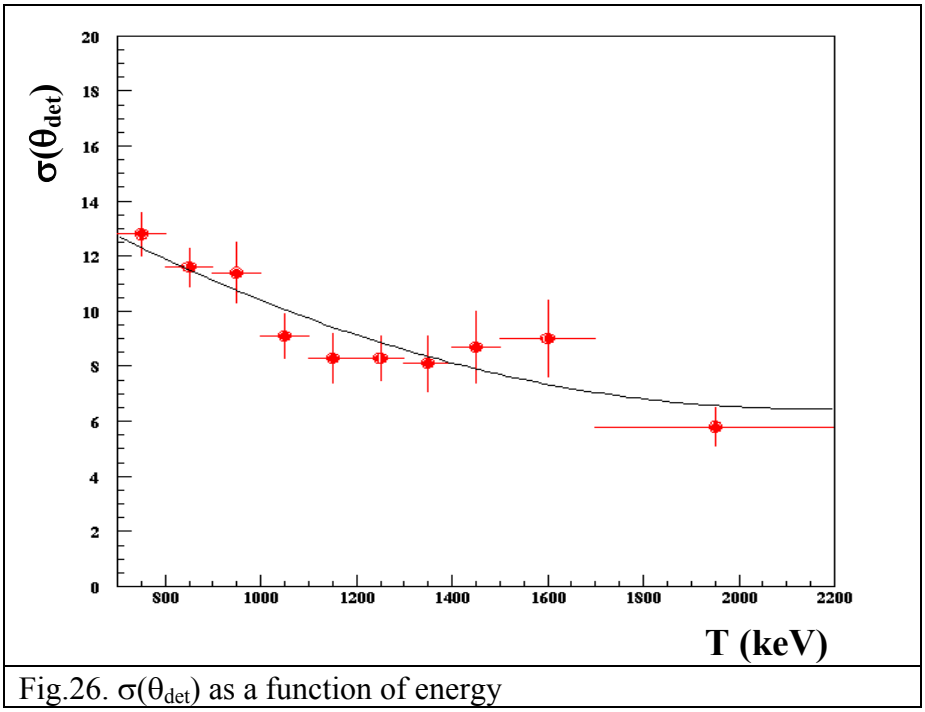

Fig.26. $\sigma(\theta_{det})$ as a function of energy

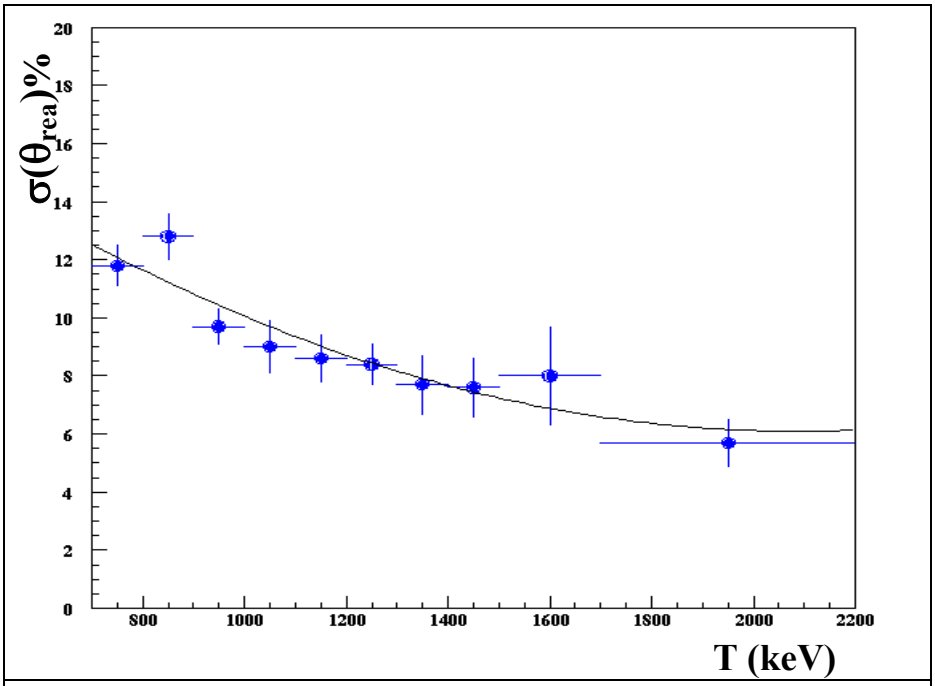

Fig.27. $\sigma(\theta_{rea})$ as a function of energy

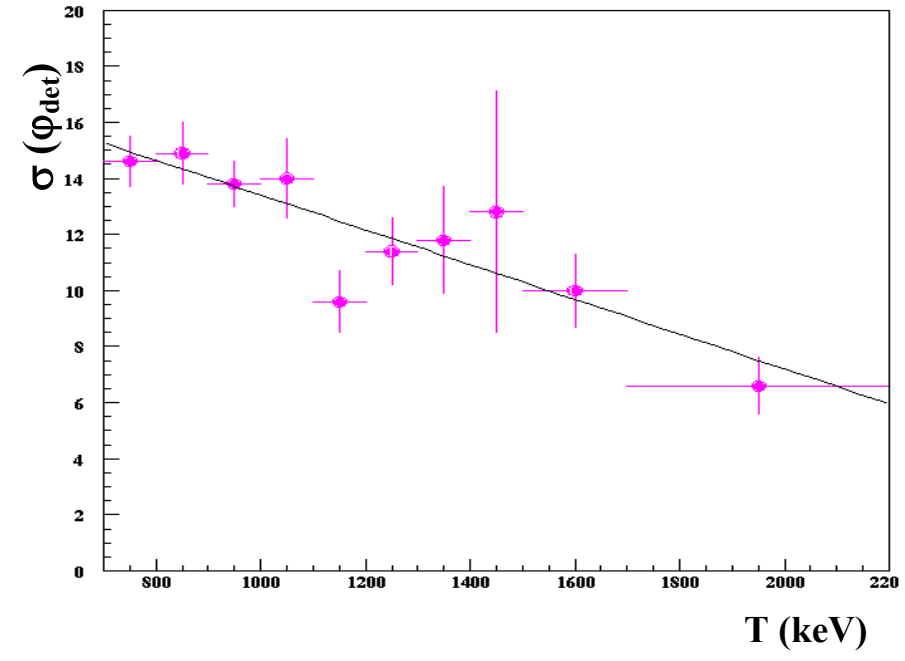

Fig.28. σ(φ_{det}) as a function of energy

III.1.2. Influence of the geometry of the detector to the reconstruction of the angles θ_{det}, θ_{rea} and φ_{det}

Due to the geometry of the detector some tracks could not be reconstructed. This result that in some values of the angles θ_{det}, θ_{rea} and φ_{det} the number of the reconstructed events is smaller than for other values.

Let's take as an example a real event which is parallel to the *x* axis. *X* and *Y* strips are perpendicular; hence the projection of the vertex on the *y* axis is zero (point like). The real case, however differs from ''point like''. The multiple scattering of such an event results in a projection of the vertex on the y axis far from the ''point like'' (the zone where the vertex is projected is marked with red line in fig.29).

The reconstruction of the vertex of such an event is difficult, because the start of the path on the *y* axis could not be localized clearly: it could start from the bottom, the top or somewhere from the middle of the region selected in red in fig.29. The different starting points of the vertex on the *y* axis will give different values for all angles.

Consequently, one could not define the start and the initial direction of such an electron; it is classified in the class ''other 1''.

The number of the events in class ''other 1''whose starts could not be defined clearly is 4 % of the total number of events resulting in an acceptance of 96 % of the visual scan. This acceptance could be called **Acceptance geometry.**

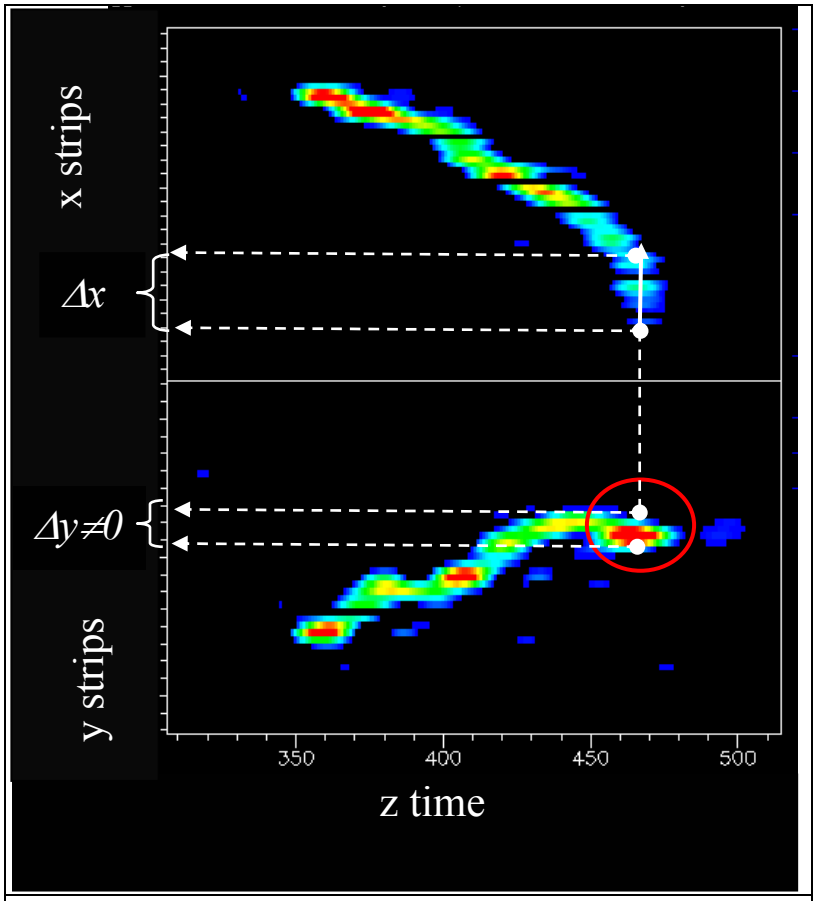

Fig.29. An electron, parallel to x axis.

To study the effect of the TPC geometry on the angles, we have simulated electrons **randomly** in the TPC (with energies between **700 keV and 2200 keV**) and scanned them visually**.**

III.1.2.1. Reconstruction of φ_{det} angle

From the distribution of the angle φ_{det} (Fig.30) one can see that in the intervals around: $\pm$ *90°* ($\pm$ *10°*), *0°* ($\pm$ *10°*) and *180°* ($\pm$ *10°*), the number of the reconstructed events is the smallest in comparison to the other regions.

In order to explain this discrepancy we recall here the formula for the φ_{det} angle (8)

$$\varphi_{\text{det}} = \arccos \frac{\Delta x}{\sqrt{(\Delta x)^2 + (\Delta y)^2}}$$

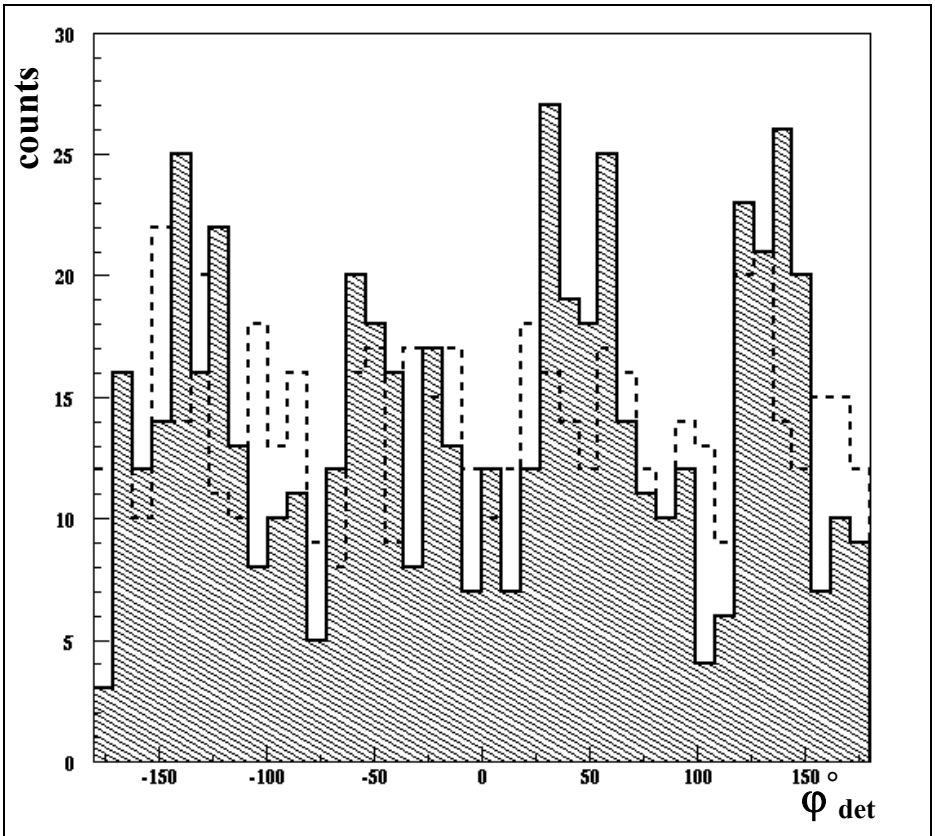

Fig.30. φ_{det} of simulated (dash line) and reconstructed (solid line) contained electrons

One gets $\varphi_{det} = 0°$ or $\varphi_{det} = 180$ for an event parallel to *x* axis (see Fig.29), because *x* and *y* axes are perpendicular to each other, the projection of this event on *y* axis is zero, i.e. $\Delta y = 0$.

Similarly one gets $\varphi_{det} = \pm 90°$ for an event, parallel to *y* axis, because the projection of this event on *x* axis is zero, i.e. $\Delta x = 0$

The lack of the reconstructed events at $\varphi_{det} = \pm 90°$, $\varphi_{det} = 0°$ and $\varphi_{det} = 180°$, in fact, results in an accumulation of events in the neighbour regions $\varphi_{det} = \pm 45°$ *and* $\varphi_{det} = \pm 135°$.

III.1.2.2. Reconstruction of θ_{det} angle

From the distribution of the angle θ_{det} (Fig.31) one can see that the number of the reconstructed events is the smallest in the region of 90° ± 10°.

In order to explain this we recall here the formula for θ_{det} angle (6)

$$\theta_{\det} = \arccos \frac{\Delta z}{\sqrt{(\Delta x)^2 + (\Delta y)^2 + (\Delta z)^2}}$$

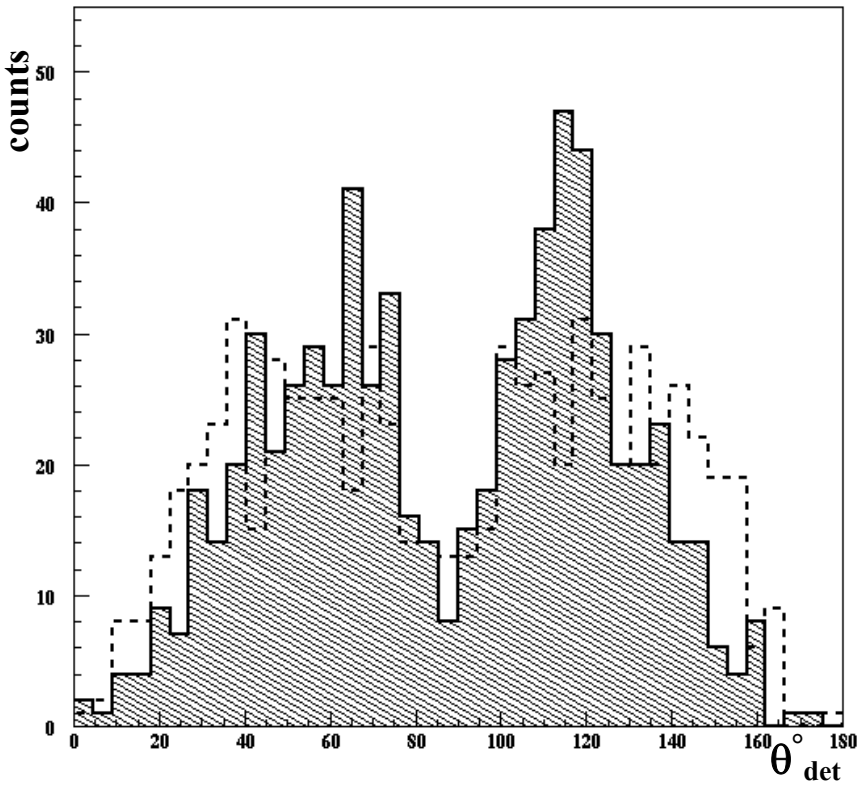

Fig.31. θ_{det} of simulated (dashed line) and reconstructed (solid line) contained electrons.

One gets $\theta_{det} = 90°$ for an event, perpendicular to the detector axis (*z)*, because the event projection on the *z* axis is zero, $\Delta z = 0$.

Let us look at the same example in fig.29, because the electron is perpendicular to *z* axis. For the reason mentioned before we could not determine the starting point of such an event on *y* axis precisely. Thus we classify it in class ‘‘other 1’’.

Therefore the number of reconstructed events, perpendicular to the detector axis *z* is smallest in the interval around $\theta_{det} = 90°$ (± 10°).

III.1.2.3. Reconstruction of θ_{rea} angle

From the distribution of θ_{rea} (Fig.32) one can see that the number of the reconstructed events is smaller in the regions of *+ 45° (± 10°)* and *+ 135° (± 10°).*

As a consequence we have the smaller number of the reconstructed events in the region *cos* (θ_{rea}) = *± 0.7 (± 0.1)* (see fig.33).

In order to explain the above results we recall here the formula for θ_{rea} angle (14)

$$\theta_{rea} = \arccos \frac{\Delta y \cos\varphi_{drea} - \Delta x \sin\varphi_{drea}}{\sqrt{(\Delta x)^2 + (\Delta y)^2 + (\Delta z)^2}}$$

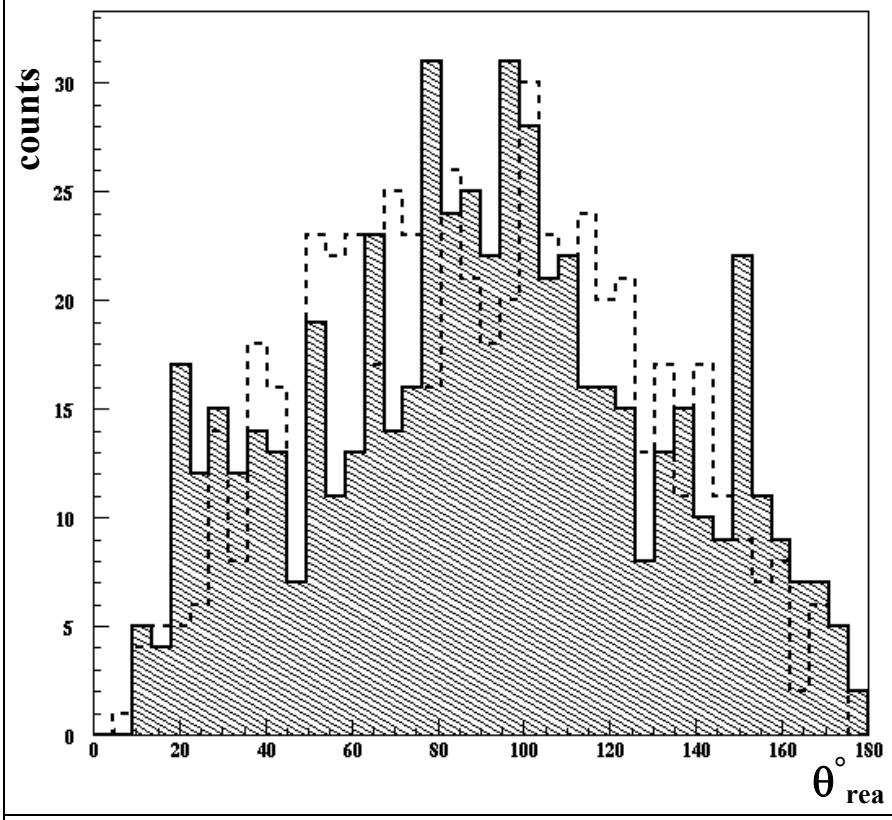

Fig.32. θ_{rea} of simulated (dashed line) and reconstructed (solid line) contained electrons

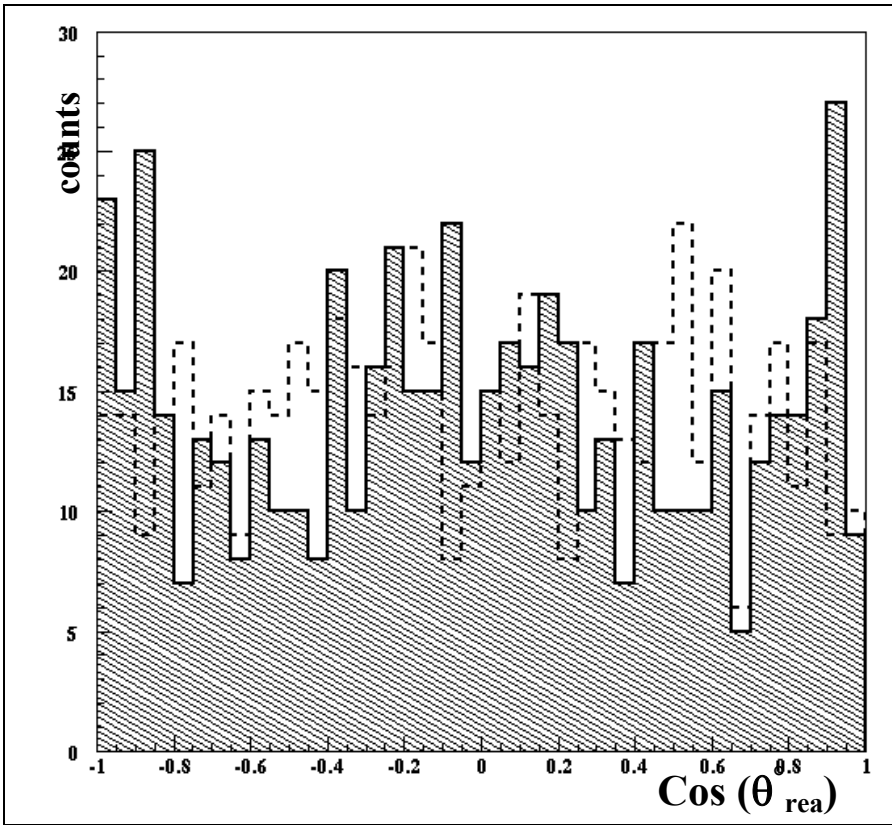

Fig.33. Cos (θ_{rea}) of reconstructed MC electrons

φ_{drea} (the angle between the reactor direction and the detector) is *-46.5* °, hence $cos(\varphi_{drea}) = +0.7$ and $sin(\varphi_{drea}) = -0.7$.

For an electron perpendicular to z ($\Delta z = 0$) and y ($\Delta y = 0$) axis (fig.29), one gets for $cos(\theta_{rea}) = +0.7$ $(\Delta x < 0)$ or $cos(\theta_{rea}) = -0.7$ $(\Delta x > 0)$.

For an electron perpendicular to z ($\Delta z = 0$) and x ($\Delta x = 0$) axis, one gets for $cos(\theta_{rea}) = +0.7$ $(\Delta y > 0)$ or $cos(\theta_{rea}) = -0.7$ $(\Delta y < 0)$.

Hence the number of the reconstructed events is smaller in the regions of:

$cos(\theta_{rea}) = +0.7$ (± 0.1), $(\theta_{rea} = +45° (\pm 10°))$ and

$cos(\theta_{rea}) = -0.7$ (± 0.1), $(\theta_{rea} = +135° (\pm 10°))$.

III.2. Global acceptance

The global acceptance is defined as a product between the acceptance of the visual scan and the containment efficiency

Global acceptance = Containment efficiency x Acceptance visual scan

III.2.1. Containment efficiency

To estimate the containment efficiency (in the 42 cm fiducial radius) we simulate electrons randomly in the TPC in the energy interval from **10 keV to 3000 keV**.

The containment efficiency was calculated as the ratio of the **contained electrons** to **all generated electrons**. It varies with the energy (see fig.34). At 700 keV the acceptance is 0.61, at 900 keV is 0.52, and at 1.5 MeV is 0.26.

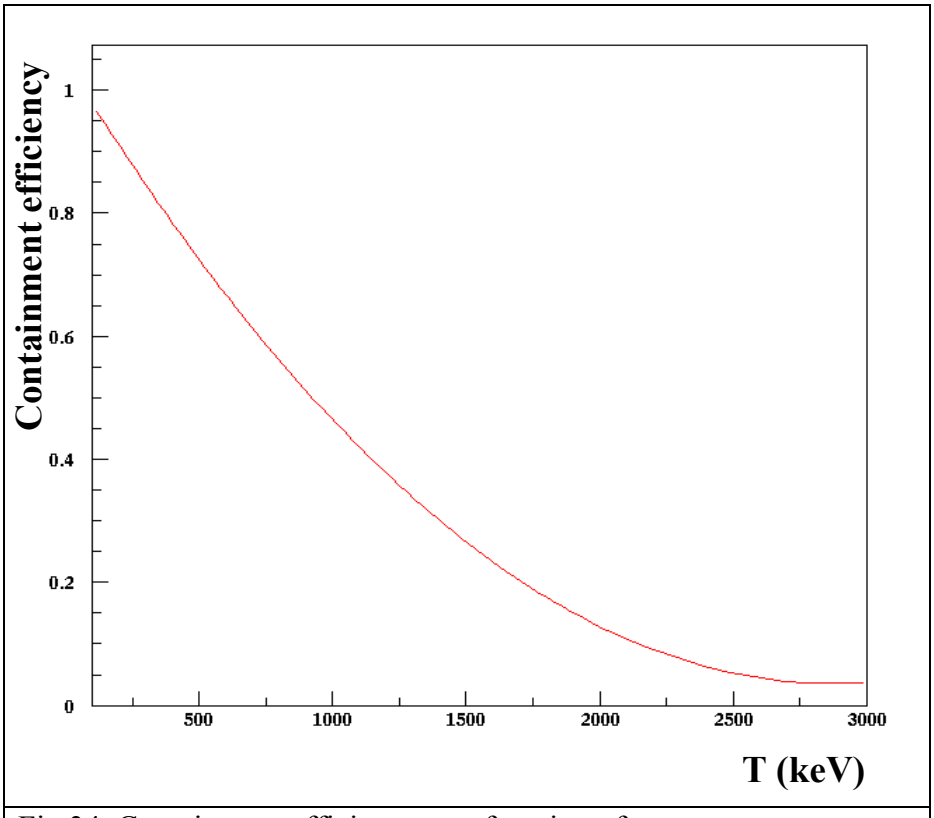

Fig.34. Containment efficiency as a function of energy

III.2.2 Acceptance of visual scan

The acceptance of visual scan (***Acceptance visual scan***) is a product of both the acceptance derived from scan of MC and the acceptance derived from the scan of real data

III.2.2.1 Acceptances of visual scan derived from MC samples

III.2.2.1 1. Acceptance in – out (*Acc. in–out*)

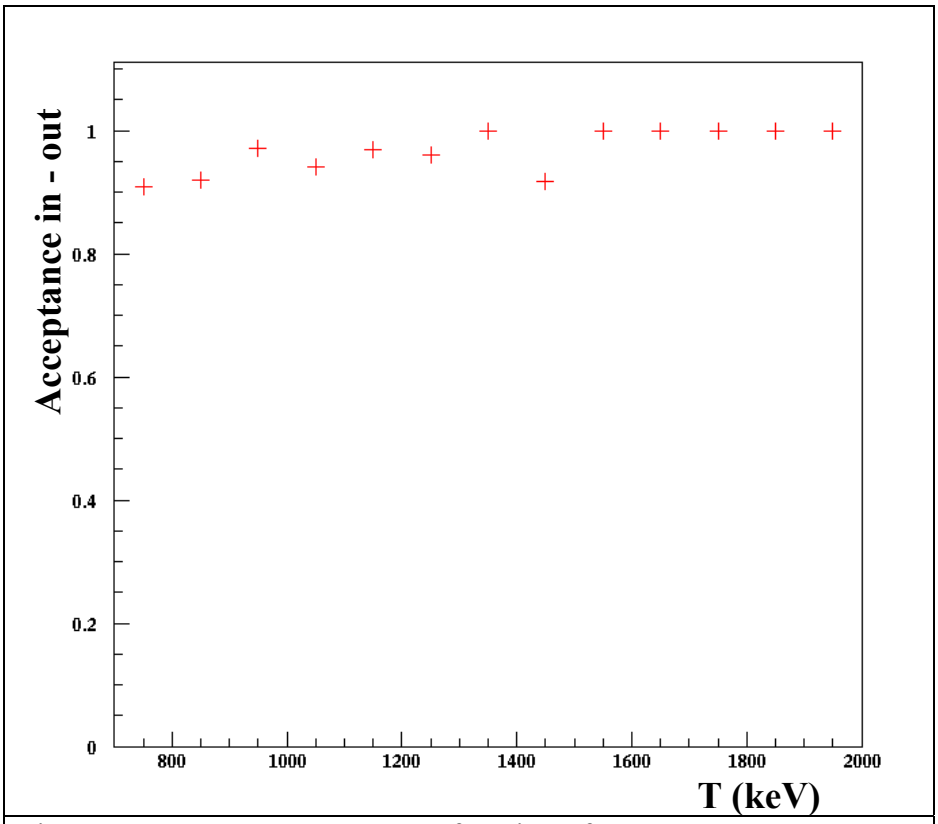

Fig.34. **Acceptance in – out** as a function of energy.

The electrons are generated randomly in the TPC in the energy interval from 700 keV to 2000 keV.

By definition the acceptance in-out **(*Acc. in-out*)** is the number of contained electrons found inside of the TPC of radius smaller then 42 cm (visual scan) divided by the number of generated contained electrons.

The average ***Acc. in-out*** of the visual scan is found to be 0.95 ± 0.08 and shows no energy dependence (see fig.34).

III.2.2.1.2. Acceptance of the visual scan to the neutrino events from the reactor (*Acc.* $E_\nu > 0$)

The acceptance of the visual scan to the neutrino events (***Acc.*** $E_\nu > 0$) is calculated by using MC electrons, which are generated in the energy interval from 700 keV to 2000 keV in the forward kinematical cone (Cf.III.1.2).

Acc. E_ν is by definition the ratio of the neutrino events which are found in the forward kinematical cone (visual scan) to the ones generated in the forward cone.

Acc. E_ν is found equal to 99.9%.

III.2.2.2. Acceptances of the visual scan derived from real data

The next two acceptances are derived from the scanning of the real data samples.

III.2.2.2.1. Acceptance geometry (*Acc. geometry)*

The acceptance geometry (Cf. III.1.2) is the ratio of the numbers of the events which are good to be reconstructed to the total numbers of the events.

It gives an acceptance of 0.96 ± 0.008.

III.2.2.2.2. Acceptance θ_{det} (*Acc.* θ_{det})

This acceptance is due to the activities which are larger at the anode side than those registered at the cathode side (Cf. III.3.3). Only the electrons from the cathode are accepted in the present analysis.

It gives an acceptance of 50 %.

In summary the acceptance of the visual scan for 3-bar is

$$\textit{Acceptance visual scan} = (\textit{Acc. in-out}) \times (\textit{Acc. } E_\nu{>}0) \times (\textit{Acc. geometry}) \times (\textit{Acc. } \theta_{det})$$

$$\textit{Acceptance visual scan} = 0.95 \times 0.99 \times 0.96 \times 0.5$$

$$\textit{Acceptance visual scan} = 0.45 \pm 0.08$$

III.2.3. Expected rate

The number of the interactions ***N*** in the TPC from electron antineutrino scattering (expected rate of recoil electrons) is given by

$$N = tn_e\phi\int_T^\infty\int_E^\infty\left(\frac{\partial\sigma}{\partial T}\right)_{E_\nu} N(E_\nu)dE_\nu dT \qquad (32)$$

In (32) the following parameters are considered:

t is the live time of the data taking

$\boldsymbol{n_e}$ is the number of the target electrons (3 x 10^{27} for 3 bar of CF4), which is a function of the pressure and volume of the TPC

$\boldsymbol{\phi}$ is the antineutrino flux at the detector location (10^{13} ν cm^{-2} s^{-1}). The reactor average power is found 2775 MWth and the distance between the detector and the reactor core is 18 m.

$\frac{\partial\sigma}{\partial T}$ is the electron antineutrino differential cross section, calculated by [19].

$\boldsymbol{N(E_\nu)}$ is the number of the neutrinos, emitted per keV and per fission. The fission fragments average contribution over an annual reactor cycle is: ^{235}U (60 %), ^{239}Pu (28 %), ^{241}Pu (5 %), ^{238}U (7 %) plus the additional contribution from neutron activation $^{238}U_n$ and is calculated by[19, 21].

T is the electron energy threshold

$\mathbf{E_\nu}$ is the neutrino energy

E is the minimum neutrino energy for an electron energy **T**

The calculated rate of the recoil electrons is folded with the detector resolution and is corrected by the global acceptance (Cf.III.2).

The energy resolution of the detector for 3-bar [36] follows the semi empirical law given by

$$\sigma(E) = \sigma_0\left(\frac{E}{E_0}\right)^{0.31} \qquad (33)$$

In (33) σ_0 and E_0 are the variance and the energy at 1MeV.

The total expected rate above 700 keV assuming zero magnetic moment is found to be 68.2 ± 13 counts for 66.6 days (fig.35), which gives 1.02 ± 0.19 counts per day.

The Monte Carlo error on the expected rate comes from uncertainties in the neutrino spectrum above 900 keV, reactor flux (5 %), detector containment (2 %), events with weird topologies that can not be reconstructed (4 %) and acceptance visual scan (8 %). The total uncertainty is of 19 % on the total expected rate.

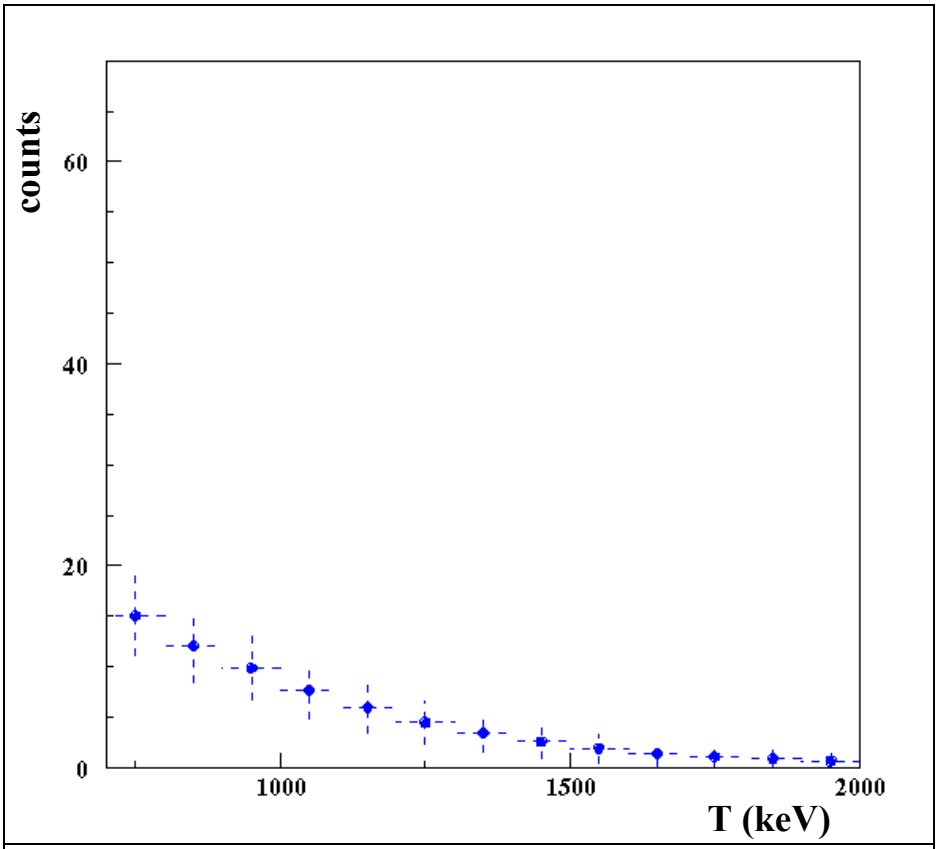

Fig.35. The expected electron recoil spectrum from weak interaction

III.3. Background in the TPC during 3-bar period

To select properly the neutrino candidates we have to understand the background in the detector during the 3-bar period. To do this we consider the following backgrounds:

III.3. 1. Radon background

The radon is a naturally occurring radioactive noble gas. It is produced by the radioactive decay of radium. It could be found in the worldwide atmosphere.

The decay chain of ^{222}Rn consists of daughter elements which have half-lives varying from seconds to years, as it shown in the Fig 36.

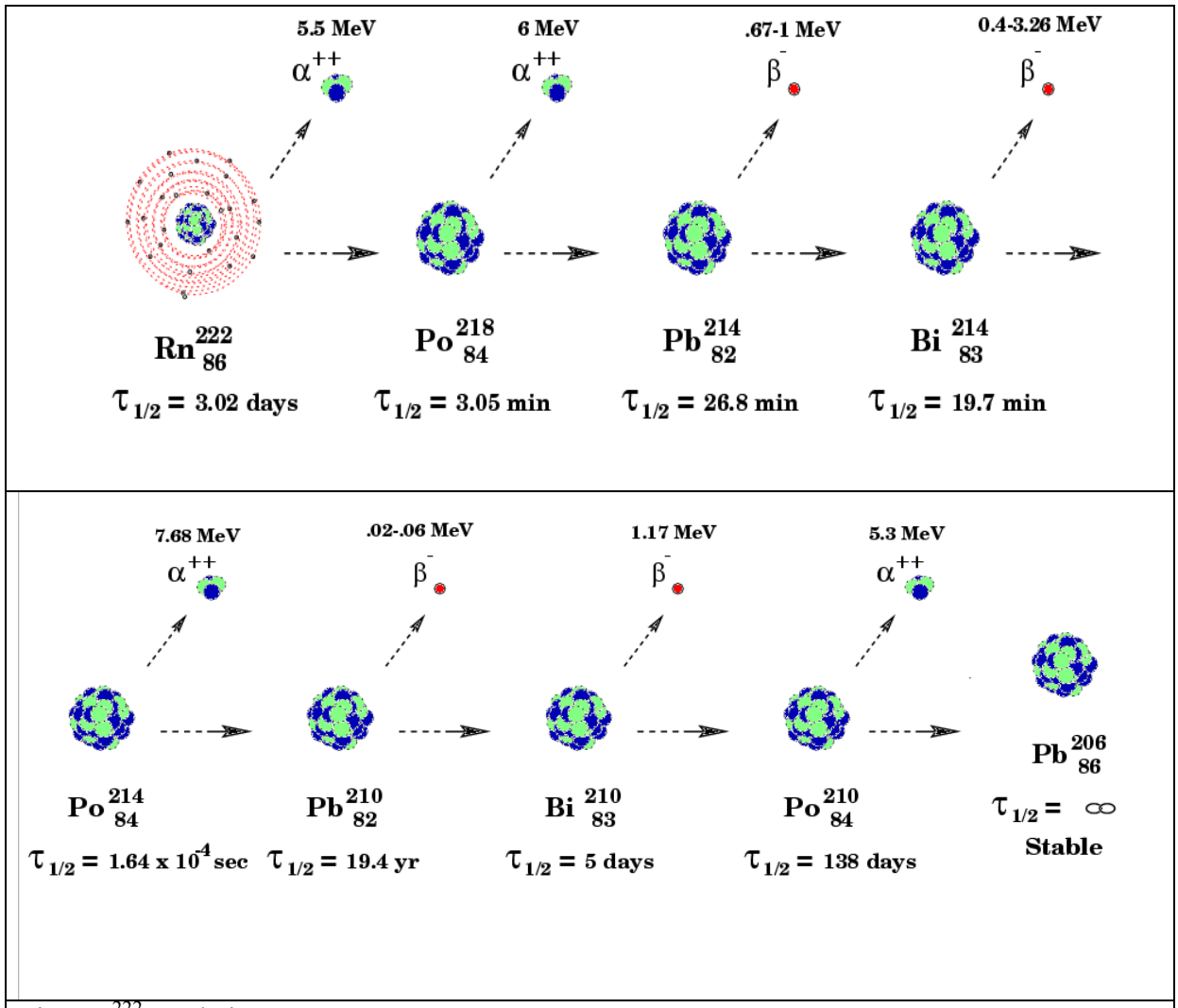

Fig.36. ^{222}Rn chain

The background from gas ^{222}Rn at a level of 0.7 mBq/m^3 was measured in the detector from the ^{214}Bi -^{214}Po decays (from the ^{222}Rn decay chain) [34]. In Fig.37, one such a coincidence is shown: the electron is from the β-decay of ^{214}Bi and the alpha is from the α-decay of ^{214}Po.

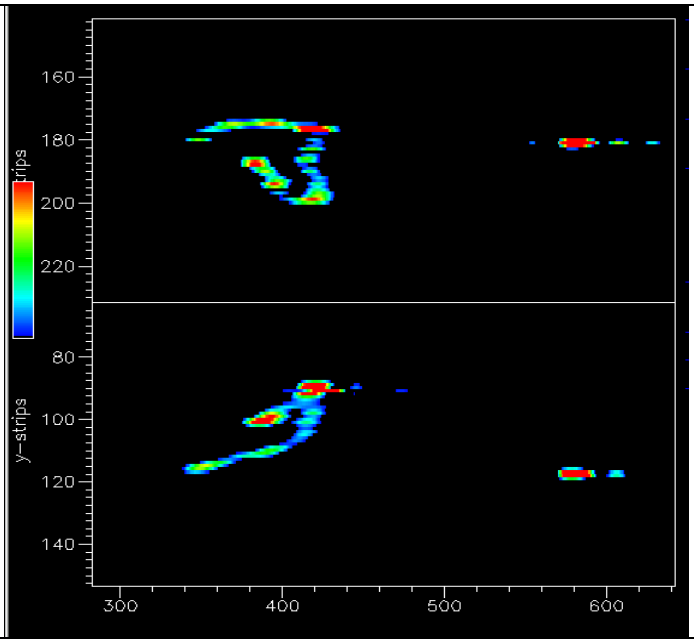

Fig.37.A beta-alpha coincidence. The electron is from the β-decay of ^{214}Bi and the alpha is from the α-decay of ^{214}Po.

III.3.2. Background from β emitters

In the atmosphere of every nuclear plant there are radioactive products from fission, namely gases ^{85}Kr and ^{133}Xe, which are mostly beta emitters. These gases could enter the TPC from the ventilation system of the nuclear plant, mostly during the time when the TPC is opened.

^{85}Kr is mostly beta emitter with the end point of beta spectrum at 687 keV and half-life of 10.7 years. It could not be stopped completely by the cold trap and purification system of the gas, because its boiling point (-153°C) is below the trap operation temperature (-80°). The estimated activity of ^{85}Kr is found to be 0.15 Bq/m^3 [36]

In the 3 bar analyses, ^{85}Kr is eliminated by setting an energy treshold of 700 keV above the endpoint. Furtheremore the forward–backward analyses, as well as the forward–normalized background analyses, eliminate the background online.

^{133}Xe is mostly beta emitter with the endpoint of beta spectrum at 427 keV and half-life of 5.2 days. His boiling point (-107 °C) is also lower than the temperature of the cold trap. But because of its very short life time (5 days), the quantity of the gas after 5 days is negligible. Hence ^{133}Xe does not lead to any increase of the background.

III.3.3. Background from the anode

An excess of events from the anode side was monitored during the 3-bar experiment (see Fig.38). This is possibly due to the greater complexity of the anode side: the grid, the potential wires, the anode wires, the x-y readout plane. On the contrary, the cathode itself is very simple, it is made from a very pure copper foil.

To eliminate the possible background from the anode side, we treated in the analysis only the electrons coming from the cathode side ($\cos\theta_{det} > 0$, $\theta_{det} < 90°$).

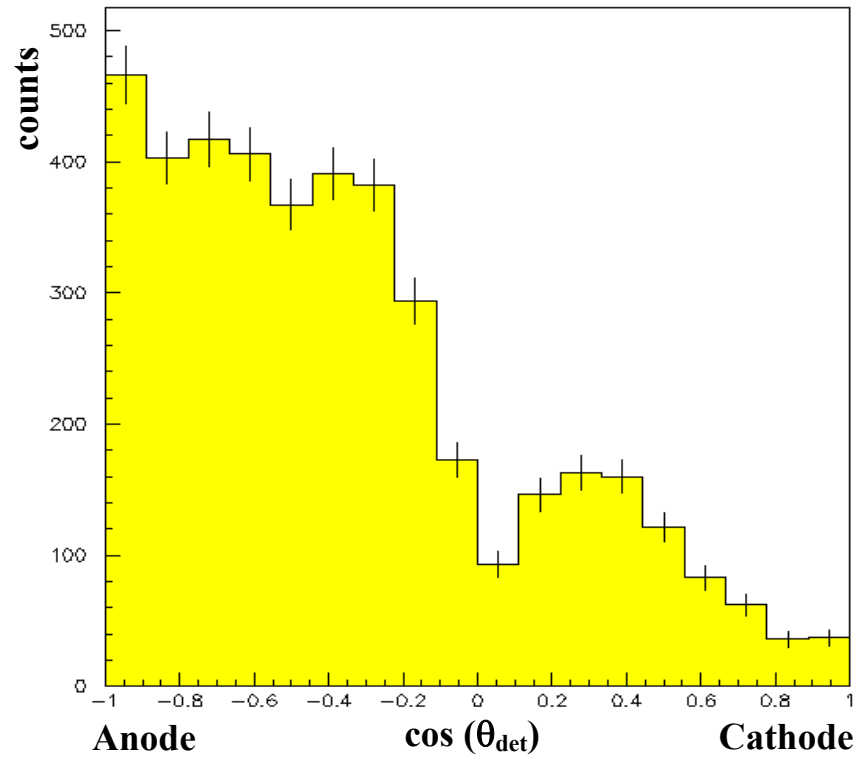

Fig.38. $\mathrm{Cos}(\theta_{det})$ distribution for the fully contained single electrons at 3-bar pressure

III.3.4. Background in the source direction

In order to estimate the background in the source direction we assume that the reactor is in the perpendicular direction, which coincides with the source direction, as one can see in Fig.39.

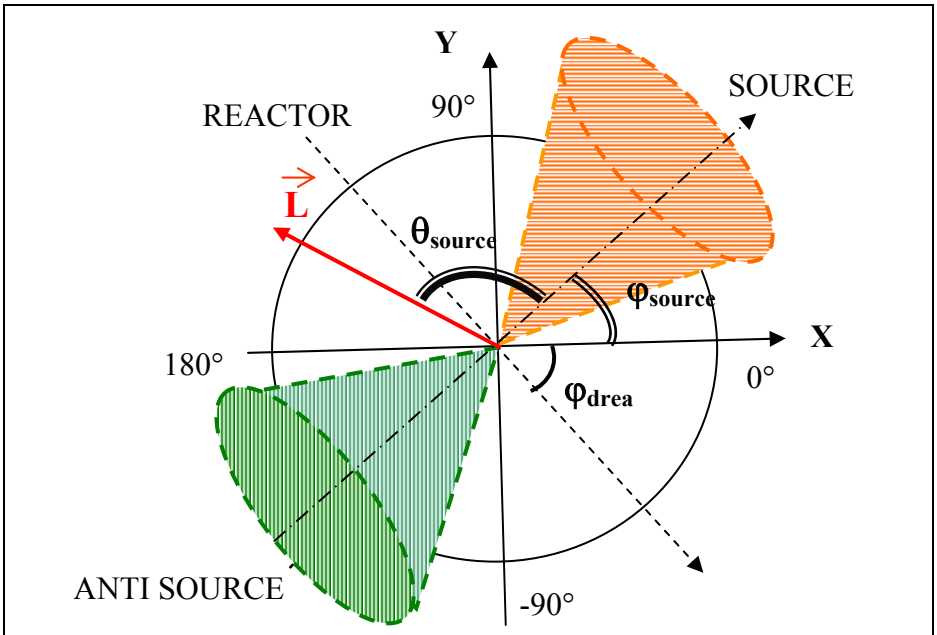

Fig.39. The source and anti source kinematical cones

In fact we rotate the reactor direction on +90°, so that φ_{drea}, which is equal to – 46.5° coincides now with φ_{source} = + 43.5° (see fig.38) and it is pointed from the bottom to the top in the source direction. The source and antisource cones are defined with the help of the neutrino initial energy E_ν (29) and scattering angle between the electron and the source direction θ_{source}. The angle θ_{source} is defined in the same way as θ_{reac} (14). Thus it is

$$\theta_{source} = \arccos \frac{\Delta y \cos\varphi_{source} - \Delta x \sin\varphi_{source}}{\sqrt{(\Delta x)^2 + (\Delta y)^2 + (\Delta z)^2}} \tag{34}$$

The neutrino initial energy is defined similarly to (29) as

$$E_\nu = \frac{m_e c^2}{\cos\theta_{source}\sqrt{\frac{T_e + 2m_e c^2}{T_e} - 1}} \tag{35}$$

In (35) θ_{source} is the angle between the electron direction ($\vec{L}$) and the source direction (see fig.39).

The neutrino energy is positive, hence the maximal scattering angle is

$$\theta_{source\max} = a\cos\sqrt{\frac{T_e}{T_e + 2m_e c^2}} \tag{34}$$

The source cone is defined in the interval: $0 < \theta_{source} < \theta_{sourcemax}$, while the antisource cone is defined in the interval: $\pi - \theta_{sourcemax} < \theta_{source} < \pi$. Note please that the source kinematical cone coincides with the source position, because of the orientation of the axis in the source direction from the bottom to the top. The source electrons which are inside of the source kinematical cone presented at the top in fig.39 are those that have positive neutrino energy $E_\nu > 0$ and positive $\cos(\theta_{source}) > 0$. In the source cone there are only background events (few events from neutrino electron interactions can be neglected at energy above 700 keV). The antisource electrons which are inside of the antisource kinematical cone presented at the bottom in fig.39 are those that have positive neutrino energy $E_\nu > 0$ and negative $\cos(\pi - \theta_{source}) < 0$. In the antisource cone there are only the background events (the few events from neutrino electron interactions can be neglected at energy above 700 keV).

We will make now quantitative analysis for the source and anti source electrons.

III.3.4.1. φ_{det} and $\cos(\theta_{rea})$ distributions of the source and antisource electrons

The φ_{det} and $\cos(\theta_{rea})$ distributions of the source and antisource electrons are given in the fig.40 and fig.41, respectively. The source and anti source electrons are marked on these figures.

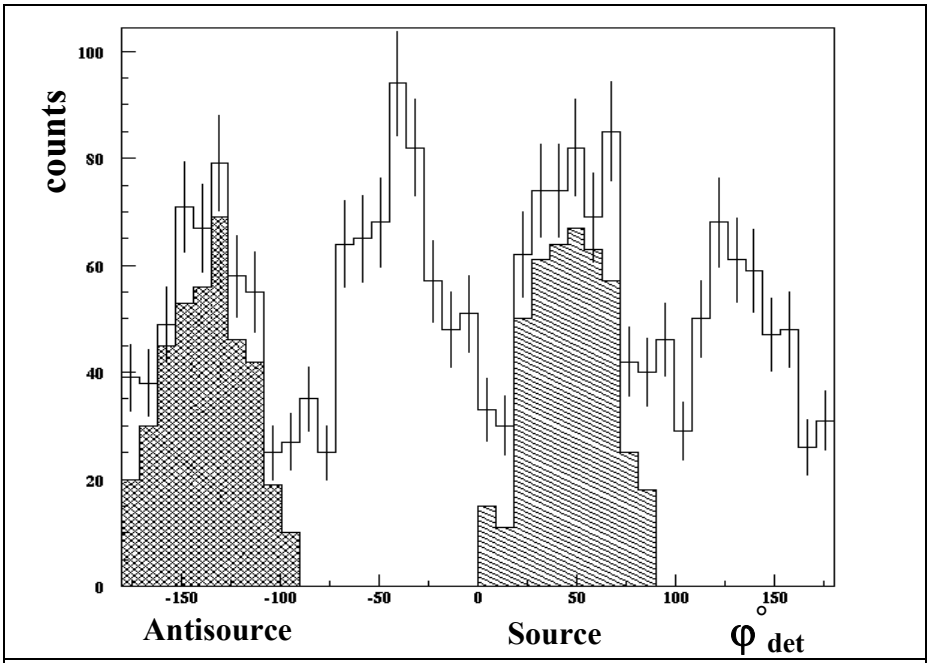

Fig.40. φ_{det} distribution of source (right) and antisource (left) electrons.

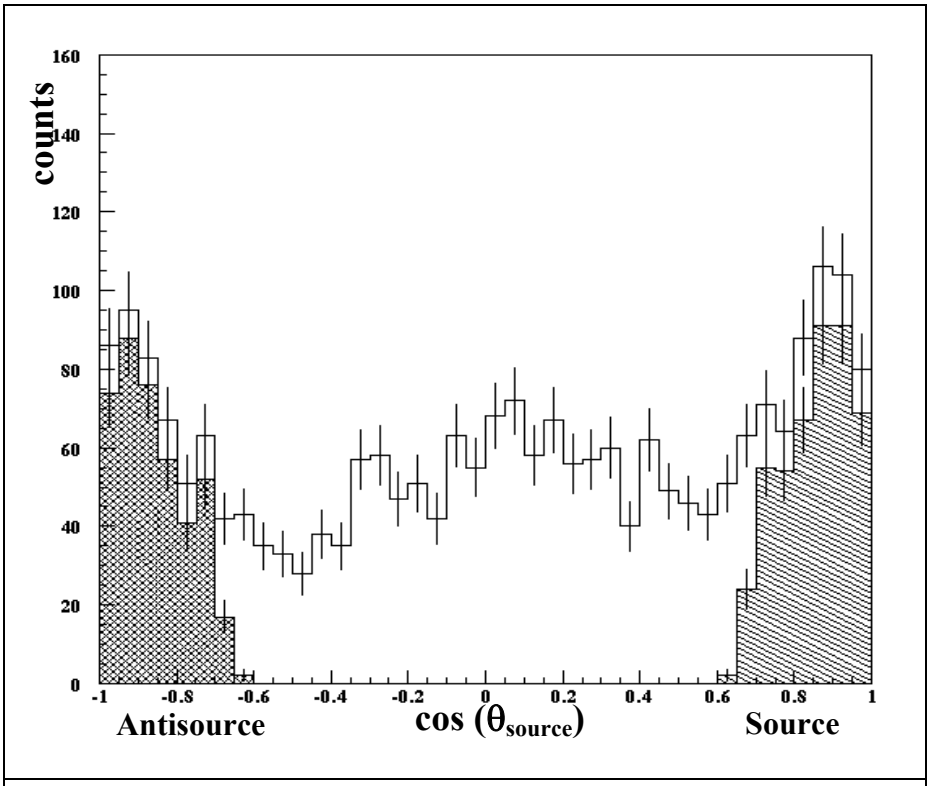

Fig.41. Cos (θ_{source}) distribution of the contained electrons. Source (right) and antisource (left) electrons are marked by pattern.

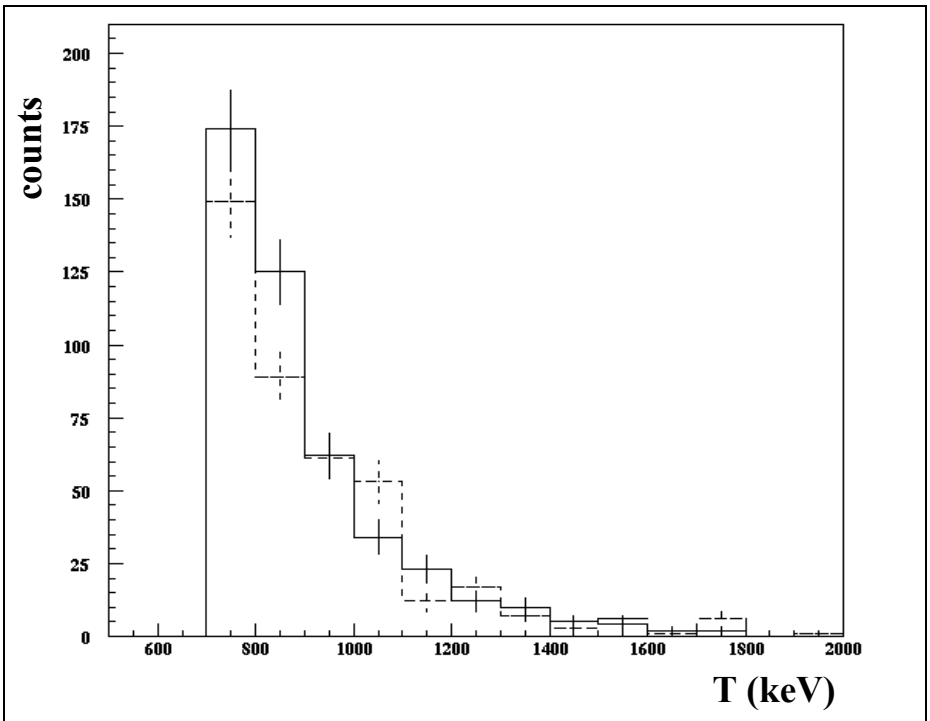

Fig.42. Energy distributions of source (solid line) and antisource (dashed line) electrons.

III.3.4.2. Energy distributions of the source, antisource and source minus antisource electrons

The energy distributions of the source (433 counts), antisource (390 counts) electrons (see fig.42) and source minus antisource electrons (fig.43) showed a little asymmetry in the background in the source direction. The difference is 43 ± 29 counts, which statistically is close to 0.

We can see from fig.43 that there is an excess of events in the source direction in the first two channels; 700 keV and 800 keV, respectively.

It is safer thus to make the analyses at the energy above 900 keV in order to reject the asymmetrical background in the source direction. At energy above 900 keV, for instance, the difference is -11 ± 26 and the result is completely consistent with zero.

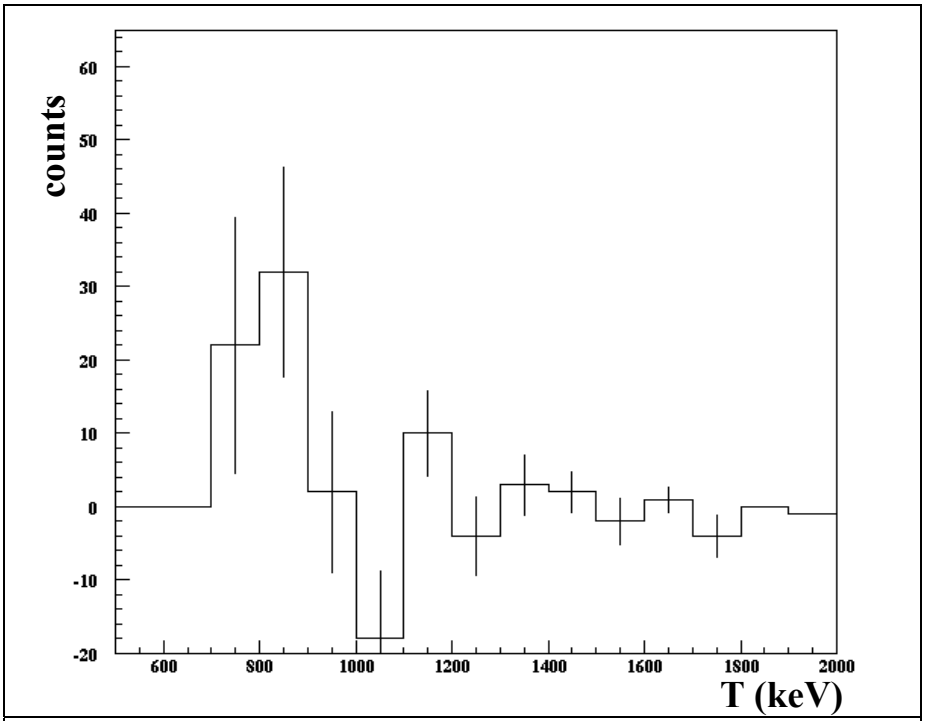

Fig.43. Energy distributions of source minus anti source electrons.

III.3.5. Background in the reactor direction

We consider the following background in the reactor direction [34].

background in the liquid scintillator

About 52000 neutrons per day are produced by $\bar{\nu}_e + p \rightarrow e^+ + n$ reaction in the liquid scintillator. This background is vetoed (the neutrons are captured by hydrogen nuclei in the scintillator and produced a 2. 2 MeV gamma rays).

background in the TPC acrylic vessel

The free protons in the TPC acrylic vessel would lead to $\overline{\nu}_e + p \rightarrow e^+ + n$ reaction. This background is vetoed by the fiducial volume cut of 42 cm radius;

background in the CF4 gas

The reaction $\overline{\nu}_e + p \rightarrow e^+ + n$ from the free protons in pure CF_4 (in the TPC) is excluded, because there are no free protons in the gas. In case if there are any, however, they will be vetoed by gamma rays following the positron annihilation.

Moreover, the reactor associated neutron flux in the Bugey laboratory has been measured and found to be negligible [39].

Therefore, an excess of events in the reactor direction will be assigned with electron antineutrino –electron interaction ($\overline{\nu}_e e^-$).

III.3.6. Fluctuations of the background during the 3-bar period

The background was monitored during the run time of data taking.

For the monitoring of the background we select only the electrons that are inside of the backward, source and antisource kinematical cones.

The backward cone is defined in (Cf. II.2.1), while source and antisource kinematical cones are defined in (Cf. III.3.4).

In the backward cone there are only background electrons. In the source and antisource cones we will consider only the background electrons, as far as the electrons from electron neutrino interactions are found to be negligible.

The reactor-on period that corresponds to 66.6 live days is divided in 12 intervals of 5.5 live days each. The reactor-off period that corresponds to 16.7 days is divided in 3 intervals of 5.5 days. In summary there are 15 intervals in total for 83 live days reactor-on plus reactor-off.

The final number of electrons ($\mathbf{N_{final}}$) in each 5.5 days interval is calculated by

$$N_{final} = \frac{\sum_{n=1}^{11} \left(N_{\text{int.electrons}} \times Cont.efficiency \right)}{N_{cont.electrons}} \qquad (37)$$

In (37):

- $\mathbf{N_{int.electrons}}$ is the number of electrons per energy interval. There are 11 intervals of 100 keV (the energy scale is settled from 700 keV to 1800 keV).

- **Cont. efficiency** is the containment efficiency of the detector for 3-bar pressure (Cf. III.2.2)

- $\mathbf{N_{cont.electrons}}$ are the number of all contained electrons in each 5.5 days interval.

Thus, the number of the final events has been normalized per energy, containment efficiency and number of contained electrons in every 5.5 days interval.

For sake of clearness the result is presented in Fig.44.

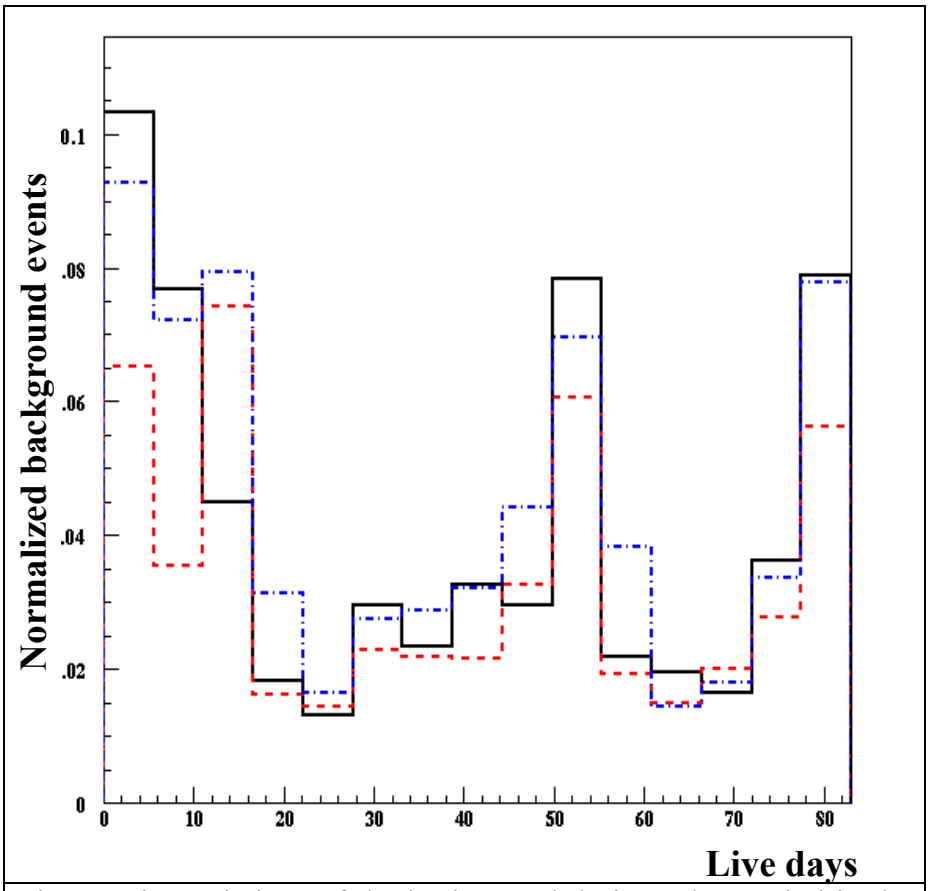

Fig.44. The variations of the background during 3-bar period in the source (blue doted dash line), antisource (black solid line) and backward cone (red dashed line).

In fig.44 one can notice some fluctuations in the background during the reactor on (from 0 to 66.7 live days) and reactor off (66.6 to 83 live days) periods. Indeed, the background decreases firstly with a minimum at the 25th live day, increases secondly with a maximum at the 50th live day, decreases again with a minimum at the 65th live days and increases finally at the 80th live day.

These fluctuations, however, have no direction, because they are identical for the backward electrons, as well as for the source and anti source electrons.

Therefore, the background fluctuations originate from the gas itself and are not due to the detectors artefacts.

III.4. 3-bar data analysis

The goal of the presented here analysis is to select neutrino candidates and to suppress the background. The selected neutrino candidates are compared with the expected ones. From this comparison limits on the magnetic moment of the electron antineutrino are derived.

The data sets are recorded by the MUNU TPC at 3 bar pressure (11.4 kg of CF4).

Two periods of operation of the reactor, reactor-on and reactor-off, are analysed. Furthermore, the data sets correspond to 66.6 live days reactor-on and 16.7 days reactor-off. Moreover the reactor-off data were recorded just after the reactor-on period.

III.4.1. Automatic data filtering

The selection of good events (contained single electrons) is firstly done trough an automatic data filtering by applying to the data sets the following filters (Cf.II.1):

- energy filter of 150 keV;
- muon filter;
- Anti Compton filter:
- filters for rejecting alphas, uncontained (R>42cm);
- energy filter of 300 keV;
- energy filter of 700 keV;

Summary of the above filters and filters efficiencies [34, 35], as well as the rates obtained for the **reactor –on** data, is given in the table below.

Automatic filtering	**Counting rate for 66.6 days**	**Counting rate per sec**	**Efficiency of the filter**
Anode 150 keV	5.75×10^8	100 Hz	-
Veto muons	5.75×10^6	1 Hz	98%
Veto Anti Compton	2.87×10^6	0.5 Hz	99%
300 keV	0.29×10^6	50 mHz	-
700 keV	2.9×10^4	5 mHz	-

The live time is derived during automatic data filtering and is found to be around 65%. It is limited, in fact, by the total veto time of the scintillator (11 %) and the dead time of the TPC itself, being due to relatively long data read-out and data transfer time (24 %).

III.4.2. Visual scan of the events above 700 keV

Here we present an analysis of the experimental data which is based on the visual scanning procedure, whose principles are already explained in Chapter II.

The work is essentially done at electron energies above 700 keV. This has two principle advantages: minimization of the scanning load, which is time consuming and rejection of the background from ^{40}Kr (with endpoint of 700 keV).

Selection of the neutrino candidates

By definition **neutrino candidate** is every single electron with clearly distinguishable start and end (blob) that answers to the following two criterias:

to be inside of the fiducial volume of the detector (R < 42 cm)

to have an angle θ_{det} smaller then 90°

The energy distribution of all fully contained electrons above 700 keV (reactor-on) is presented in Fig. 45.

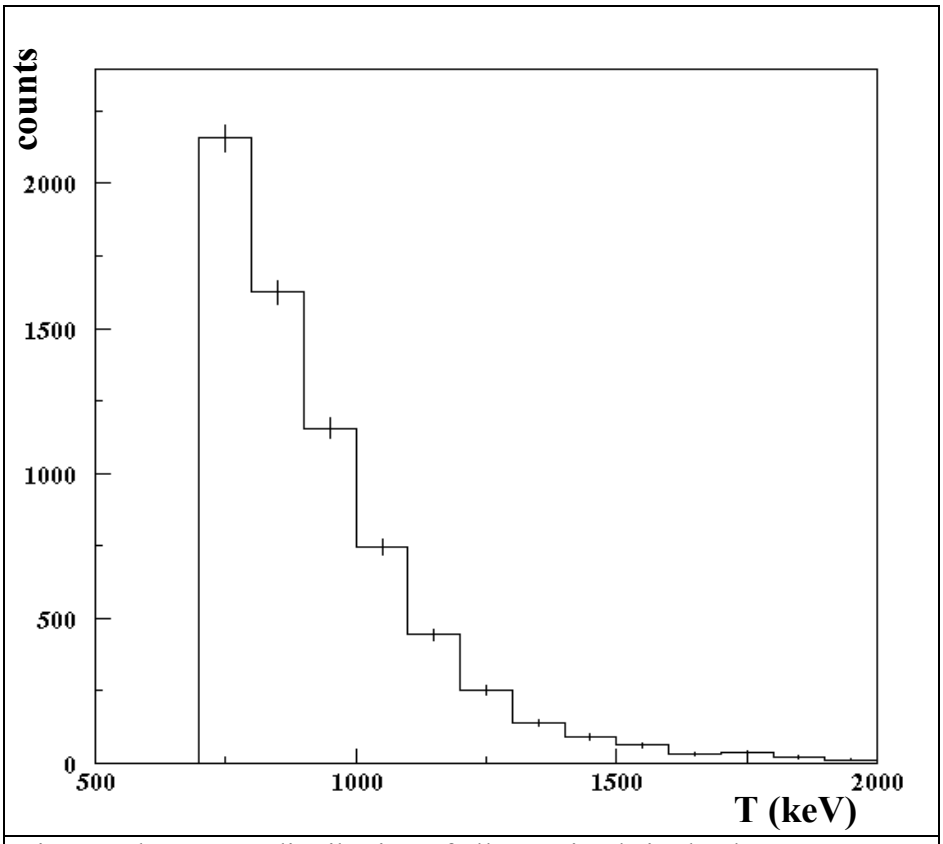

Fig.45. The energy distribution of all contained single electrons

The angular θ_{det} distribution of all fully contained electrons (reactor-on) above 700 keV is presented in Fig.46.

One can see from the plot that an excess of events from the anode side ($\theta_{det} > 90°$) dominates the counts rate. The reason of this excess was already explained (Cf. III.3.3).

In the present analysis only electrons from the cathode side ($\theta_{det} < 90°$) are accepted.

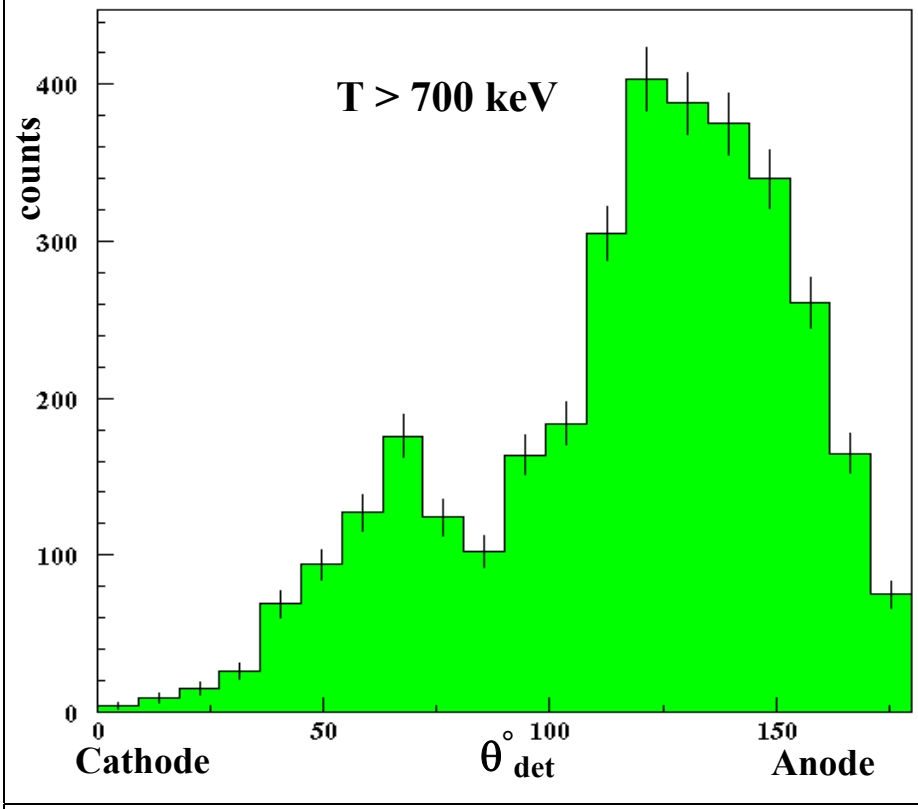

Fig.46. The angular θ_{det} distribution of contained single electrons

Summary of the filters and the rates obtained after selection of neutrino candidates are given in the table below.

Visual scanning	**Count rate for 66.6 days reactor-on**	**Count rate per sec**	**Efficiency**
single electrons	2.5×10^4	4.4 mHz	-
contained single electrons	2.2×10^4	3.9 mHz	95 %
$\theta_{det} < 90°$	3.9×10^3	0.67 mHz	50 %

III.4.3 Forward – Backward Analysis

The neutrino candidates are selected in Forward – Backward Analysis by comparison of the forward and backward electrons. The forward electrons (in the forward cone) are signal plus background events, while the backward electrons (in the background cone) are only background events (for definition of forward and backward kinematical cones see II.2.1).

III.4.3.1. Forward – Backward Analysis reactor - on

The analysed data set corresponds to 66.6 live days reactor-on.

III.4.3.1.1. φ_{det} and cos (θ_{rea}) distributions of single contained electrons

The φ_{det} and cos (θ_{rea}) distributions of all single contained electrons above 700 keV from the cathode side ($\theta_{det} < 90°$), together with the forward and backward electrons, are plotted in Fig.47 and Fig.48, respectively.

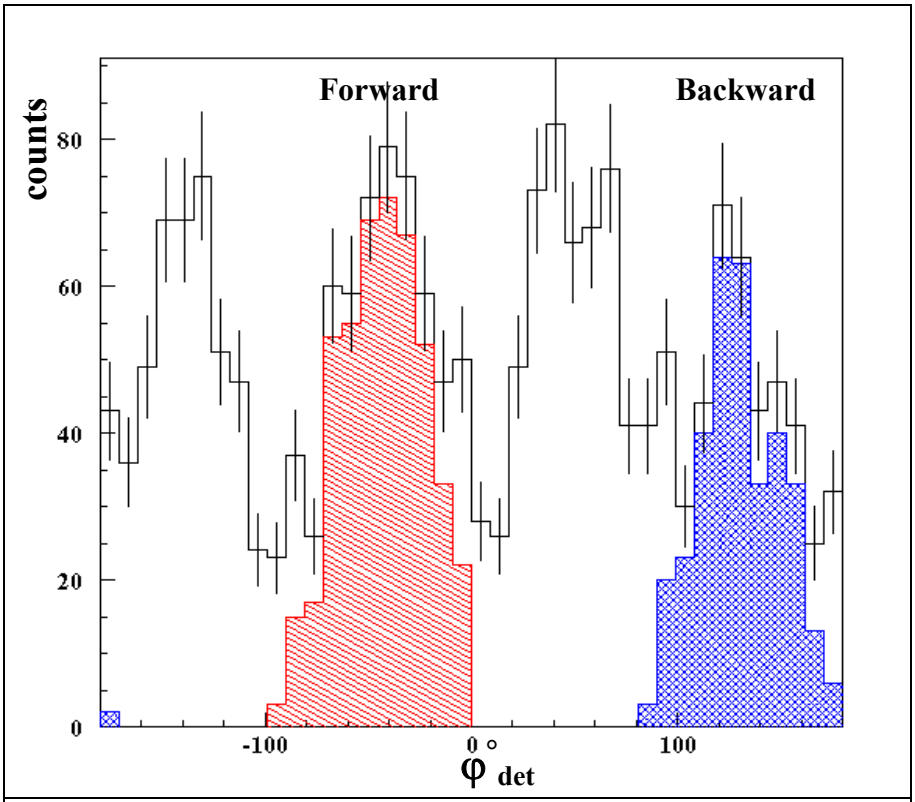

Fig.47. Distribution of φ_{det} (black line), forward electrons (left) end backward electrons (right) are marked.

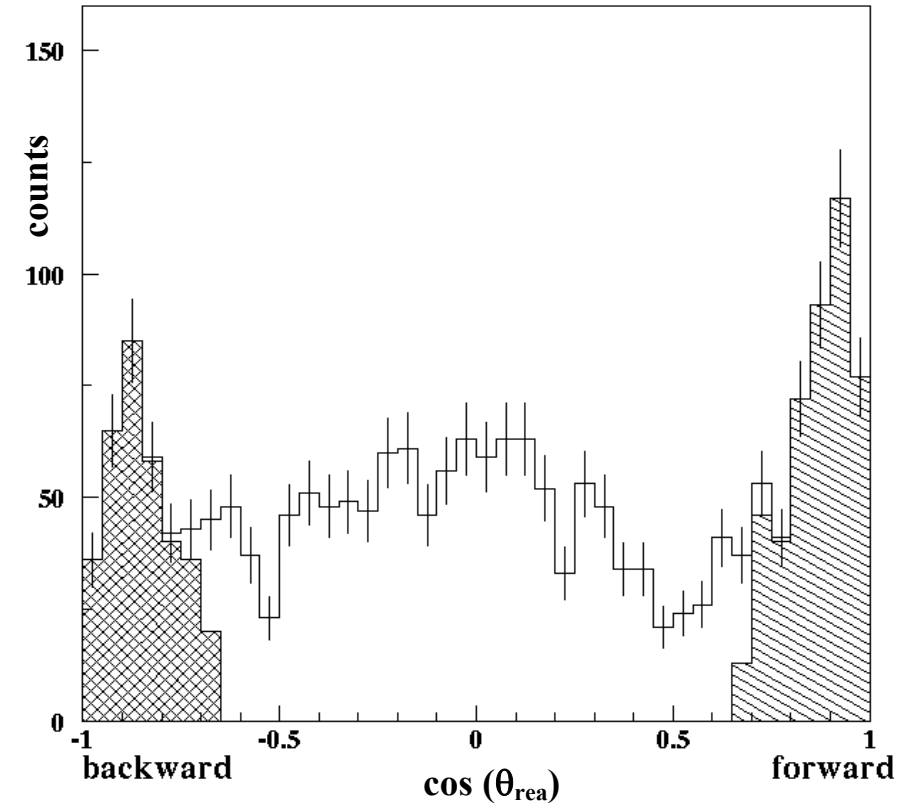

Fig.48. Cos (θ_{rea}) distribution of the single contained electrons reactor-on. The forward (right) and backward (left) electrons are marked by pattern.

The shapes of φ_{det} and cos (θ_{rea}) are deviate from the expected flat shape, because of the geometrical response of the detector. This was established from the scanned MC electrons (see III.1.2.).

There is a clear excess of electrons in the forward direction from the $\overline{\nu}_e e^-$ scattering in the reactor-on data. We calculated this excess. It is 458 forward events over 340 backward events.

III.4.3.1.2. Energy distributions of the forward and backward contained electrons

The energy distributions of both forward and backward electrons above 700 keV are given in Fig.49.

The total forward minus backward rate is 118 for 66.6 days reactor on above 700 keV, which gives 1.77 ± 0.42 counts per day (cpd).

The uncertainties from the gain instabilities, together with the live time and veto rate, are fully eliminated in the forward minus backward comparison.

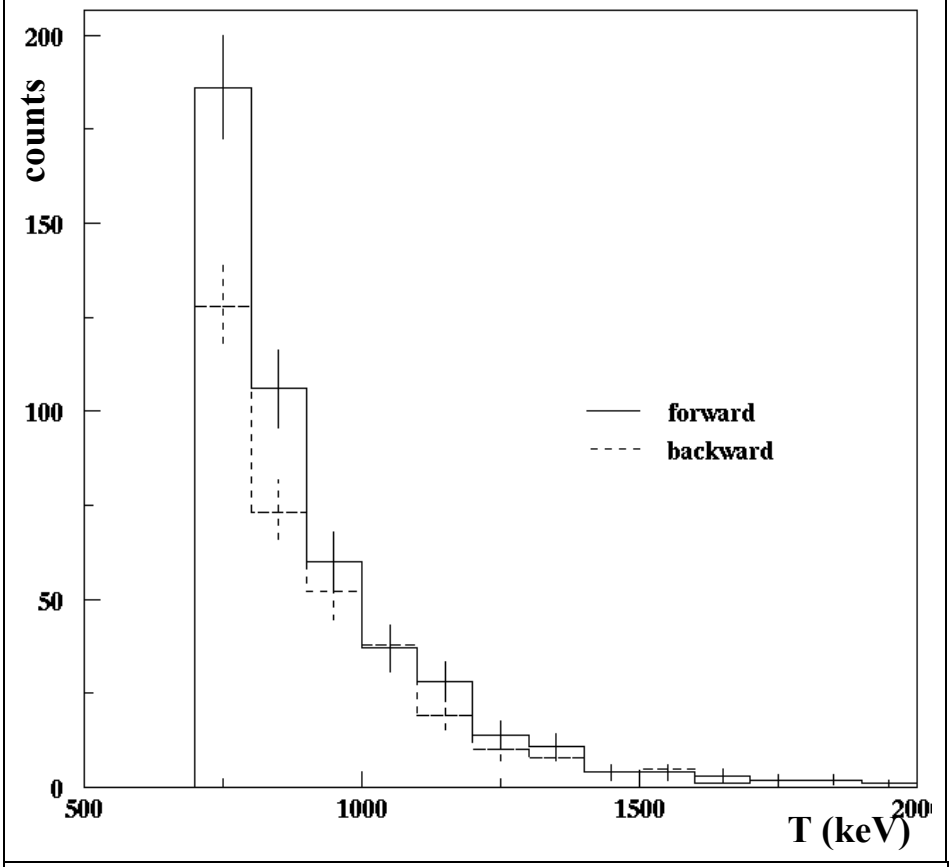

Fig.49. Energy distribution of forward and backward electrons, reactor on.

Now we will make the same forward - backward analysis for the reactor off data in order to cross check the results from reactor-on analysis.

III.4.3.2. Forward – Backward Analysis reactor - off

The reactor-off data set is recorded just after the reactor-on data set.

In the table below are given the filters and rates, which are obtained for the reactor-off data (16.7 days) after the visual scan of the events.

Visual scanning	Counting rate for 16.7 days reactor-off	Counting rate per sec
single electrons	8.3×10^3	5.7 mHz
contained single electrons	3.0×10^3	2.1 mHz
$\theta_{det} < 90°$	0.7×10^3	0.53 mHz

III.4.3.2.1. cos (θ_{rea}) distribution of single contained electrons reactor-off

The cos (θ_{rea}) distribution of single contained electrons above 700 keV from the cathode, together with forward and backward electrons, is shown in Fig.50. Here, in histogram, the forward (right) and backward (left) electrons are marked. The reactor-off distribution contrasts to the reactor-on data, where both forward (130) and backward (147) events are identical within the statistics.

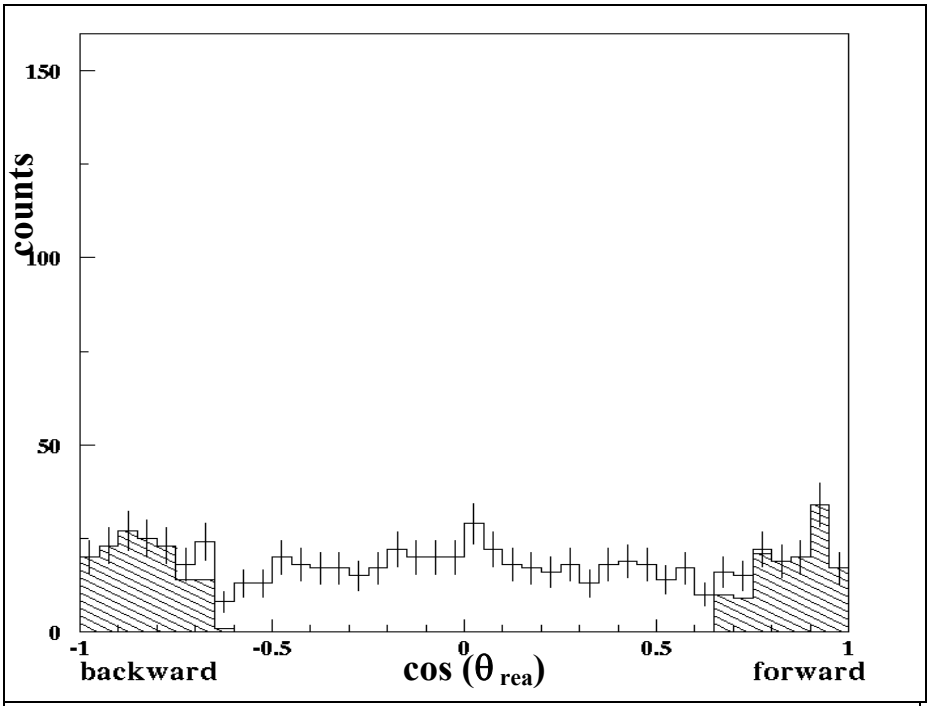

Fig.50. Cos (θ_{rea}) distribution of single contained electrons during reactor off. The forward and backward electrons are marked by pattern.

III.4.3.2.2. Energy distributions of forward and backward electrons reactor-off

The energy distributions of both forward and backward electrons are shown in Fig.51.

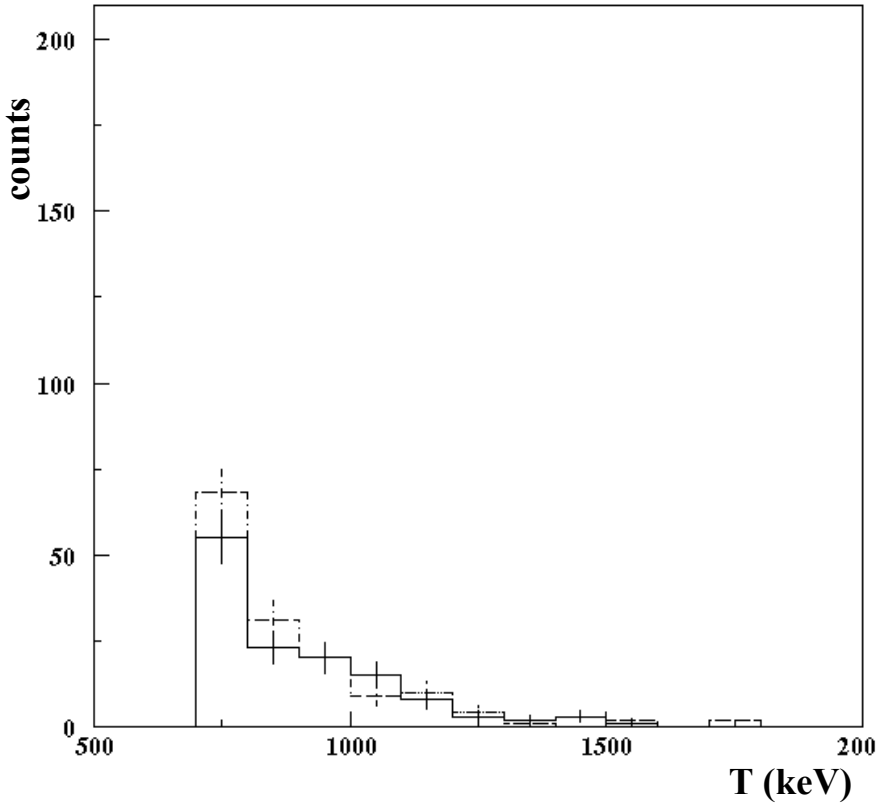

Fig.51. The energy distributions of forward (solid line) and backward (dashed line) electrons, reactor off

The total forward minus backward rate above 700 keV is -17 for 16.7 days reactor-off. The integrated forward minus backward rate above 700 keV is -1.02 ± 1.0 cpd, fully consistent with zero.

We conclude that there is no excess of the events from the reactor direction in the reactor-off period.

III.4.3.3. χ^2 analysis

We showed in the previous paragraph that in the reactor–off period no excess of events from the reactor direction is observed.

Thus we can conclude that the measured result in reactor-on, i.e. 1.77 ± 0.42 counts per day (cpd) (Cf. III.4.3.1.2) is due to neutrino interaction.

The expected rate was found to be 1.02 ± 0.1 cpd (Cf. III.2.3) consequently, we conclude that the measured result is about 1.7 σ higher than the expected one, but still compatible with the weak interactions.

Fig. 52 shows the energy distribution of the forward minus backward electrons. This result is presented together with the expected energy distribution from the weak interaction assuming zero magnetic moment ($\mu_\nu=0$).

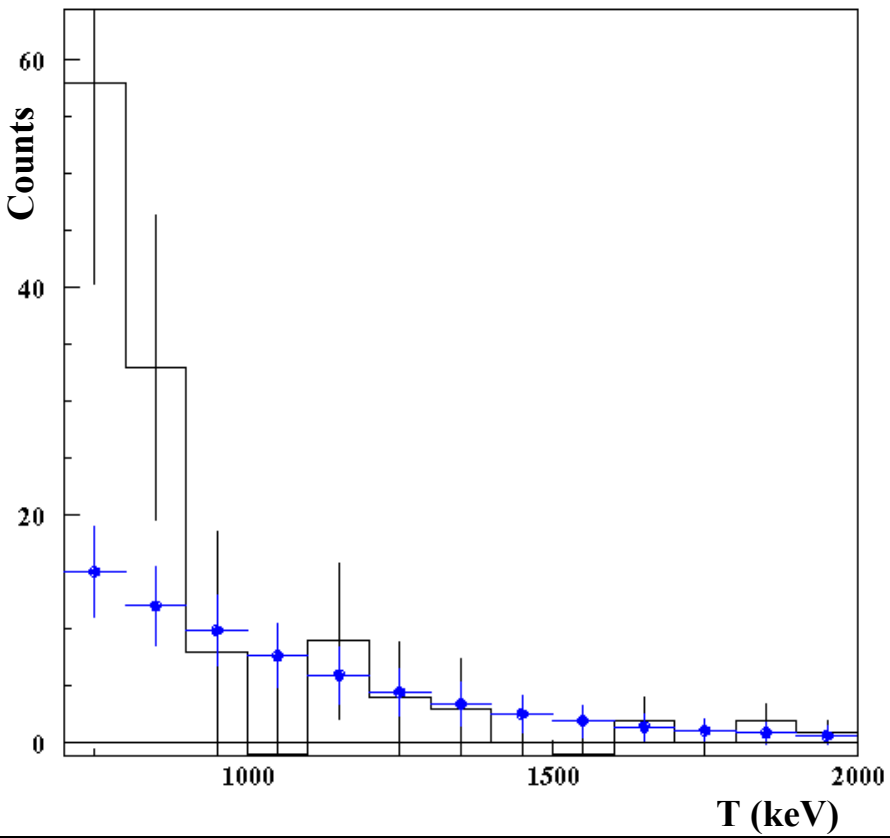

Fig.52. Energy distribution of forward minus backward electrons(solid line) as compared to the weak interaction μ=0 (blue circles), reactor on

We compare here the measured signal with the predicted one from the weak interaction (assuming $\mu_\nu=0$) by using χ^2 analysis [40], which is sensitive to both integral and shape of the spectra (see fig.52).

$$\chi^2(\mu^2) = \sum_{i=1}^{n} \frac{\left(Y_{i\exp} - Y_{ical}(\mu^2) \right)^2}{\left(\sigma_{i\exp} \right)^2} \qquad (38)$$

In (38) μ^2 is the squared magnetic moment, being varied as a free parameter, Y_{iexp} are the experimental points, Y_{ical} are the calculated points and σ_{exp} are the statistical errors of the experimental points (the errors of the expected points are smaller than the statistical errors, so that they can be neglected).

III.4.3.3.1. 700 keV analysis

To calculate χ^2 we divided the region between 700 keV and 1400 keV to 7 channels of 100 keV and the region between 1400 and 2000 keV to 1 channel of 600 keV (with this we avoided the small statistics in the upper channels). In this case the total number of channels is 8. We vary μ^2 as a free parameter; hence the degree of freedom (d.o.f.) is 7.

The result of χ^2 (μ^2) for the electron energy above 700 keV is presented in Fig. 53.

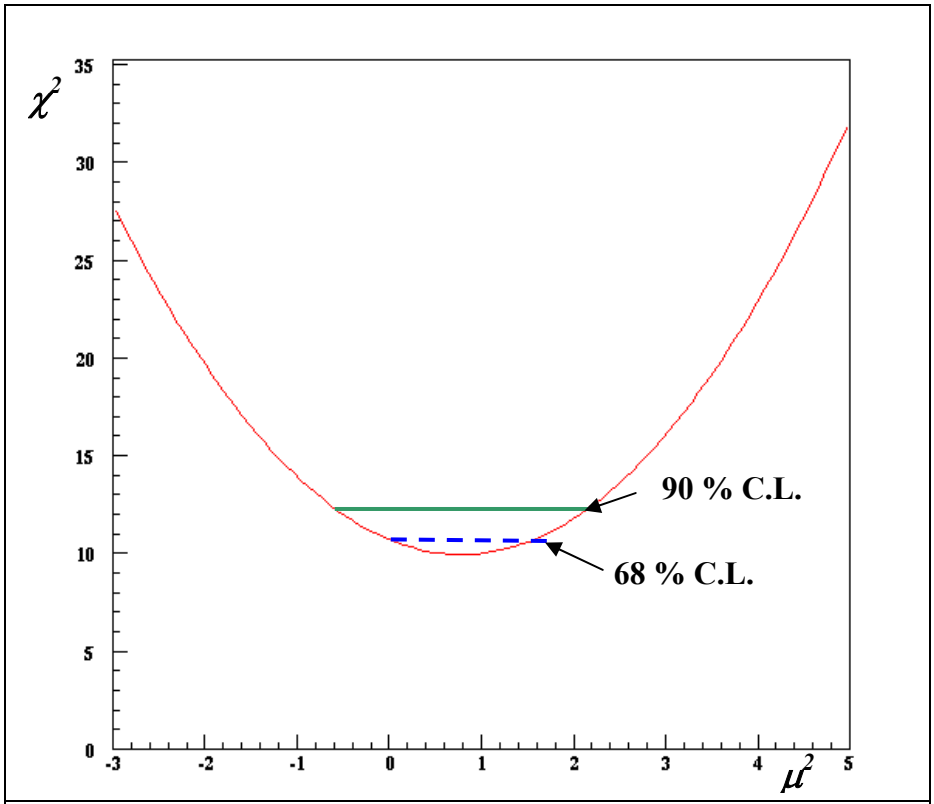

Fig.53. $\chi^2(\mu^2)$. 90 % C.L. (line) is shown together with 68 % C.L. (dash line).

The minimum of χ^2 is found to be 9.9. The squared magnetic moment μ^2 in the minimum of χ^2, μ^2 (χ^2_{min}) is 0.77 x 10^{-20} μ^2_B.

Furthermore, we found in the 68 % confidence interval $\mu^2 = 0.77 \pm 0.90 \times 10^{-20}\ \mu^2_B$ and in the 90 % confidence interval $\mu^2 = 0.77 \pm 1.5 \times 10^{-20}\ \mu^2_B$ (see Fig.53). The results are consistent with a zero magnetic moment.

We renormalize the above results to the physical region of μ^2 ($\mu^2 \geq 0$) (see for details [40]) with the help of a program [33] and find next limits: $\mu < 1.2 \times 10^{-10}\ \mu_B$ at 68 % C. L. and $\mu < 1.4 \times 10^{-10}\ \mu_B$ at 90 % C. L.

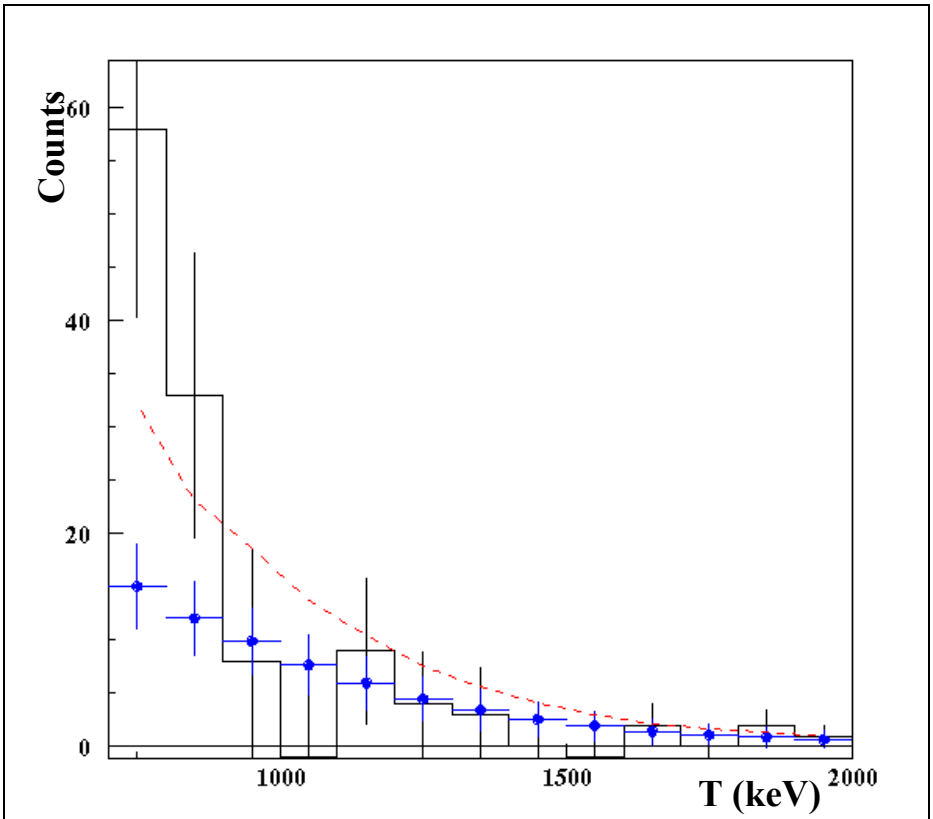

Fig.54. Energy distribution of forward minus backward (solid line) compared with weak interaction: $\mu=0$ (blue circles) and with weak plus electromagnetic interactions assuming a magnetic moment of $\mu=1.4.10^{-10}\mu_B$ (red dash line).

In fig.53 one can see that even the best fit is not satisfactory, because χ^2/d.o.f. = 9.9/7 =1.4 is high.

Moreover the accumulation of events in the first two channels (from 700 keV to 900 keV) makes the adjustment of the experimental and predicted spectrum (assuming zero magnetic moment) very difficult at the beginning (see fig.54).

Furthermore, as mentioned in Chapter I the low part of the neutrino spectrum (below 1500 keV), which contributes significantly to the electron spectrum below 900 keV, has never been measured. Only less precise calculations have been known up to now. The excess of events in the first two channels could result from an additional neutron activation that is beyond the value which one takes into account in calculations of the expected rate.

For the reasons mentioned above and, because of the monitored asymmetry in the background in the source direction (Cf. III.3.4), we restrict our analysis to the electron energy above 900 keV.

III.4.3.3.2. 900 keV analysis

The *cos* (θ_{rea}) distribution of all contained single electrons from the cathode above 900 keV is shown in Fig.55.

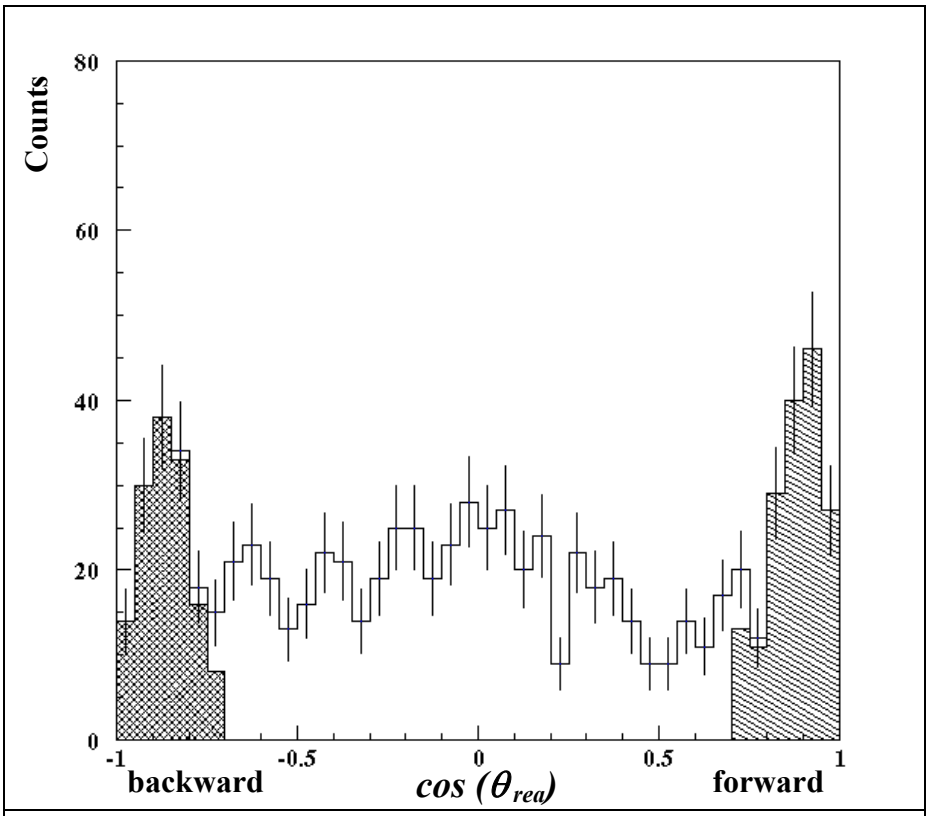

Fig.55. *cos* (θ_{rea}) distribution of single contained electrons above 900 keV. Forward (right) and backward (left) electrons are marked.

The energy distributions of forward (166) and backward (139) electrons above 900 keV is shown in Fig.56. The total forward minus backward rate is 27 for 66.6 days reactor on above 700 keV, which gives 0.41 ± 0.26 counts per day (cpd).

At $T_e \geq 900$ keV we have a good agreement between the measured 0.41 ± 0.26 cpd and expected rate 0.62 ± 0.05.

We calculate χ^2 by using the same method as before (Cf.III.4.3.3).

Indeed, we divided the region between 900 keV and 1400 keV to 5 channels of 100 keV and the region between 1400 and 2000 keV to 1 channel of 600 keV. Thus the total number of channels is 6; hence the degree of freedom is 5.

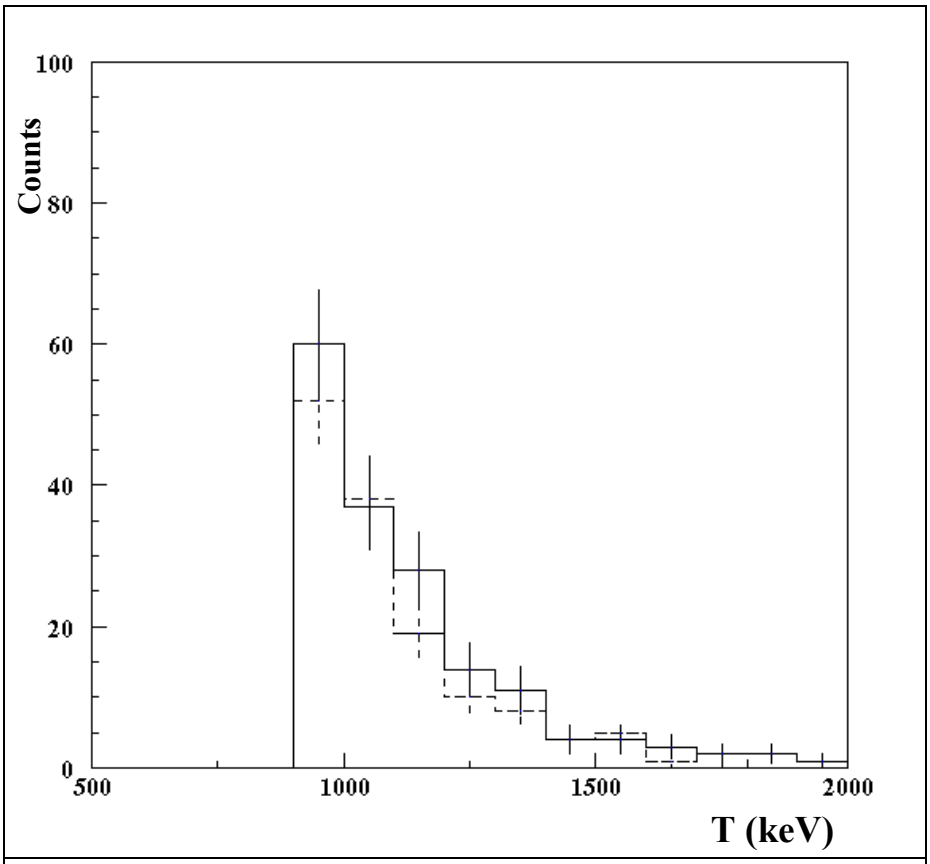

Fig.56. The energy distribution of forward (solid line) and backward (dashed line) electrons above 900 keV

The result of χ^2 (μ^2) for electron energy above 900 keV is presented in Fig. 57.

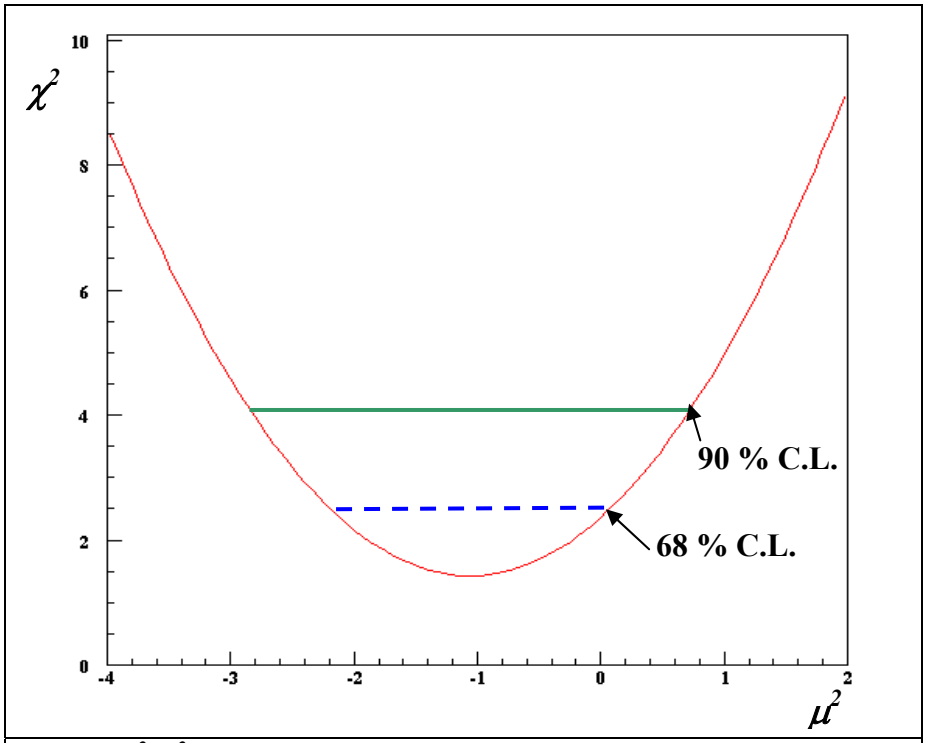

Fig.57. $\chi^2(\mu^2)$. 90 % C.L. (line) and 68 % C.L. (dash line) are shown.

The minimum of χ^2 is found to be 1.5.

The squared magnetic moment μ^2 in the minimum of χ^2, μ^2 (χ^2_{min}) is $-$ 0.95 x 10^{-20} μ^2_B. Moreover, we found in the 68 % confidence interval μ^2 = -0.95 ± 0.95 x 10^{-20} μ^2_B and in the 90 % confidence interval μ^2 = -0.95 ± 1.5 x 10^{-20} μ^2_B (see Fig.56).

This time the fit is very good. The best χ^2 is 1.5 for 5 degree of freedom, which gives $\chi^2/d.o.f.$ = 1.5/5 = 0.3.

We renormalize the above results to the physical region corresponding to $\mu^2 \geq 0$ and find the following limits:

μ < 0.8 x 10^{-10} μ_B at 68 % C. L. and **μ < 1.0 x 10^{-10} μ_B at 90 % C. L**.

The result of μ < 1.0 x 10^{-10} μ_B at 90 % C. L is shown in fig.58.

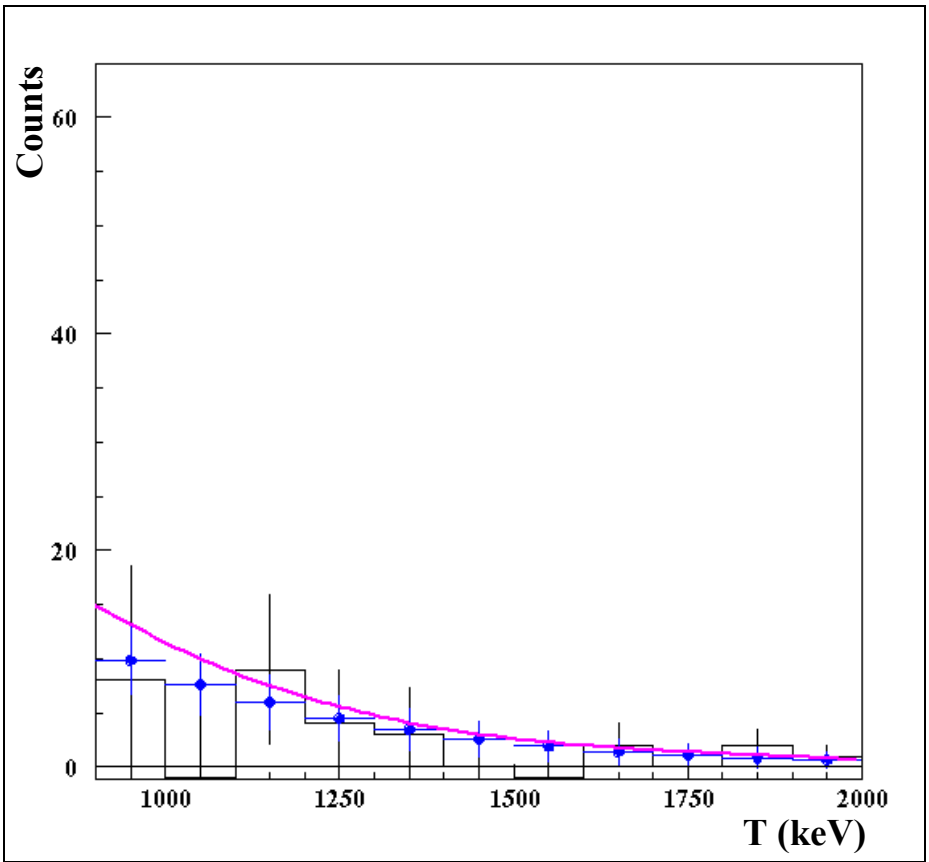

Fig.58. Energy distribution of forward minus backward (black solid line) as compared to the weak interaction (μ = 0, blue circles), and to the weak plus electromagnetic interactions assuming a magnetic moment of μ = 1.0 x $10^{-10}\mu_B$ (pink solid line) above 900 keV.

III.4.4. Forward – Normalized Background Analysis

Although the result of MUNU experiment ($\mu < 1.0 \times 10^{-10}\ \mu_B$ at 90 % C. L) gives recently the best laboratory upper limit of the magnetic moment of the electron antineutrino [41], we continue our efforts to improve the analysis.

In order to achieve this we proceed with a different analysis.

We select following four kinematical cones: **forward**, **backward**, **source** and **antisource** (see fig.58, Cf.II.2.1 and III.3.4).

We normalize the background in the backward, source and antisource cones considering that it is isotropic. Moreover, we have showed that the fluctuations of the background are the same in the three selected directions (Cf.III.3.f).

This, so called *normalized background*, will be subtracted later from the forward electrons.

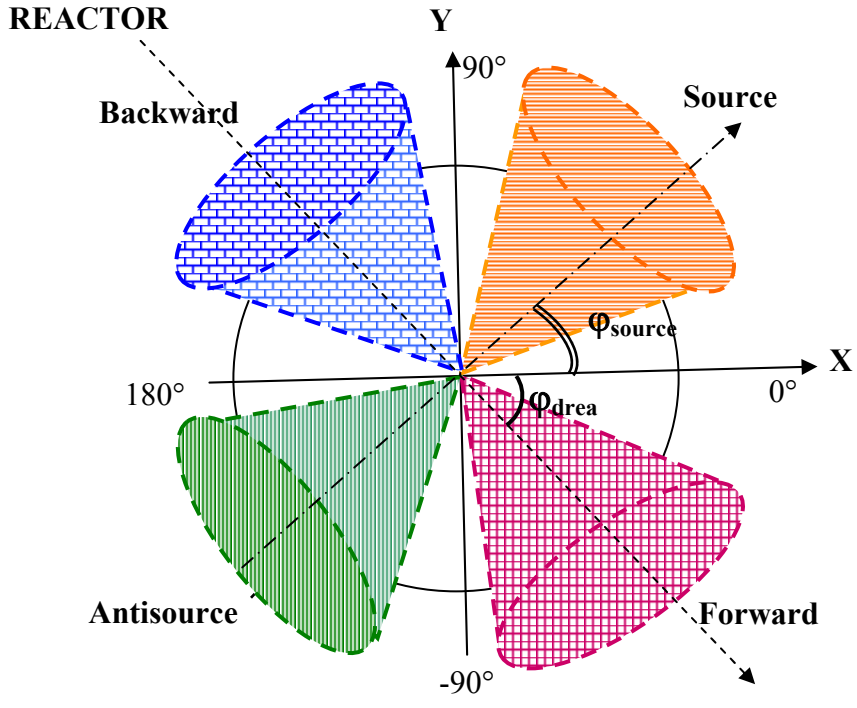

Fig.59. The source, antisource, forward and backward cones in *xy* plane

The source electrons (inside of the source kinematical cone presented at right top in fig.59), the antisource electrons (inside of the antisource kinematical cone, presented at the left bottom in fig.59) and the backward electrons (inside of the backward kinematical cone, presented at the left top in fig.59) are all background events.

Please note that the forward electrons (inside of the forward kinematical cone, presented at the right bottom in fig.59) are signal plus background events.

III.4.4.1. φ_{det} distribution of the contained electrons in four kinematical cones

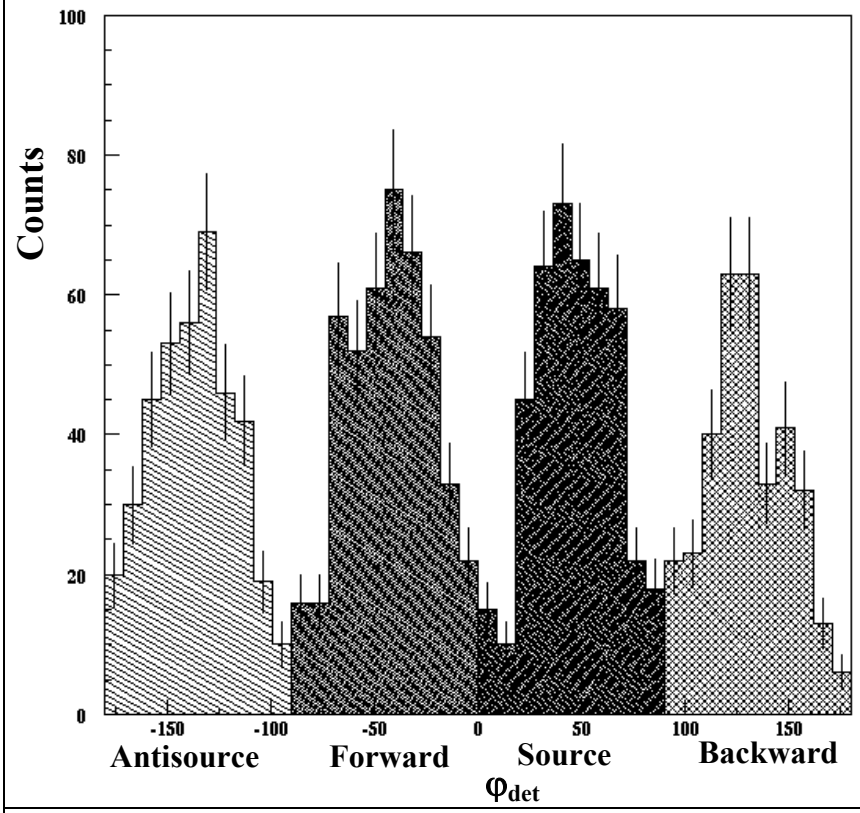

Fig.60. φ_{det} distributions of antisource, forward, source and backward electrons (from left to right).

In order to avoid an overlap of electrons contained in the four kinematical cons we define them in the next intervals of the φ_{det} angle:

- antisource electrons φ_{det} = [–180° ; –90°],
- forward electrons φ_{det} = [–90° ; 0°],
- source electrons φ_{det} = [0° ; 90°],
- backward electrons φ_{det} = [90°; 180°].

The non overlapped φ_{det} distribution of antisource, forward, source and backward electrons is presented in Fig.60.

The Monte Carlo simulations of forward electrons (from electron antineutrino scattering) determine that, the angular cut of angle φ_{det} = [–90°; 0°] has an acceptance of 99.6 % above 700 keV (see fig.61).

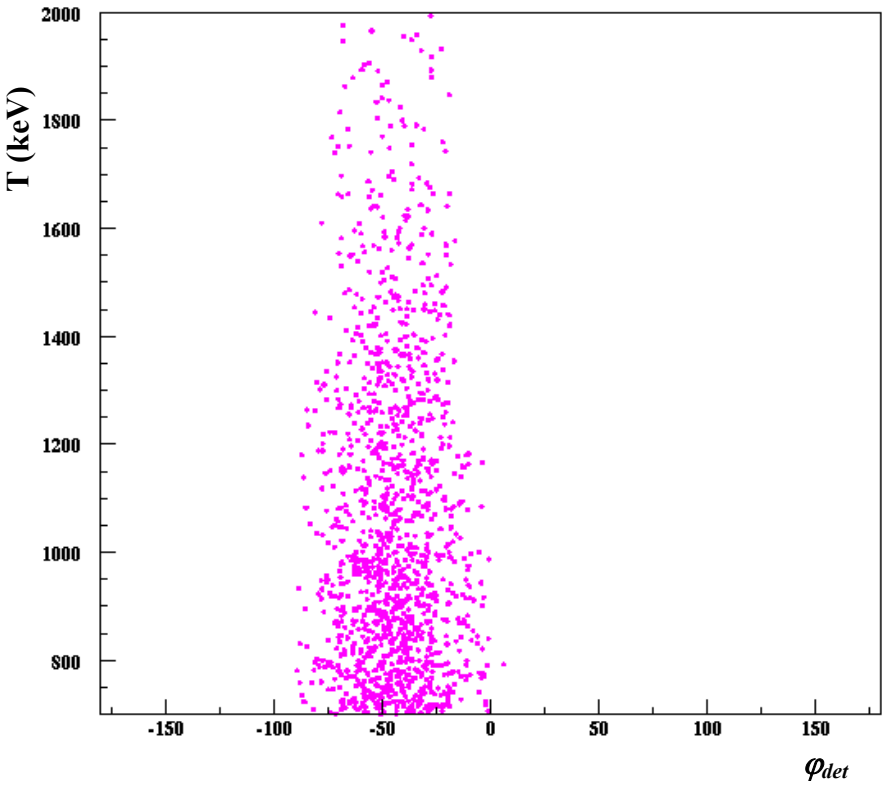

Fig.61. φ_{det} as a function of energy (T) for forward electrons (from neutrino electron scattering)

III.4.4.2. Energy distribution of forward and normalized background electrons

The normalized background is defined as

$$Electrons_{Normal.background} = \frac{Electrons_{Source} + Electrons_{Antisource} + Electrons_{Backward}}{3} \qquad (39)$$

The number of the normalized background electrons in each energy interval (from 700 keV to 2000 keV) is obtained with the help of eq.39.

The errors of normalized background electrons $\sigma^2_{normbackground}$ are calculated according to

$$\sigma^2_{normbackground} = \frac{\sigma^2_{source} + \sigma^2_{antisource} + \sigma^2_{backward}}{9} \qquad (40)$$

The numbers of normalized background electrons are calculated from (40) as

$$(431_{source} + 387_{antisource} + 336_{backward}) / 3 = 385_{normal\ background}$$

The energy distributions of forward (455) and normalized background (385) electrons are given in fig.62.

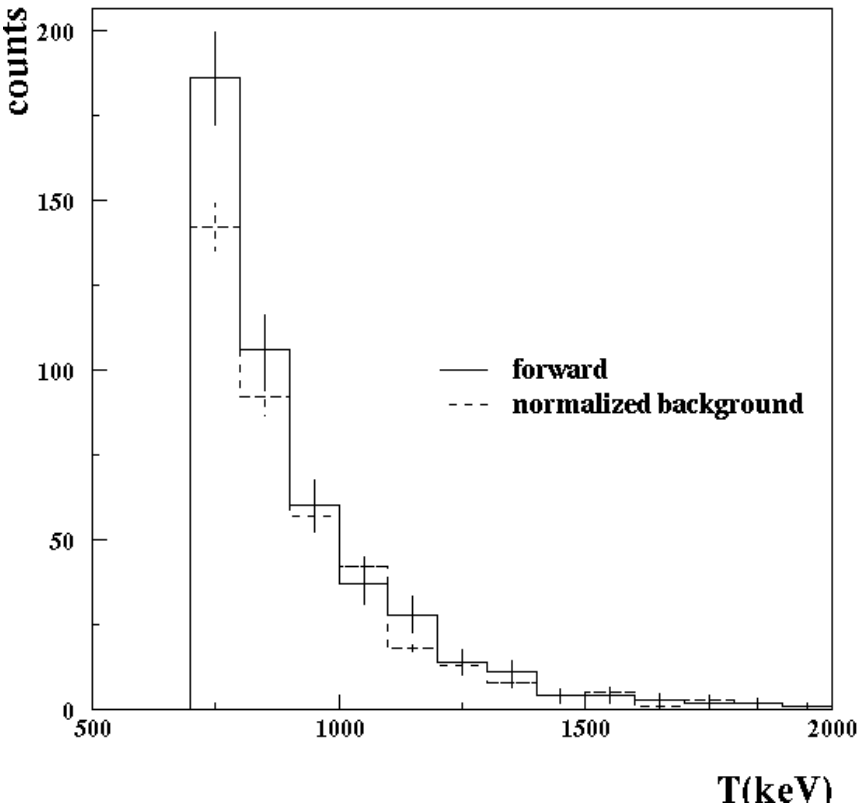

Fig.62. The energy distributions of forward and normalized background electrons.

III.4.4.3. Energy distribution of forward minus normalized background electrons

The measured signal is calculated by

$$Electrons_{Signal} = Electrons_{Forward} - Electrons_{Normal.background} \qquad (41)$$

In (41) $Electrons_{Forward}$ are the forward electrons and $Electrons_{Normbackground}$ are normalized background electrons.

The errors on the signal σ^2_{signal} are calculated by

$$\sigma^2_{signal} = \sigma^2_{normbackground} + \sigma^2_{forward} \qquad (42)$$

The energy distribution of the forward (455) minus normalization background (385) electrons is shown in fig.63.

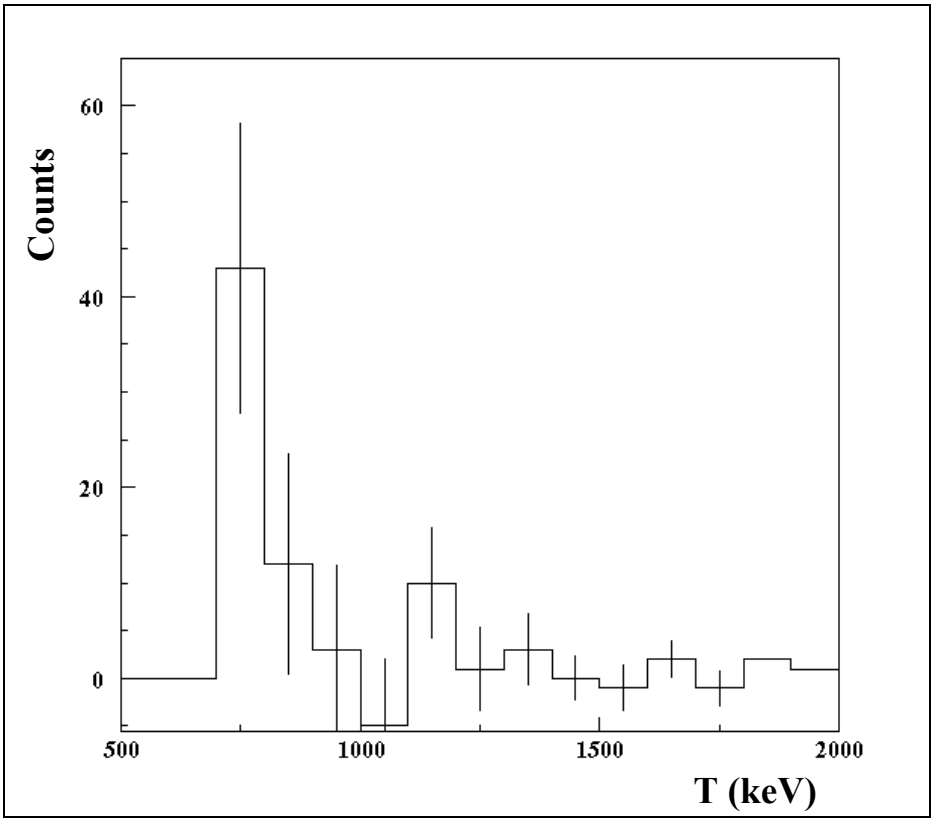

Fig.63. The energy distribution of forward minus normalized background electrons.

The total forward minus normalized background rate is 70 for 66.6 days reactor on above 700 keV, which gives 1.05 ± 0.36 cpd.

The expected rate (Cf. III.2.3) is found to be 68.2 for 66.6 days, which gives 1.02 ± 0.12 cpd.

Please note that this time the agreement between the measured (70) and expected (68.2) rate is excellent.

III.4.4.4. χ^2 analysis

We compare the measured signal with the predicted one from weak interactions ($\mu = 0$) by using the expression (38) for χ^2 as we did before. The measured signal (forward minus normalized background electrons), together with the expected one from the weak interactions ($\mu = 0$), is given in fig. 64.

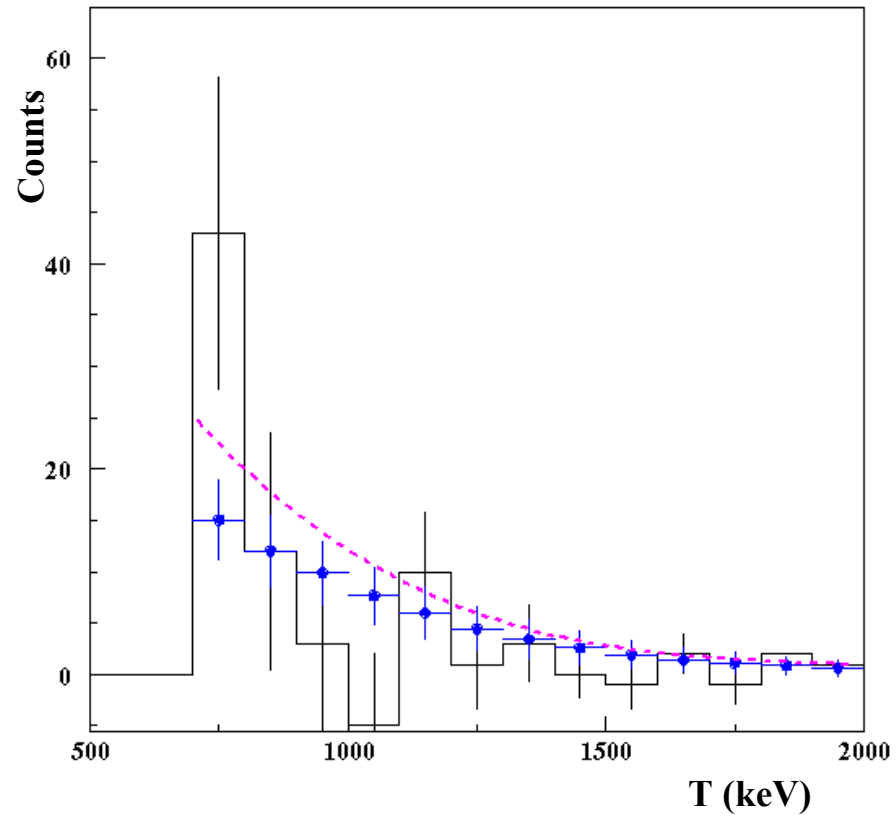

Fig.64. Energy distribution of forward minus normalized background electrons (solid line) compared to the expected rate from weak interactions (circles). The expected rate from weak plus electromagnetic interactions ($\mu = 0.95 \times 10^{-10}\ \mu_B$) is given with dashed line.

Although the expected rate per day by assuming zero magnetic moment (1.02 ± 0.12 cpd) is in a perfect agreement with the measured rate (1.05 ± 0.36 cpd) we still have an accumulation of events in the first channel from 700 keV to 800 keV (see fig. 64). The explanation of this phenomenon could be searched in the energy dependence of the gain (in 3-bar data calibration, the gain is supposed to be constant, while in reality it depends on energy). Some fluctuations of the gain itself, which are not taken into account in the calibration (mainly done by cosmic muons), could also affect the final energy distribution of the events.

III.4.4.4.1. 700 keV analysis

The result of χ^2 (μ^2) for electron energy above 700 keV is presented in Fig. 65.

The minimum of χ^2 is found to be 10. Although the best fit is on high side χ^2/d.o.f. = 10/7 = 1.4 (resulting from the difference between expected and measured spectra in the first channel), the adjustment of the two spectra is satisfactory now.

The squared magnetic moment μ^2 in the minimum of χ^2, μ^2 (χ^2_{min}) is $-0.64 \times 10^{-20}\ \mu^2_B$.

Furthermore we find in the 68 % confidence interval $\mu^2 = -0.64 \pm 0.74 \times 10^{-20}\ \mu^2_B$ and in the 90 % confidence interval $\mu^2 = -0.64 \pm 1.24 \times 10^{-20}\ \mu^2_B$ (Fig.65).

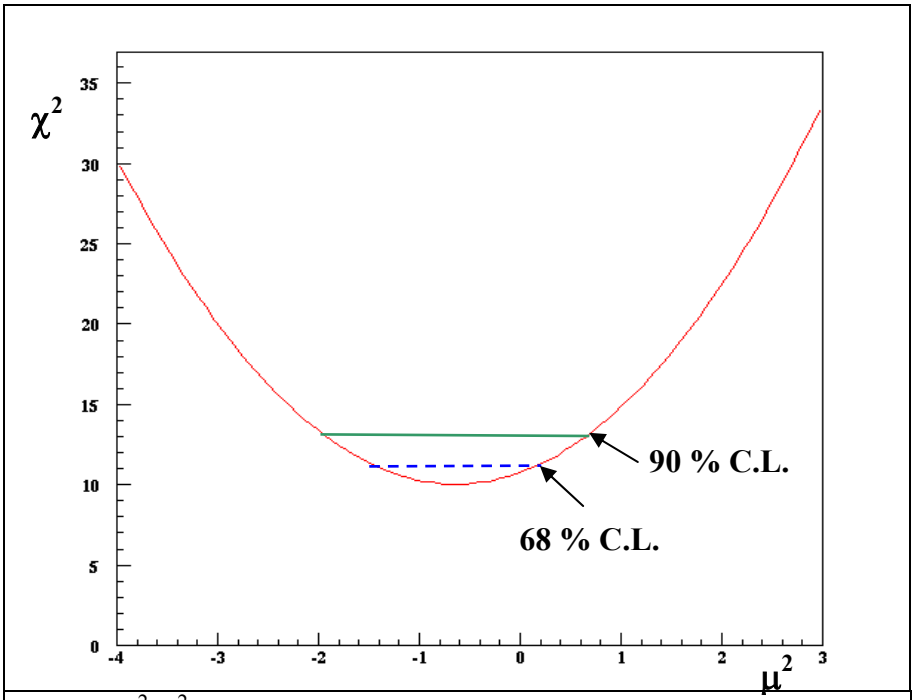

Fig.65. $\chi^2(\mu^2)$. 90 % C.L. (line) and 68 % C.L. (dash line) regions are shown.

We renormalize the above results to the physical region ($\mu^2 \geq 0$) and find next limits:

$\mu < 0.71 \times 10^{-10}\ \mu_B$ at 68 % C. L. and $\mu < 0.95 \times 10^{-10}\ \mu_B$ at 90 % C. L.

The energy distribution of expected rate from weak plus electromagnetic interactions ($\mu = 0.95 \times 10^{-10}\ \mu_B$) is shown in fig.64.

III.4.4.5. Comparison of the result of MUNU experiment with the results from the other experiments

The results of MUNU experiment $\mu < 1.0\ (0.8) \times 10^{-10}\ \mu_B$ at 90 (68) % C. L. [41] improve the existing experimental limits on the neutrino magnetic moments.

Firstly the most recent limit from a direct measurement, has been obtained from the TEXONO collaboration [42] by using an Ultra Low Background High Purity Germanium Detector installed near the Kuo-Sheng reactor in Taiwan. The energy threshold is 12 keV.

The reactor-on minus reactor-off was found to be identical and from that the limit $\mu_\nu < 1.3 \times 10^{-10} \mu_B$ (90 % C.L.) was reported.

Secondly, the limits that have been derived from the indirect measurements,obtained by the Super - Kamiokande experiments, which depend however on underlying oscillation neutrino scenario. The Super- Kamiokande (SK) experiment is a water Cherenkov detector with a fiducial volume of 22.5 kton. SK detects solar neutrinos via the elastic scattering of solar neutrinos off electrons in the water. This experiment has measured the electron recoil spectrum of solar ^{8}B neutrinos.

From the shape of the spectrum the limit $\mu_\nu^{sol} < 1.5 \times 10^{-10} \mu_B$ (90 % C.L.) was derived [8] in 1999.

More recently in 2004, a limit of $\mu_\nu^{sol} < 3.6 \times 10^{-10} \mu_B$ (90 % C.L.) was reported from an analysis of 1496 live days by fitting the day/night spectra.[43]. In addition, in the same work, a limit of $\mu_\nu^{sol} < 1.1 \times 10^{-10} \mu_B$ (90 % C.L.) was obtained by combining the results from all solar neutrino and KamLAND experiments constraining the oscillation region.

III.4.4.6. Summary

We have shown here an alternative way to estimate the background and extract the signal by using the forward-normalized background analysis.

By using this method we achieve:

- **good agreement between the measured (1.02 ± 0.12 cpd) and expected rate from the weak interactions (1.05 ± 0.36 cpd)**

- **above 700 keV the obtained limit of $\mu < 0.95 \times 10^{-10} \mu_B$ at 90 % C. L. is better that the limit obtained with the forward backward analysis in the same energy region ($\mu < 1.4 \times 10^{-10} \mu_B$)**

- **the limit of $\mu < 0.95 \times 10^{-10} \mu_B$ at 90 % C. L. which is found above 700 keV is in perfect agreement with the limit of $\mu < 1.0 \times 10^{-10} \mu_B$ at 90 % C. L. which is found above 900 keV by the forward backward analysis.**

CHAPTER IV

1 bar data analysis

IV.1. Energy calibration of the Time Projection Chamber

The energy calibration of the detector is done with γ-sources and cosmic muons.

Here is described the procedure for the energy calibration of the Time Projection Chamber (TPC), which is developed by the author. This procedure is used for the energy calibration of the detector in 1-bar period of data taking.

IV.1.1. Energy calibration of the TPC with γ sources

The two γ sources which are used for calibration of the TPC at 1 bar are ^{54}Mn and ^{137}Cs with the energy of the incident gammas (E_γ), respectively, 834 keV and 662 keV.

A gamma undergoes at least one elastic scattering with the electrons in the TPC, before leaving the detector. The result in the TPC is a continuous Compton electron spectrum.

The energy of the Compton edge (E_e) [44] is

$$E_e = E_\gamma - E_c \tag{43}$$

In (43) E_c is the energy of the gap between E_γ and E_e and is calculated by

$$E_C \equiv h\nu - E_{e^-}\Big|_{\theta=\pi} = \frac{h\nu}{1+\frac{2h\nu}{m_0c^2}} \tag{44}$$

The calculated energy of the Compton edge, E_e, is found to be 638 keV for ^{54}Mn and 478 keV for ^{137}Cs.

A program based on the code GEANT 3 [45] was used for Monte Carlo simulations.

Why do we have to use Monte Carlo simulations for calibrations?

First, the photons from the sources could not be detected directly in the TPC, but only from the Compton scattering with electrons. Second, the full energy peak is not available, but only the Compton edge.

The position of the Compton edge for ^{54}Mn is at 640 keV for an ideal detector (see fig.66).

For a real detector, however the Compton edge is smeared out by the resolution. It washed down and shifted to the left (see Fig.67).

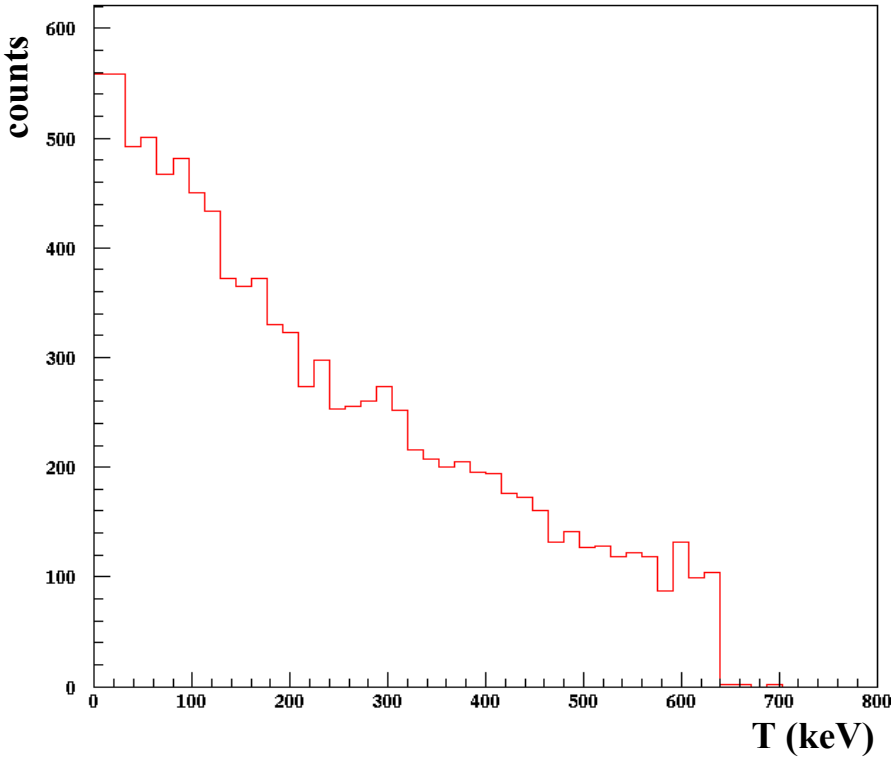

Fig.66. The Compton electron spectrum in the TPC for an ideal detector with zero resolution.

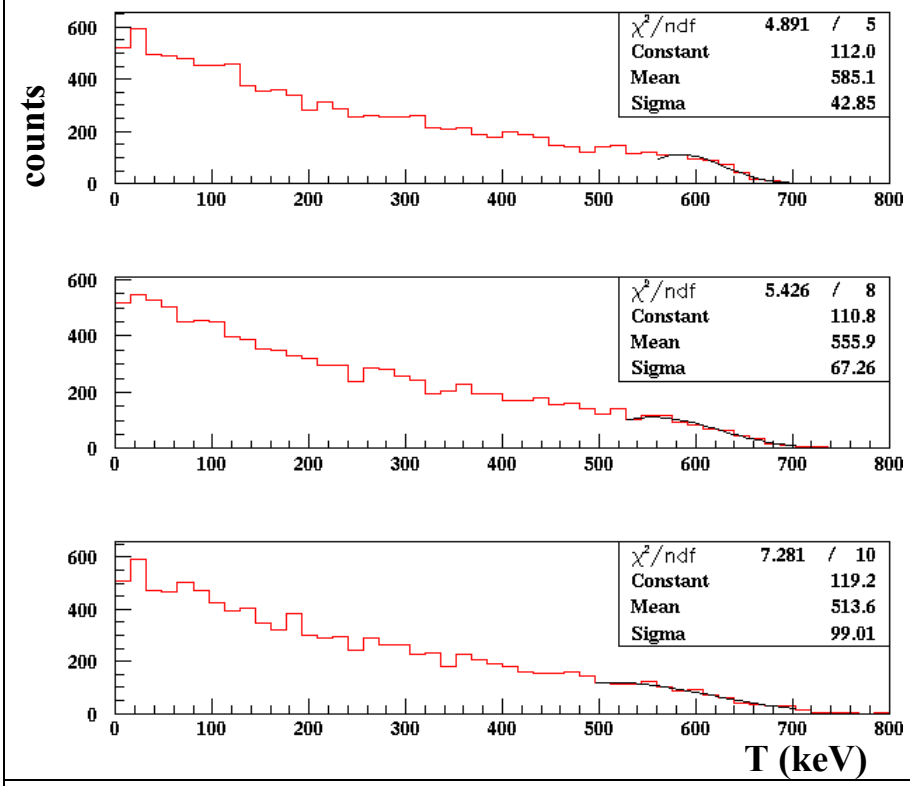

Fig.67. The Compton electron spectrum in the TPC for 3 different resolutions: 2%, 4% and 10%. The position of the Compton edge (obtained with a Gaussian fit) is at 585 keV, 555keV and 513 keV respectively.

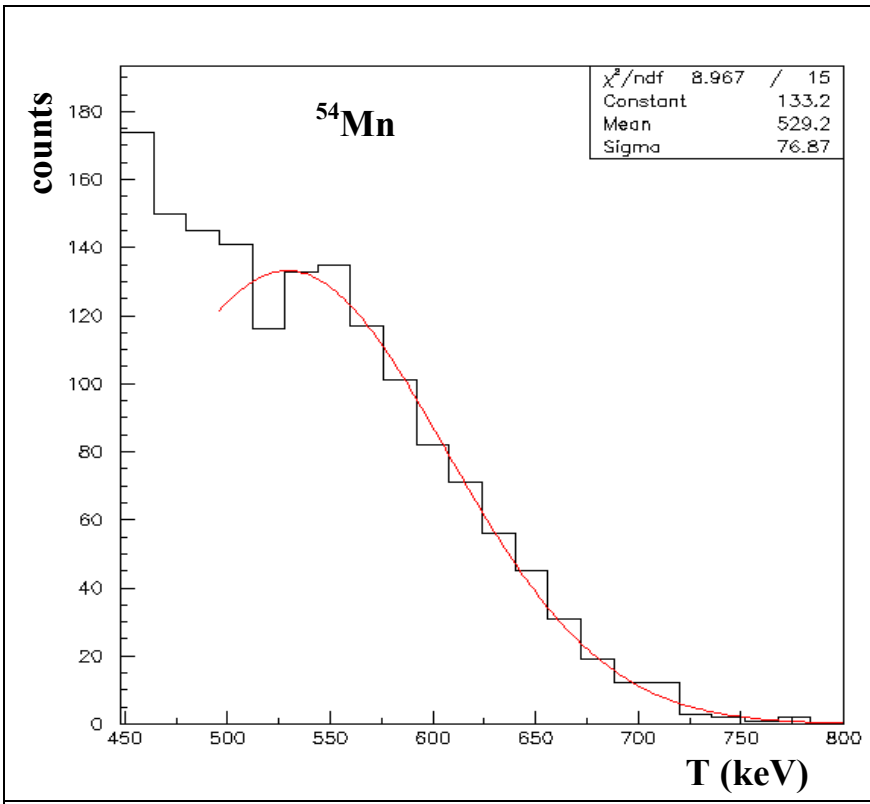

Fig.68. A Gaussian fit of the Compton edge is shown. The sigma and the mean of the fit are given in the small window.

The anode signal (*anodsm)*), which is a combination of the Compton electron spectrum plus the noise from various sources of background is used for energy calibration

We are only interested in the end of the spectrum, which we can assume as a pure signal from the source (without the background). The signal is plotted as a histogram and is fitted in the region of the Compton edge with a Gaussian function as it is shown in Fig.68 for ^{54}Mn.

The simulated and the measured anode signals, together with the Gaussian fits of the end of the spectra, are shown for ^{54}Mn in fig.69.

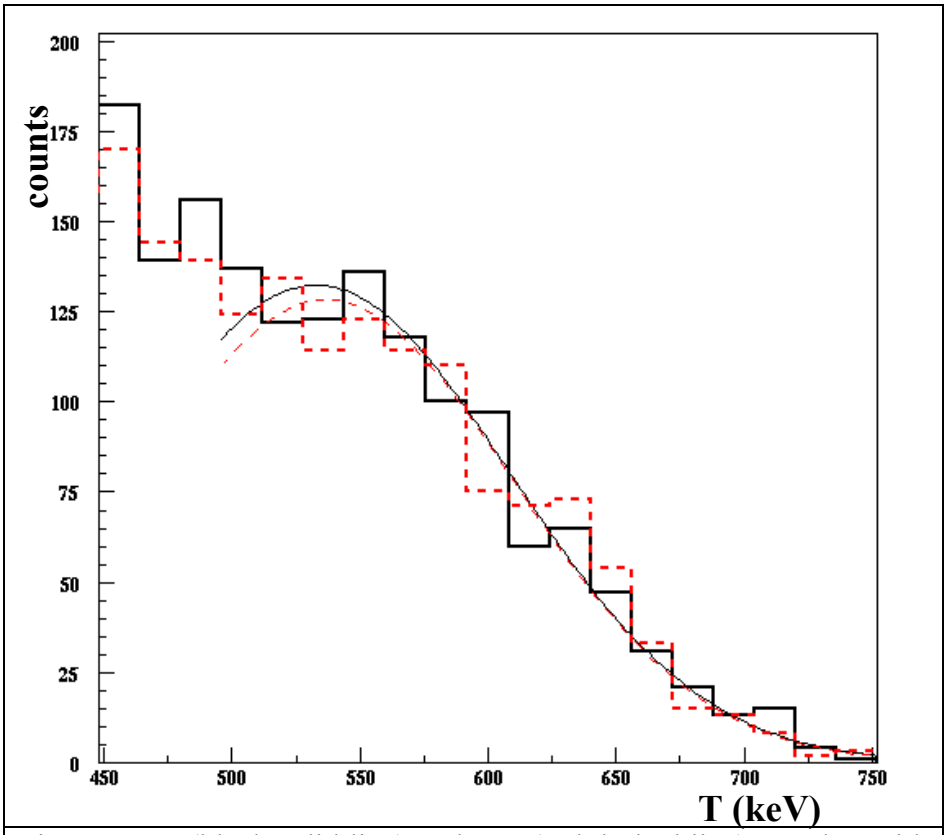

Fig.69. Data (black solid line) and MC (red dashed line) together with the Gaussian fits of the Compton edge for ^{54}Mn

A χ^2 method is used for comparison between the data and simulations.

The χ^2 is given by

$$\chi^2(C,R) = \sum_{i=1}^{n} \frac{\left(x_{i\exp} - x_{iMC}(C,R) \right)^2}{\left(\sigma_1(\exp) + \sigma_2(MC) \right)^2} \qquad (45)$$

Where C is the coefficient of calibration, R is the resolution of the detector, σ_1 and σ_2 are the statistical errors on experimental (x_{iexp}) and simulated points (x_{iMC}), and n is the number of channels.

IV.1.1.1. Calibration with ^{54}Mn

We are interested (in this example) in the region between 530 keV and 768 keV. This region is divided in 14 channels, 17 keV per channel.

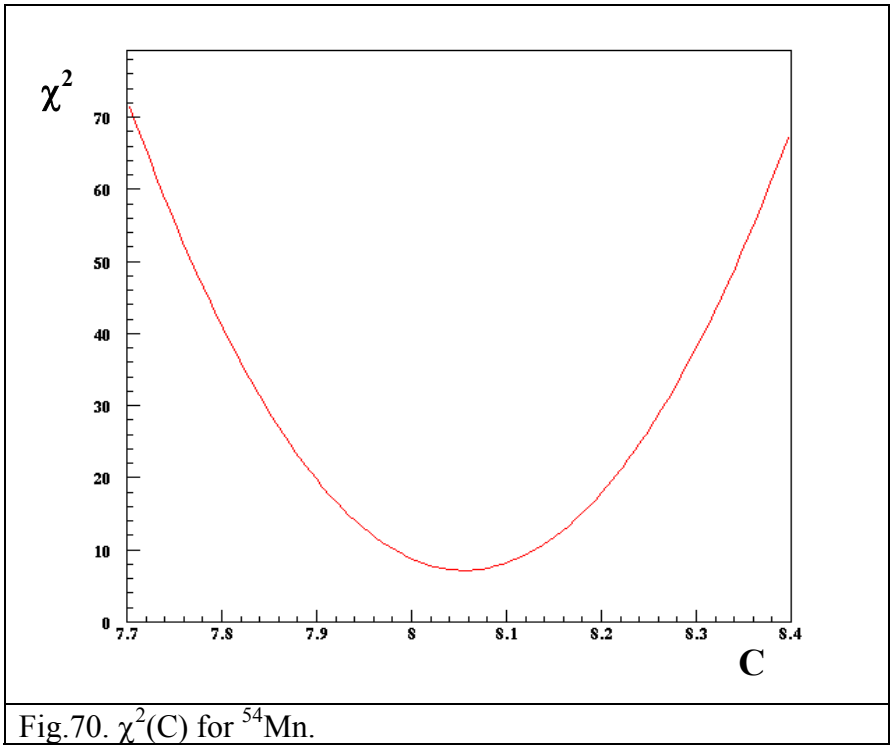

Fig.70. χ^2(C) for ^{54}Mn.

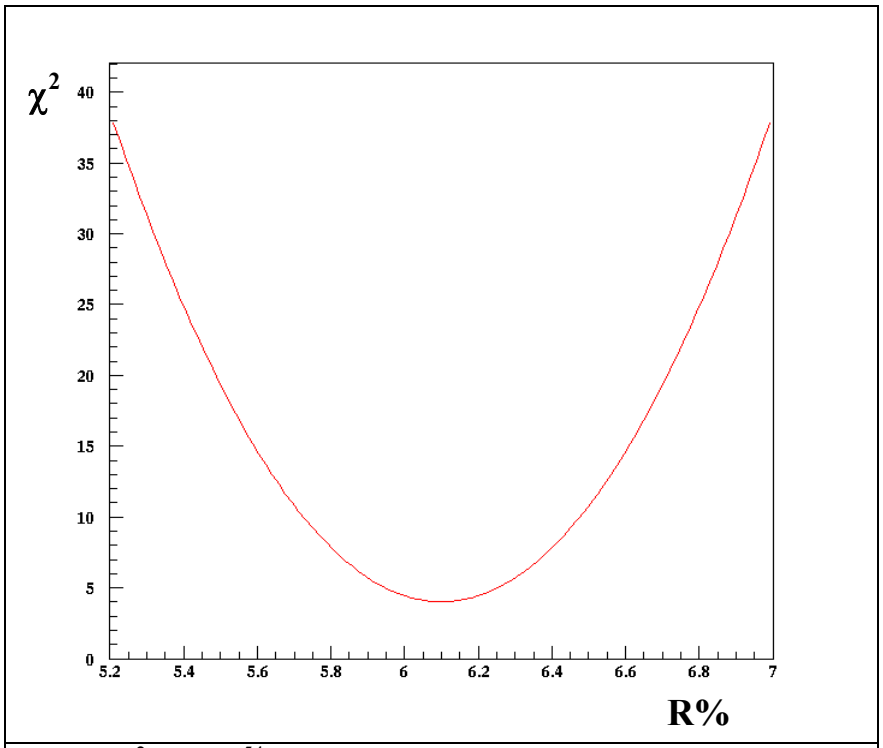

Fig.71. χ^2(R) for ^{54}Mn.

We vary the following two free parameters: the coefficient of calibration (C) and the detector resolution (R). The degree of freedom is 12.

First, we vary C for R = 6.1 % in order to find the minimum of χ^2. The result for χ^2 *(C)* is presented in Fig.70. In the minimum of χ^2 (7.27), C is 8.04. In 90 % confidence interval we found $C = 8.04 \pm 0.06$.

Second, we vary R for C = 8.04. The result for χ^2 *(R)* is presented in Fig.71. In the minimum of χ^2 (4.3), R is 6.1%. In 90 % confidence interval we fond $R = 6.1 \pm 0.25$ %.

(χ^2/d.o.f) = 0.6 for the coefficient C and (χ^2/d.o.f) = 0.3 for the resolution R.

The final result from the calibration with ^{54}Mn is presented in Fig.72.

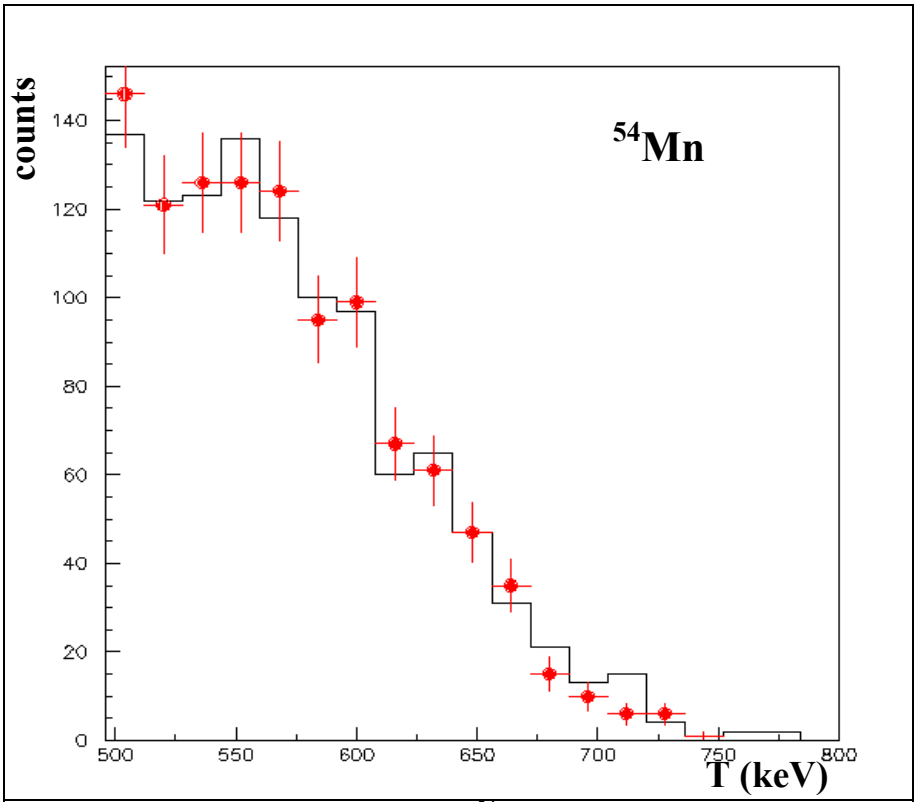

Fig.72. A Compton spectrum of ^{54}Mn in the TPC (black line) compared with MC (red circles)

IV.1.1.2. Calibration with ^{137}Cs

The region between 420 keV and 560 keV is divided in 14 channels, 10 keV per channel. We vary C and R; hence the degree of freedom is 12.

First, we vary C for R = 6.8 %. The result for χ^2 *(C)* is presented in Fig.73. The calibration coefficient C in the minimum of χ^2 (4.8) is 6.98. In 90 % confidence interval we obtained $C = 6.98 \pm 0.04$.

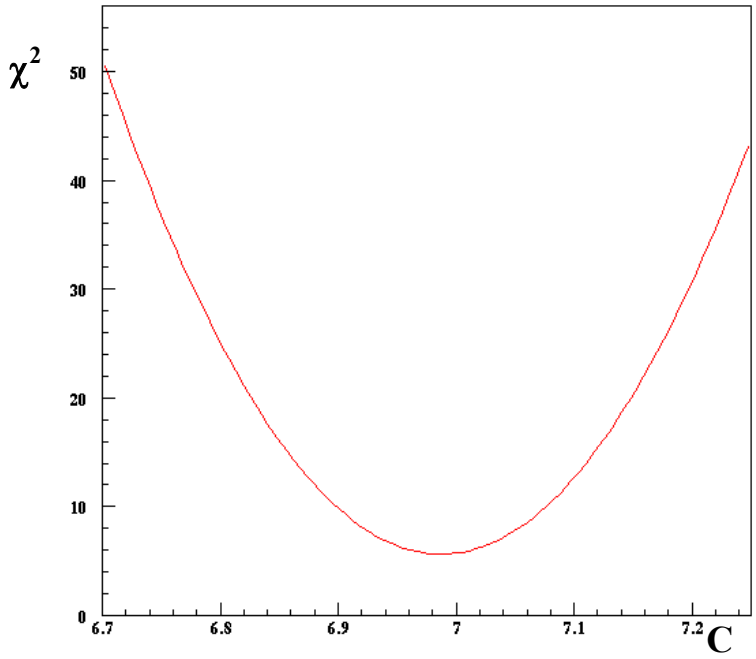

Fig.73. χ^2(C) for ^{137}Cs.

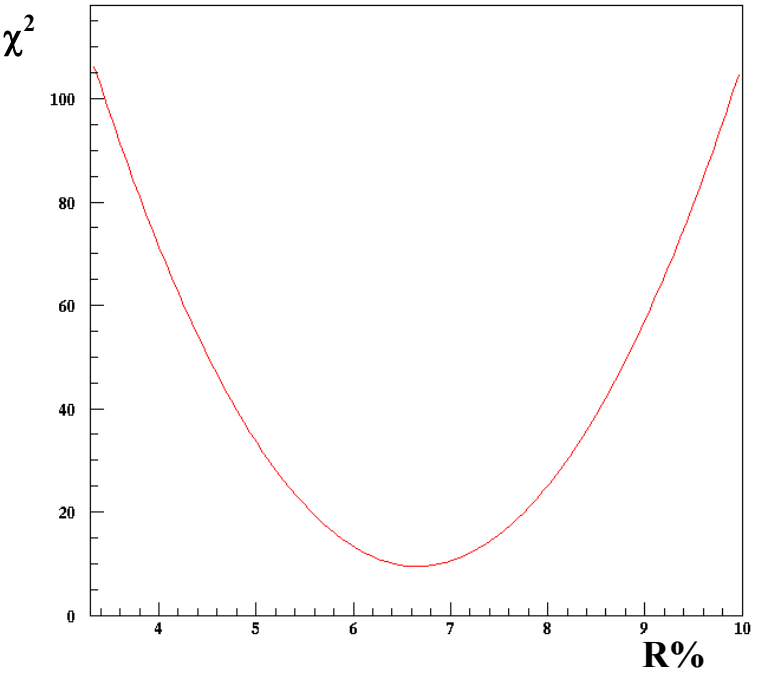

Fig.74. χ^2(R) for ^{137}Cs.

Secondly, we vary R for C = 6.98. The result for χ^2 *(R)* is presented in Fig.74. The resolution R in the minimum of χ^2 (4.82) is 6.8 %. In 90 % confidence interval is R = 6.8 ± 0.25 %.

(χ_{min}^2/d.o.f) = 0.4 for both the coefficient C and the resolution R.

The final result from the calibration with ^{137}Cs is presented in Fig.75.

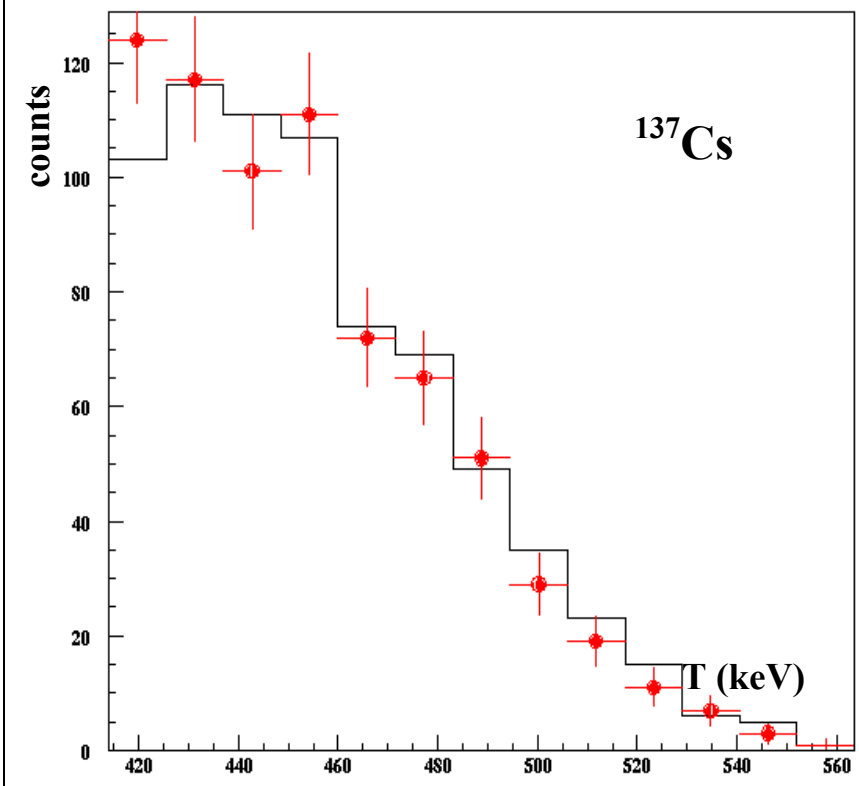

Fig.75. A Compton spectrum of ^{137}Cs in the TPC (black line) compared with MC (red circles)

IV.1.2. Energy dependence of the calibration coefficient

To study the calibration coefficient as a function of energy we take as an example the energy calibrations that are done with two sources (^{54}Mn and ^{137} C) on the same day.

In the table below are given the energies of the Compton edge, calibration coefficients, and simulated anode signals (*anodsm)*.

Source	**^{137}Cs**	**^{54}Mn**
Energy of the Compton edge (keV)	478	638
Calibration coefficient (C)	6.96	7.36
Anodsm (arb. units)	3327	4696

The results from the table for the calibration coefficient (*C*) as a function of the true energy (*T*) are presented in Fig.76. One can see that the coefficient of calibration varies with energy.

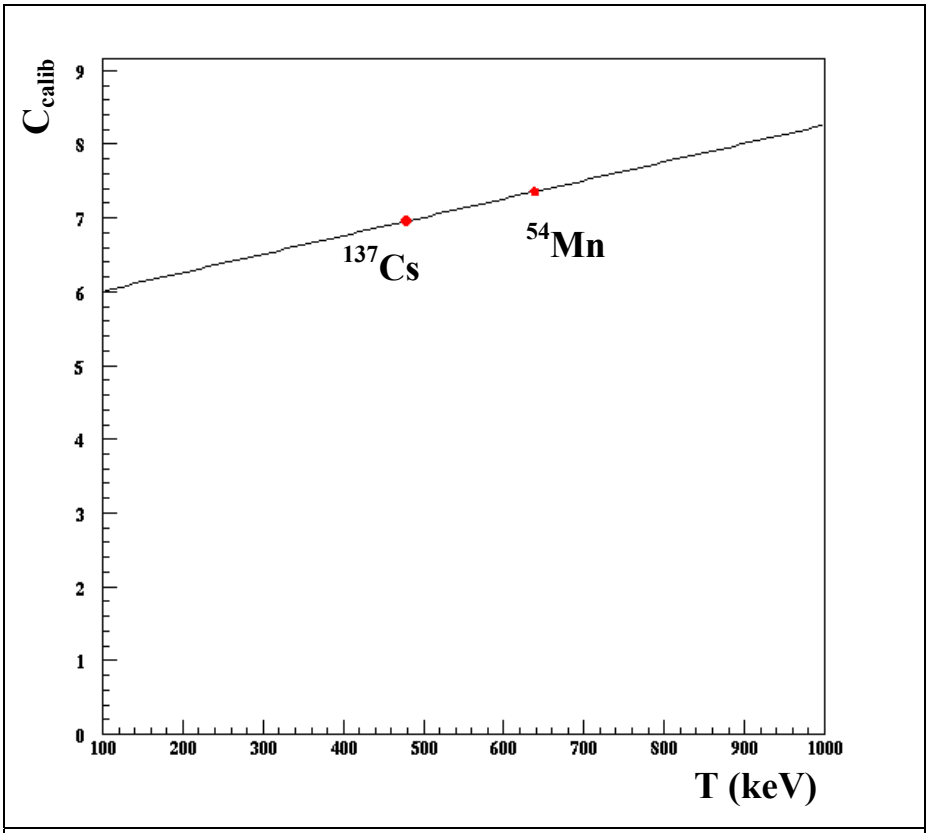

Fig.76. Coefficient of calibration (C_{CALIB}) depends on energy

IV.1.3. Energy dependence of the gain

To study the gain of the detector at 1-bar we plot the simulated anode signal (*anodsm*) as a function of the energy (*T*) (fig.77) for ^{54}Mn and ^{137}Cs sources.

In fig.77 the dashed line represents an ideal detector (the gain is constant and does not change with energy). The line is passing through three points: 0 and the sources. The solid line represents the measurements with sources. The gain of the detector depends on energy and the line is passing through the two sources points.

One possible explanation of the energy dependence of the gain is the influence of the electronic noise. The *anodsm* is a sum of the Compton electrons signal plus the electronic noise.

The *anodsm* is connected with the energy *T* by the following expression for the real case (see solid line in fig.77):

$$anodsm = 8.556\,T - 762.8$$

This equation gives for the detector an offset of 89 keV for the 1-bar period.

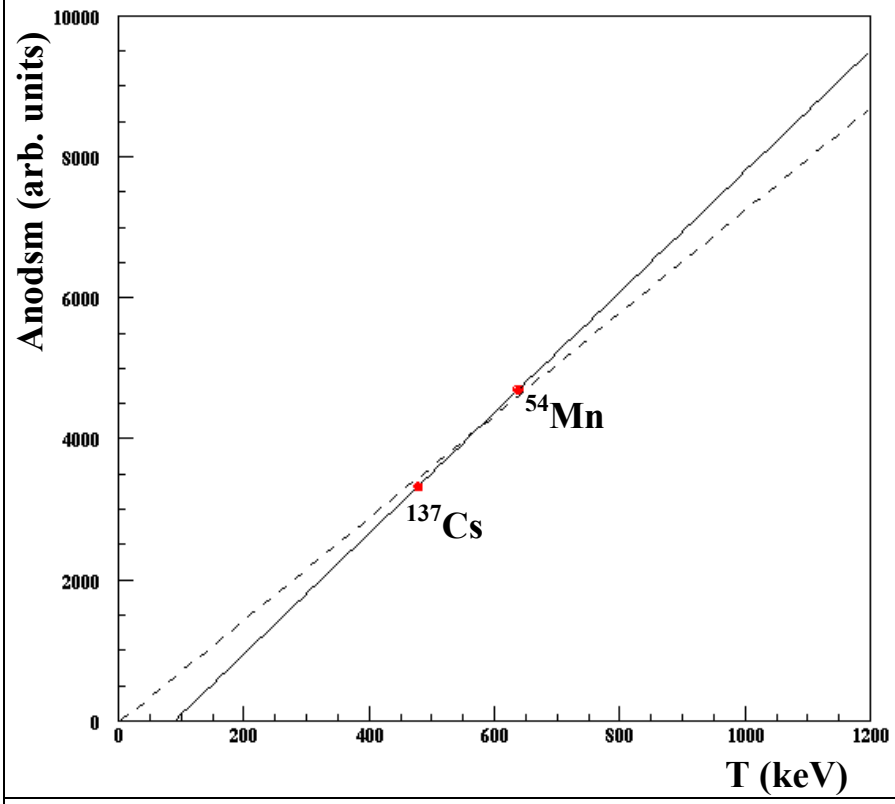

Fig.77. The gain for a perfect detector (dashed line) and the gain obtained experimentally with two sources (solid line).

The detector gain also showed a similar energy dependence during the 3-bar period and the offset was found to be 75 keV [36].

The incomplete subtraction of the background plus electronic noise, as well as the increase of the electronic noise itself, are possible explanations for the different offset during the 1-bar period.

IV.1.4 Energy resolution of the TPC for the 1-bar period

The energy resolution is given by

$$R = \frac{\sigma(E)}{E}. \tag{46}$$

In (46), $\sigma\ (E)$ and E are the sigma and energy mean of the Gaussian distribition, respectively.

We find the energy resolution of the TPC with the help of the energy resolutions of ^{54}Mn and ^{137}Cs sources. The energy resolution at 640 keV (^{54}Mn) is found to be 6.1 % (see fig.71) and the energy resolution at 478 keV (Cs source) is found to be 6.8 % (see fig.74)

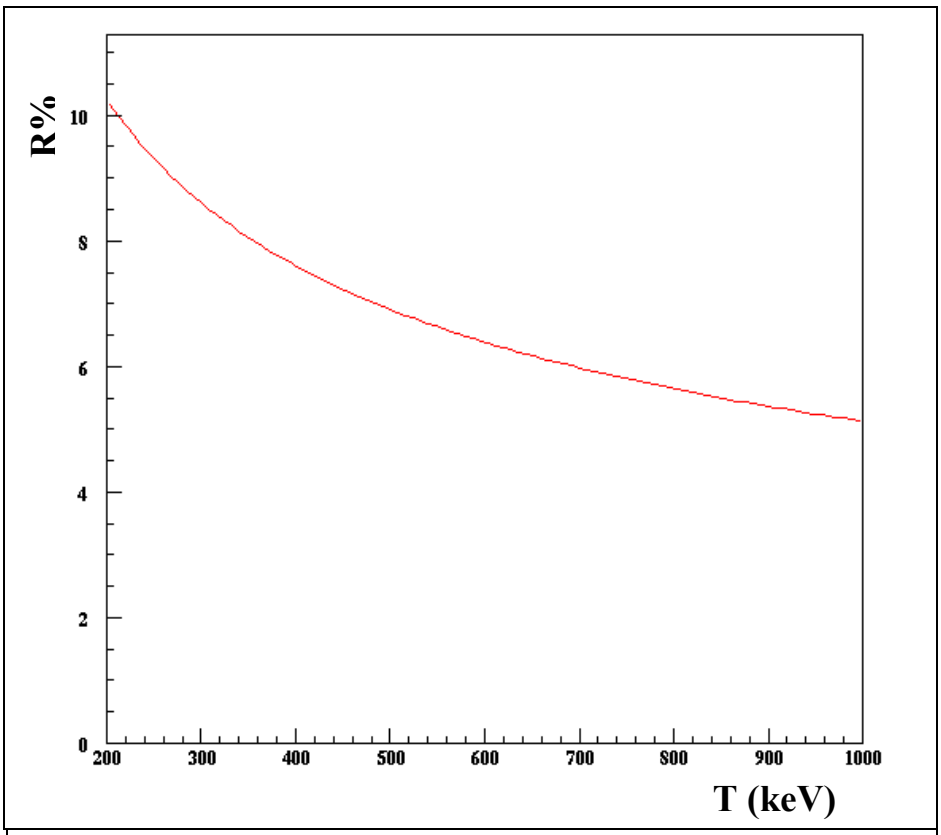

Fig.78. The energy resolution of 1-bar period as a function of energy.

We combined the above results from both sources, 6.1 % (at 640 keV) and at 6.8 % (at 478 keV) respectively, and deduced an empirical law for the resolution at 1bar, that is given by (47) and presented in Fig.78.

$$R = \frac{\sigma(E)}{E} = \frac{E^{0.57}}{E} \tag{47}$$

We can see from Fig.78 that the energy resolution at 1-bar at 200 keV is 10%, at 400 keV it is 7.6 %, at 600 keV it is 6.4 %, at 1 MeV it is 5.1 % and so on.

IV.1.5. Comparison between the energy resolutions of the TPC for 1-bar and 3-bar periods

The energy resolution of the detector for 3 bar [36] is given by the semi-empirical low (48).

$$R = \frac{\sigma(E)}{E} = \frac{\sigma_0 \left(\frac{E}{E_0} \right)^{0.31}}{E} \tag{48}$$

In (48) σ_0 = 80 keV and E_0 = 1 MeV.

T (keV)	R % (3-bar)	R%(1bar)
200	24	10
400	15	7.6
600	11.4	6.4
1000	8	5

The energy resolutions for 1-bar and 3-bar are given in the table above. One can see that the resolution at 1 bar is about 1.7 – 2 times better than at 3-bar.

The energy resolution of the TPC filled with CF4 gas depends on one hand on the electrical property of the gas itself (ionisation of the gas, attachment and multiplication) and on the other hand on the quality of the detector (homogeneity of the gain on the anode plane and charge attenuation). It is difficult however to evaluate all the parameters and their consequences. For 3bar pressure exist calculations and simulations of the expected energy resolution [36, 46], which however differ from the experimental ones (48).

In our opinion the main parameters that are responsible for the better energy resolution at 1-bar than at 3-bar are:

the effective attachment of CF4, which is smaller at 1-bar (85 % - 87 %) than at 3-bar (95 % -97 %) [34, 36, 47].

the number of the surviving electrons after the attachment in CF4 is bigger at 1-bar (13 % - 15 %) than at 3-bar (3 % - 5 %).

t**he density of the gas:** at 1-bar it is 3 times smaller than at 3-bar, hence there is less multiple scattering at 1-bar

t**he length of the tracks**: at 1-bar 1.5 times larger than at 3-bar

the gain of the detector: at 1-bar amplification is 1.5 times larger than at 3-bar

Some of the above parameters, such as the attachment and the gain degrade the resolution, while others, such as the length of the tracks and the number of the surviving electrons, improve it.

The final numbers however are difficult to evaluate simply by direct inspection of the above parameters without simulations (which are not covered by the subject of the presented work).

IV.2. Energy calibration of the TPC with cosmic muons

The MUNU detector is situated at a depth corresponding to a shielding of 20 meter water equivalent and is exposed to a constant flux of cosmic muons, which is equal to 32 m^{-2} s^{-1}.

The Anti-Compton detector is especially designed to veto gamma particles and cosmic muons. A cosmic muon, coming outside the detector has to cross the liquid scintillator with a mean energy loss of about 1.8 MeV cm^{-1}. It produces a large prompt signal in the phototubes (fig.79.bottom), which could be used as a trigger to select, or to veto muon events. The pictures of a cosmic muon at 1 bar pressure, together with the signals that are produces in the anode and photomultipliers, are shown in Fig.79.

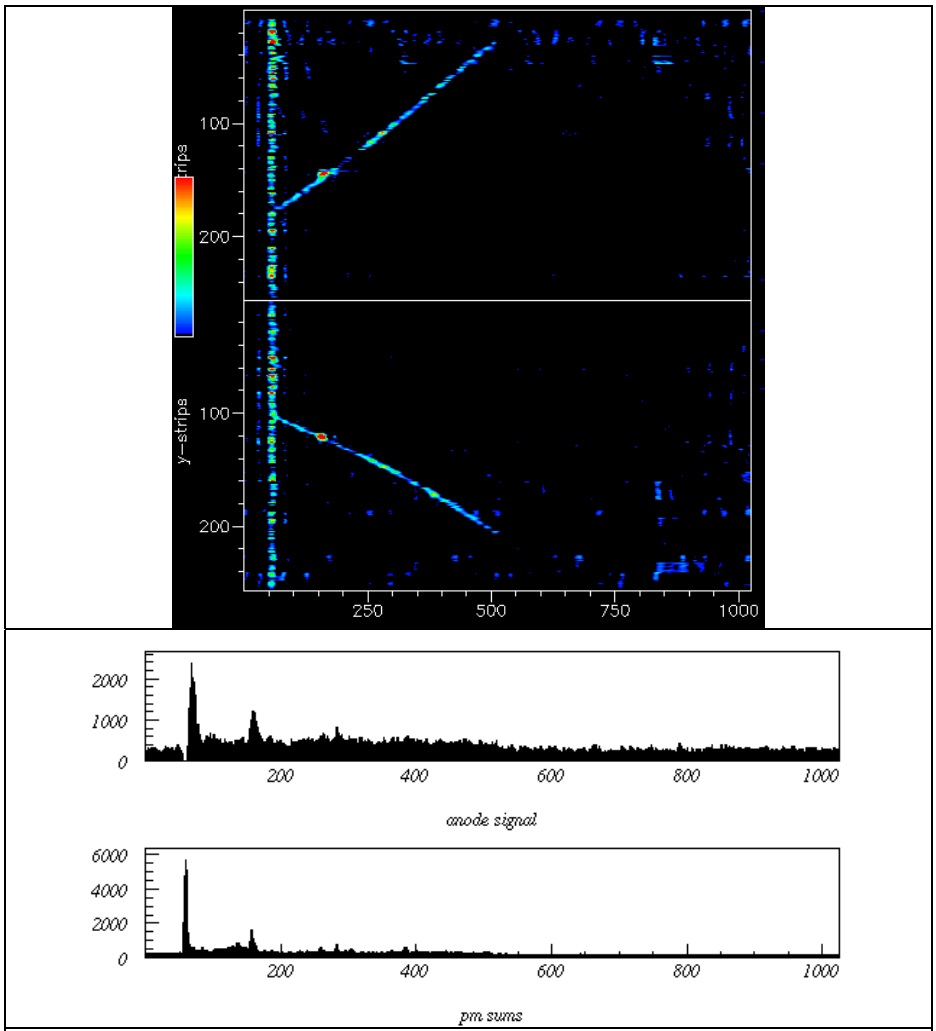

Fig.79. A cosmic muon in TPC at 1-bar pressure. *xz* and *yz* projections of the track (top) are shown together with anode signal (middle) and pm sums (bottom).

The cosmic muons have minimum specific ionisation in the detector and thus are used for the energy calibration.

The muons deposited a constant mean energy loss per cm in the gas: for 3-bar pressure of CF4 19.7 keVcm^{-1} and for 1 bar pressure of CF4, 6.4 keVcm^{-1} (this is an estimate from scanning of simulated muons).

The calibration with muons is used for every day monitoring of the gain. This has advantage with respect to the calibration with sources, because it takes less time and does not result in a loss of total live time of the experiment.

Here we describe the procedure for an energy calibration with muons based on the visual scanning procedure.

We take as an example one file of cosmic muons at 3-bar pressure.

1. The whole length in the TPC, *lentra,* is obtained with DISP.

2. $lentra_X = lentra.\ cos\ (\theta_{det})$ (the horizontal projection of the length with respect to the detector) is calculated.

3. The sum $\frac{\sum_n anodsm}{\sum_n lentra_X}$ is calculated, which corresponds to the measured energy loss per cm in the TPC. The sum has a Gaussian distribution as it shown in Fig.80.

$$\frac{\sum_n anodsm}{\sum_n lentra_X} = 266\ arb.units;$$

266 is the measured mean energy loss per cm.

4. The calibration coefficient is calculated.

To obtain the calibration coefficient one has to divide 266 by 19.7 keV/cm (mean energy loss per cm in CF4 for 3-bar pressure)

$$Coef.calib = \frac{266 arb.units}{19.7 keV/cm} = 13.5$$

However 13.5 is not the final coefficient of calibration, because in this value is included the pedestal (the sum of the background plus electronic noise).

5. The pedestal is calculated

We have to consider here the influence of the pedestal for every cosmic muon, in contrast to the electrons, where the pedestal is negligible.

During the passage of a cosmic muon through the Anti- Compton detector, one observes at the very beginning a large prompt signal in the PMTs and anode plane (see middle and bottom in fig.79). The amplification of this signal having usually duration of 10 microseconds perturbs the PMTs and anode preamplifiers.

After the perturbation, the preamplifiers of the anode and PM's need a few microseconds to find theirs original tension.

We use the pedestal to correct the *anodsm* after the signal and neglect the influence on the electronic noise. This creates an error on the calculated energy, which has to be evaluated. The monitoring of the pedestal during the 3-bar period shows that it is stable with time within the region of 36 % to 40 % [36].

To estimate the pedestal we compare 13.5 with 8.3 (the calibration coefficient from ^{54}Mn source obtained at the same day).

The pedestal in this example is 38 % ((13.5 -8.3) / 13.5 = 0.38).

6. The final coefficient of calibration is calculated

$$C_{muon} = 13.5 - (38\ \% \times 13.5) = 8.3.$$

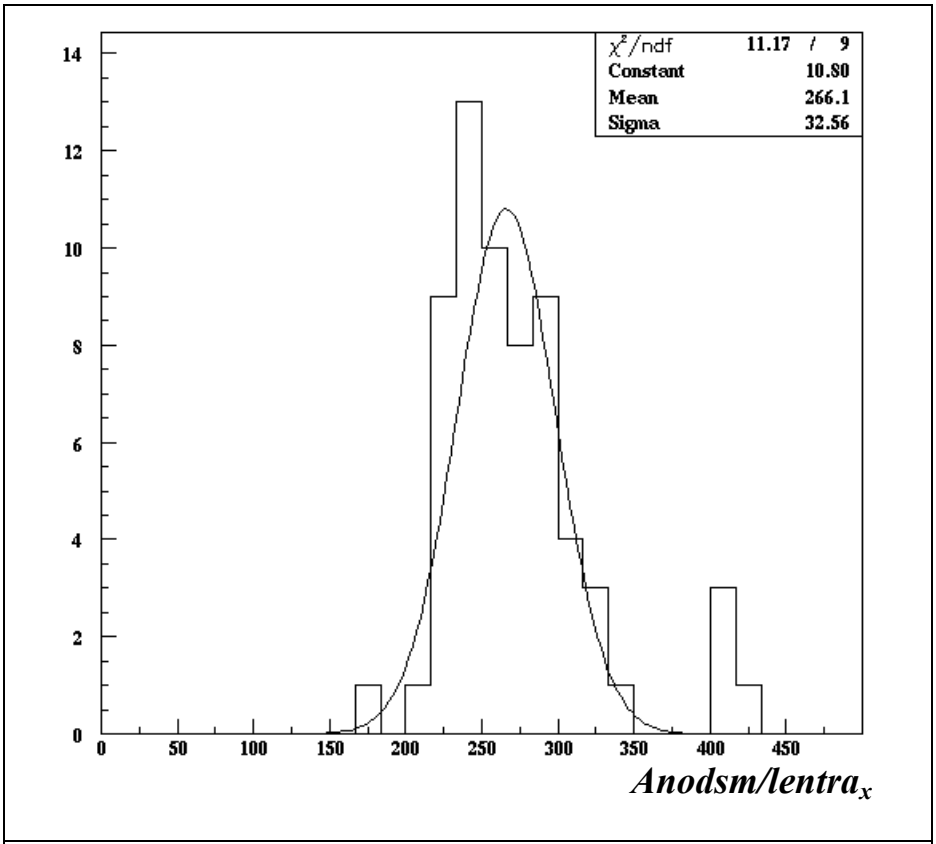

Fig.80. The Gaussian distribution of *anodsm/lentra*$_X$ of the cosmic muons is shown together with the fit (3-bar data).

Now we apply the above procedure for the energy calibration of 1-bar data.

At first we calculate the pedestal for the 1-bar period by using the data from muon and source calibration (^{54}Mn) files, collected at the same day.

The sum $\dfrac{\sum_n anodsm}{\sum_n lentra_X}$ is 113 (arb. units).

The measured mean energy loss per cm in terms of 113 arbitrary units is divided per 6.4 keV/cm (the mean energy loss per cm in CF4 for 1 bar). The result is 17.65 and it has to be corrected with the value for the pedestal at 1 bar.

The coefficient of calibration from the ^{54}Mn source on the same day is 7.34.

The pedestal therefore is 17.65 - 7.34=10.31, which gives a 58.45% pedestal for 1 bar.

Now we use a muon file to calculate the muon calibration coefficient for a period of time when only the muon files are only available for calibration of the data.

The sum $\frac{\sum_n anodsm}{\sum_n lentra_X}$ is 127 (arb. units).

127 is divided per 6.4 keV/cm, which gives 19.8. This value is corrected with the pedestal (58.45 %). We assume that the pedestal at 1-bar period is constant with time (this assumption is in agreement with the observations of the stability of the pedestal at 3-bar during short periods).

This gives 19.8 - (19.8 x 58.45 %) =8.2.

Finally we obtain for the muon calibration coefficient C_{muon} = 8.2.

The ^{54}Mn calibration coefficient at the start of the period is 8.04, which means that the gain is stable in this whole period of 1 bar.

Why is the pedestal for 1 bar (58.45 %) bigger than the one at 3-bar (40%)?

At first the electronics noise at 1-bar is bigger than at 3-bar. The properties of the gas at 1-bar are different. The detector also operates at a lower energy threshold as low as 150 keV.

IV.3. Effective time

The effective time t_{eff} is given by

$$t_{eff} = \frac{t_{runtotaltime}}{coef_{deadtime}} \tag{49}$$

In (49) $t_{runtotaltime}$ is the total time of data taking and $coef_{deadtime}$ is calculated by

$$coef_{deadtime} = \frac{100}{100 - \langle deadtr \rangle} \tag{50}$$

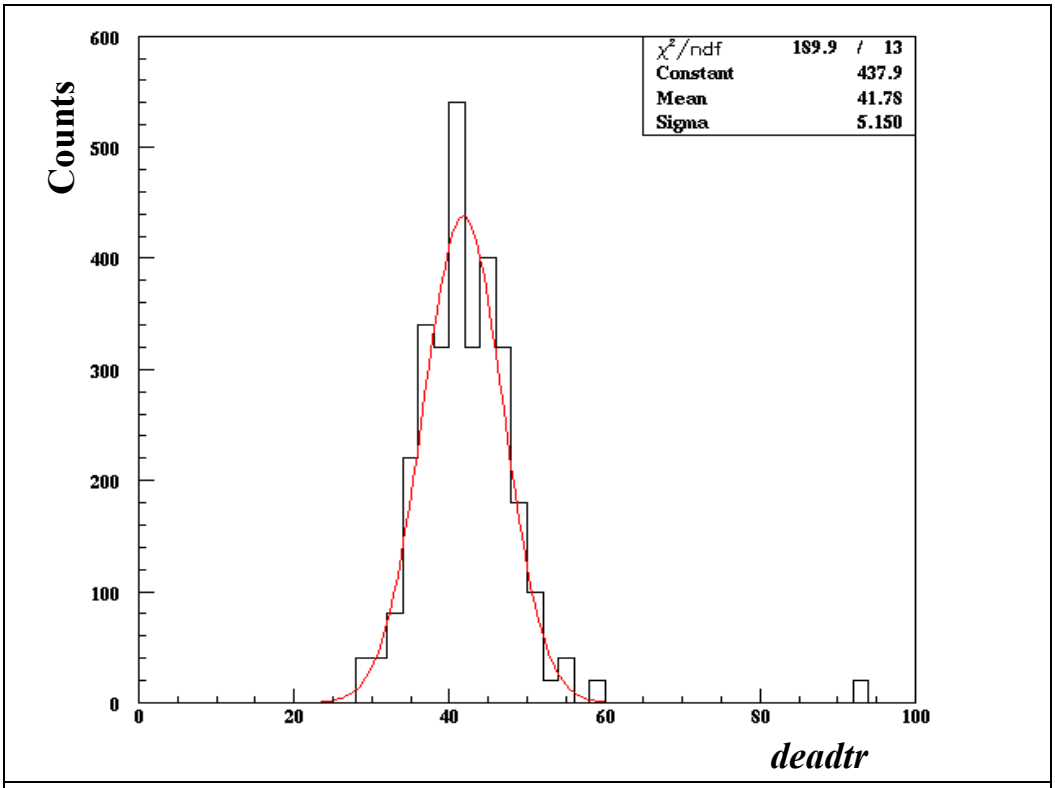

Fig.81. Trigger deadtime distribution (*deadtr*) for one particular file (1-bar data.

In (50) *deadtr* is the trigger deadtime.

The *deadtr* distribution has a Gaussian shape (see fig.81) and $\langle deadtr \rangle$ is the mean of this Gaussian distribtion.

The total deadtime during the 1-bar period is found to be 53 % of the total time, which is larger than at 3-bar, 40 %. The reason for the increase of the total deadtime of the experiment during the 1-bar period is due to the lower detection threshold and to the different containment efficiency of the detector.

The total effective time t_{eff} of 1-bar period is found to be 5.3 live days.

V.4. Examples of events in the TPC at 1-bar of CF4

In fig.82, fig.83, fig.84 and fig.85 are presented examples of electrons of 190 keV, 500 keV, 700keV and 1100 keV respectively.

From these examples one can see that the detector provides a clear signature of electrons from 190 keV to 1100 keV.

The performance of the TPC is good enough to measure the scattering angle and the energy of the electrons down to 190 keV.

Examples of the background events such as cosmic muon and electromagnetic showers (e^+e^- pairs) are given in fig. 86 and fig.87 respectively.

Electrons

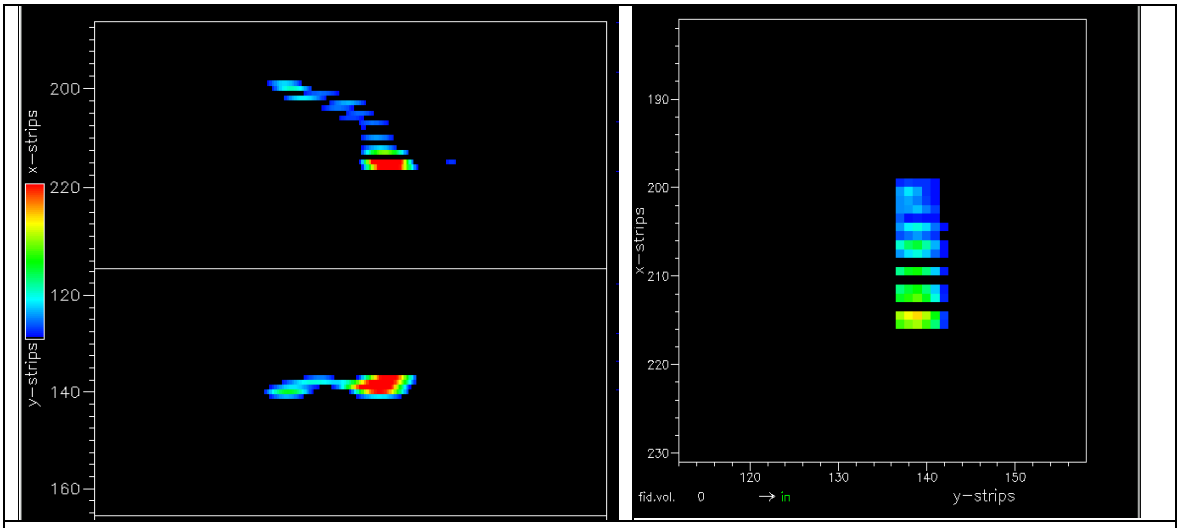

Fig.82. A 190 keV electron. xz projection (left top), yz projection (left bottom) and xy projection (right) are shown

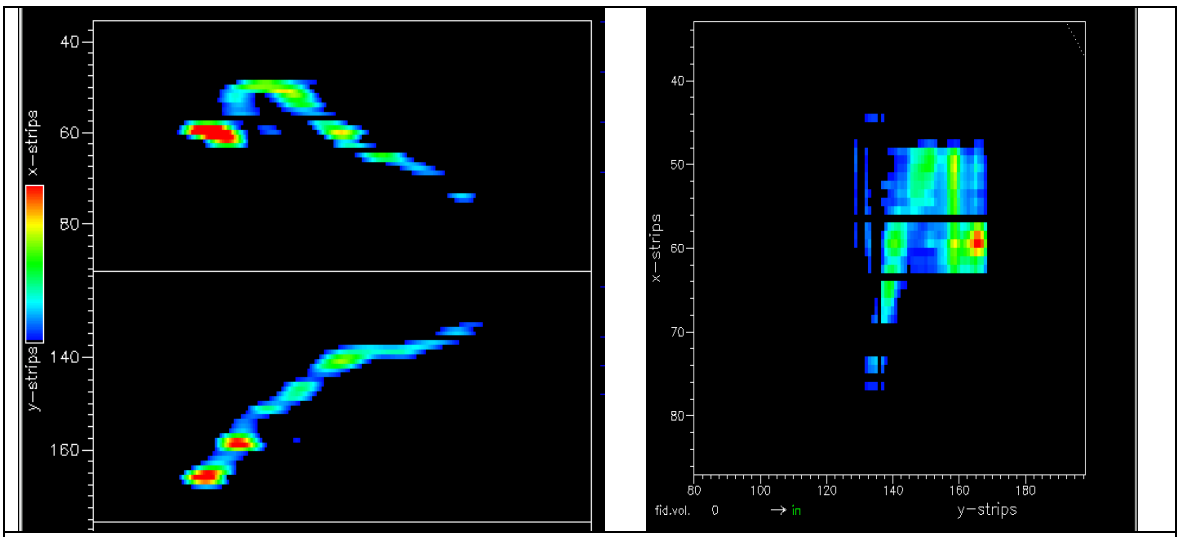

Fig.83. A 500 keV electron. xz projection (left top), yz projection (left bottom) and xy projection (right) are shown.

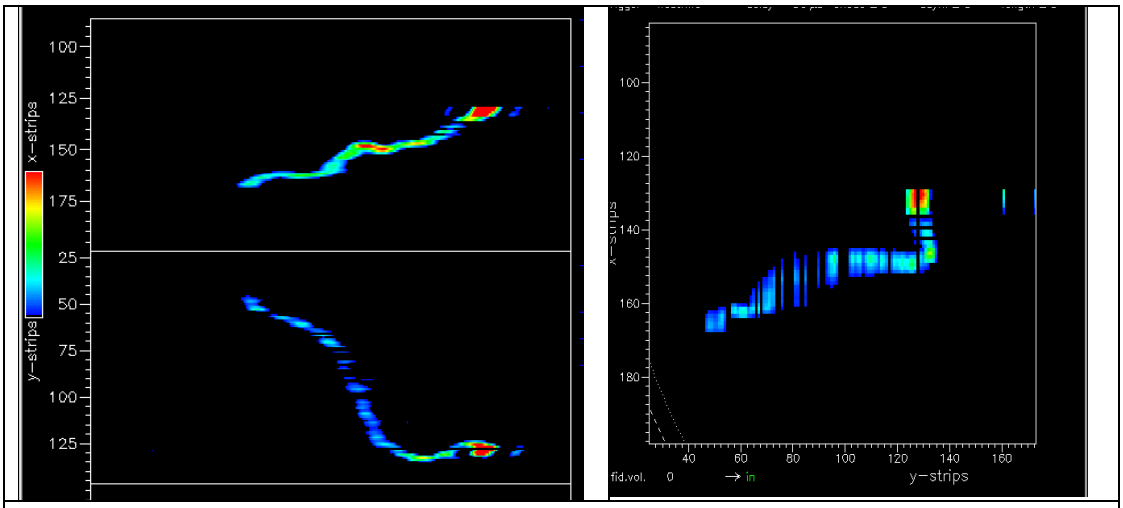

Fig.84. A 700 keV electron. xz projection (left top), yz projection (left bottom) and xy projection (right) are shown.

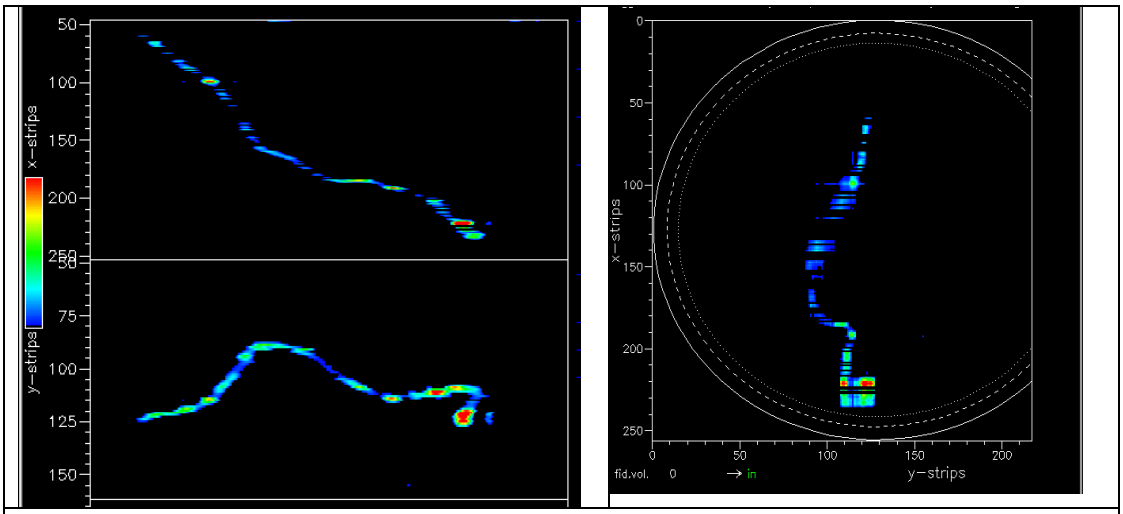

Fig.85. A 1100 keV electron. xz projection (left top), yz projection (left bottom) and xy projection (right) are shown.

Background events

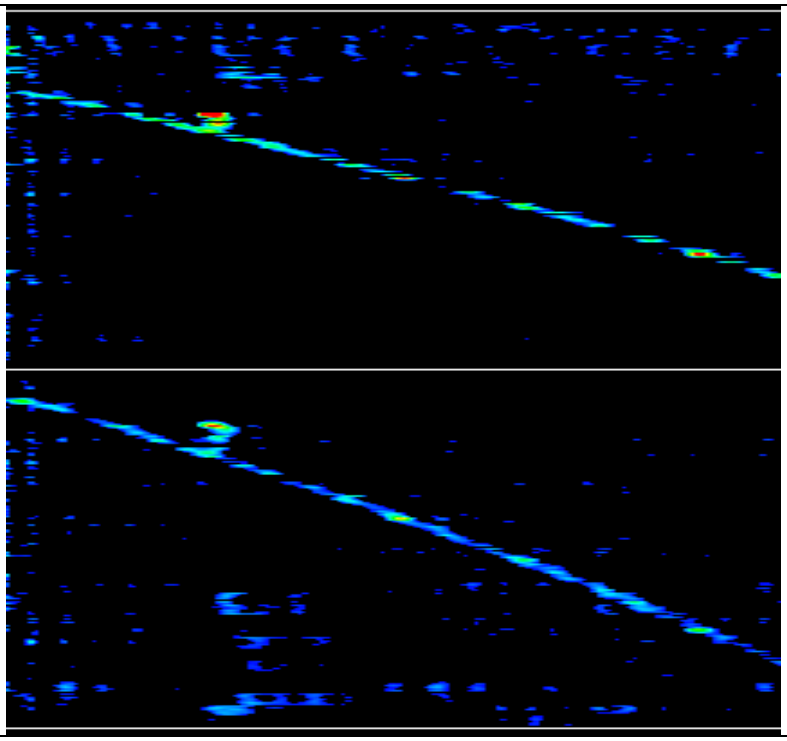

Fig.86. The *xz* (top) and *yz* projections (bottom) of a cosmic muon producing one delta electron.

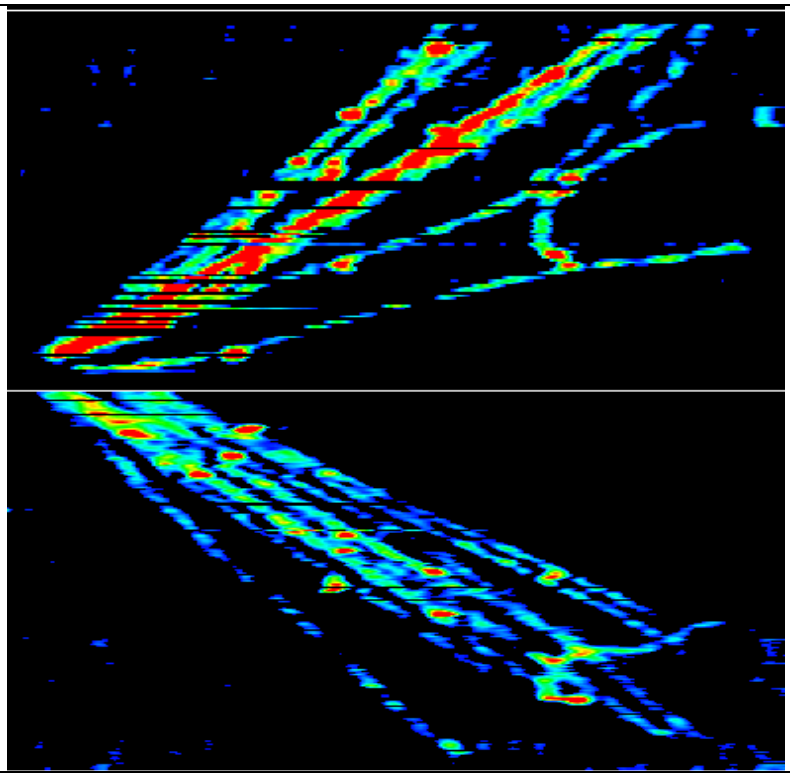

Fig.87. An electromagnetic shower.

IV.5. Global acceptance

The various acceptances are derived from the simulations and compared with the data for the 1-bar period.

The global acceptance of the visual scan analysis for 1-bar is defined in the same way as one for 3-bar (Cf. III. 2)

IV.5.1. Acceptance of the visual scan

IV.5.1.1. Acceptance in-out

The average **acceptance in-out** is found to be **0.90 ± 0.06** from the scanning of the simulated electrons with a slight energy dependence, but larger statistical errors, at energy above 800 keV (fig.88).

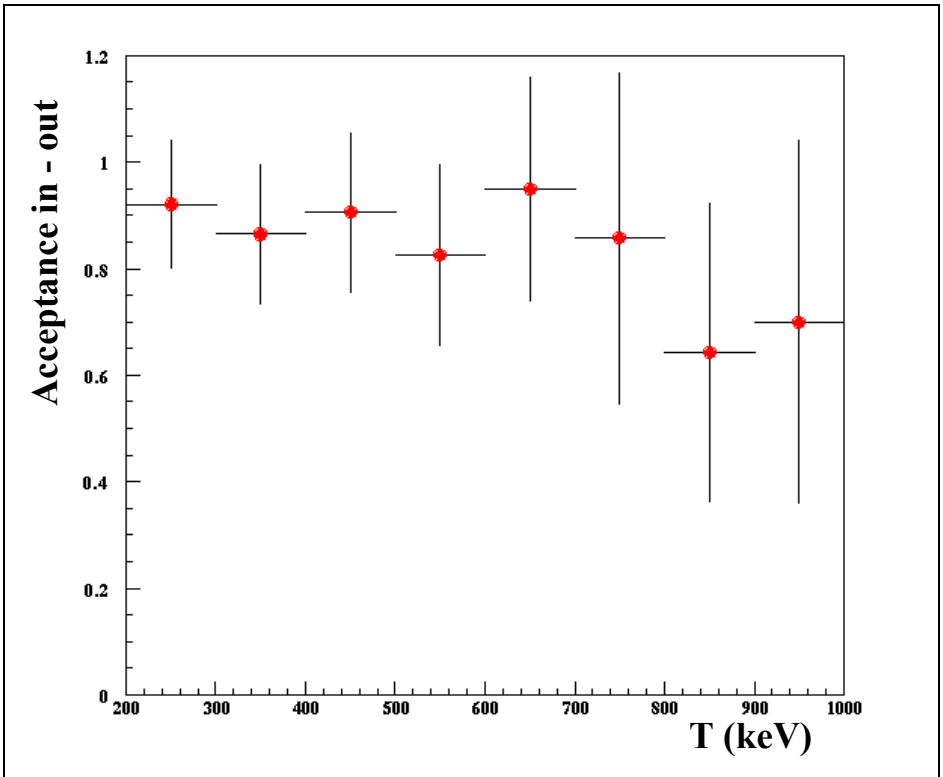

Fig.88. Acceptance in-out (1-bar) as a function of energy

IV.5.1.2. Signal acceptance ($E_\nu > 0$)

The **signal acceptance** is found to be **99.9 %** from the scan of the simulated events.

IV.5.1.3. Geometrical acceptance

The **geometrical acceptance** (Cf. III.1.2) is derived from the scan of real data and is found to be **0.90 ± 0.007**. This acceptance is due to the fact that for some events being perpendicular to the *x* and *z* (*y* and *z*) axis the initial vertex could not be reconstructed (10 % of the total number of events).

IV.5.1.4. Acceptance θ_{det}

Due to the increased activity from the anode side only the electrons from the cathode side will be considered in the analysis, hence the **acceptance θ_{det} = 50 %.**

$$\textbf{Acceptance}_{\textbf{visual scan}} = (\textbf{Acc.}_{\textbf{in-out}}) \times (\textbf{Acc. } E_\nu > 0) \times (\textbf{Acc.}_{\textbf{class}}(\textbf{Acc.}\theta_{det})$$

$$\textbf{Acceptance}_{\textbf{visual scan}} = 0.90 \times 0.999 \times 0.9 \times 0.5$$

$$\textbf{Acceptance}_{\textbf{visual scan}} = 0.41 \pm 0.05$$

IV.5.2. Containment efficiency of the detector at 1-bar pressure

To estimate the containment efficiency of the detector (42 cm fiducial radius) at 1- bar we simulated electrons **randomly** in the TPC with energies between 1**0 keV** and **1200 keV**.

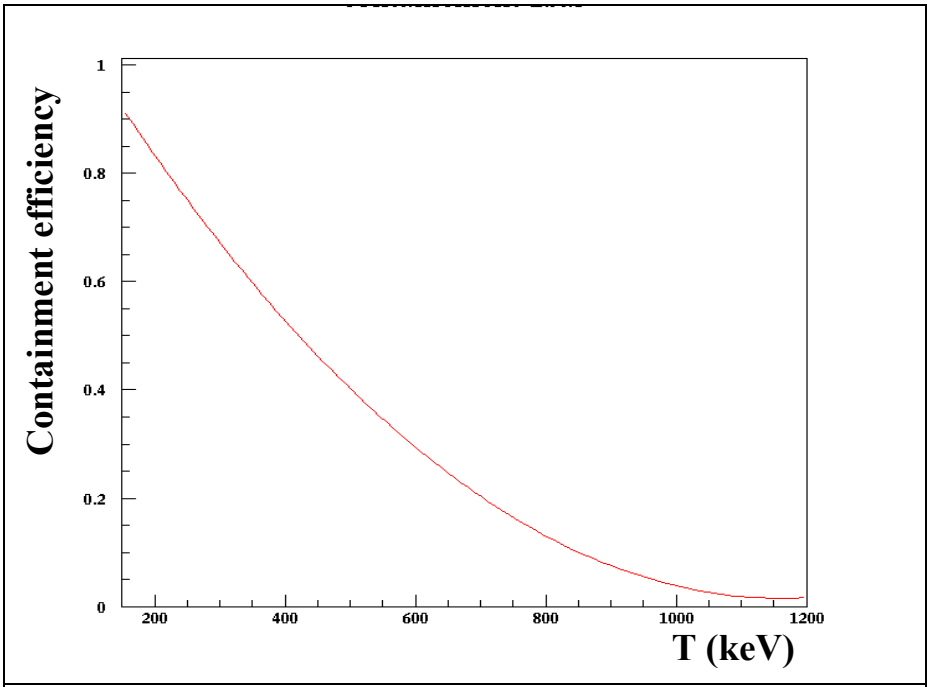

Fig.89. Containment efficiency as a function of energy

The containment efficiency of the detector for 1-bar pressure is shown in fig.89. It varies with energy: at 200 keV it is 85 %, at 400 keV it is 50 % and at 800 keV it is 10 %.

IV.5.3.Expected rate

The expected rate for the 1-bar period is calculated in the same way as for the 3-bar period (CF.III.2.3).

The parameters that are changed are:

the number of the target electrons ($1x10^{27}$ target electrons for 1 bar of CF4)
the detector resolution ($E^{0.57}$)
the acceptance of visual scanning (0.41)
the containment efficiency of the detector

The Monte Carlo error on the expected rate comes from the uncertainties in: the low energy part of the neutrino spectrum (10 %), reactor neutrino flux (5 %), energy calibration (5%), detector containment (3%), events with weird topologies (10 %) and acceptance of visual scan (5 %). The total uncertainty on the total expected rate is 38 %.

The total expected rate above 200 keV assuming zero magnetic moment is found to be 2.9 ± 1.1 counts for 5.3 days (fig.90), which gives 0.55 ± 0.2 counts per day (cpd).

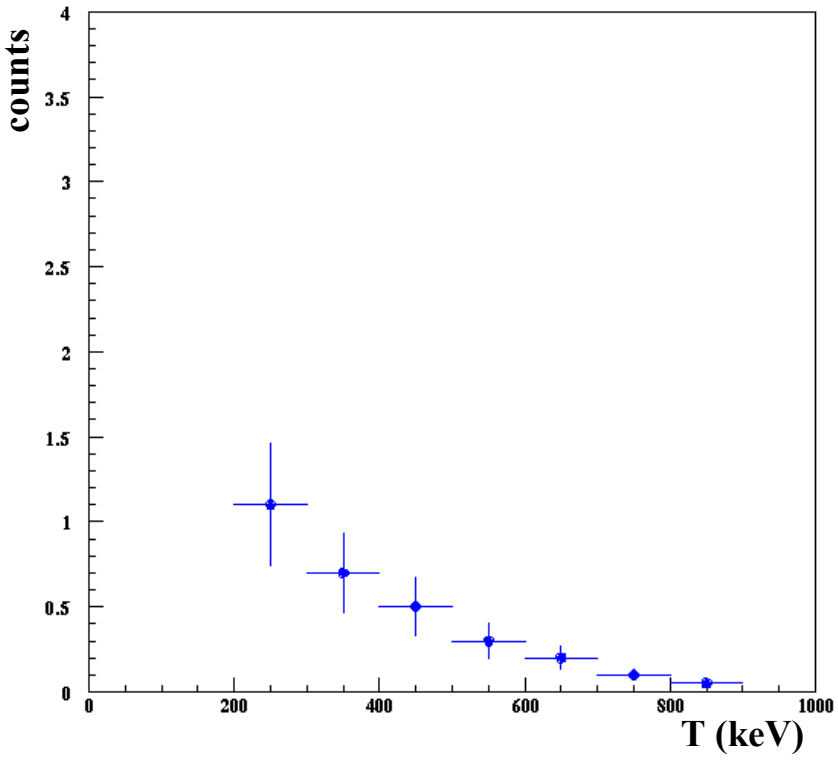

Fig.90. The expected electron recoil spectrum above 200 keV predicted for weak interaction alone.

IV.6. Background during the 1-bar period

IV.6.1. Krypton background

The presence of ^{85}Kr in the gas would lead to an increase of the background below 700 keV during the 1-bar period. However, it schould be distributed homogenuosly in the gas and is eliminated by the two analyses (forward - backward and forward –normalized background).

The estimated activity of ^{85}Kr is 0. 15 Bq [36].

IV.6.2. Background from the anode

The cos θ_{det} distribution of all contained single electrons shows an excess coming from the anode side (cos $\theta_{det} < 0$) in fig.91.

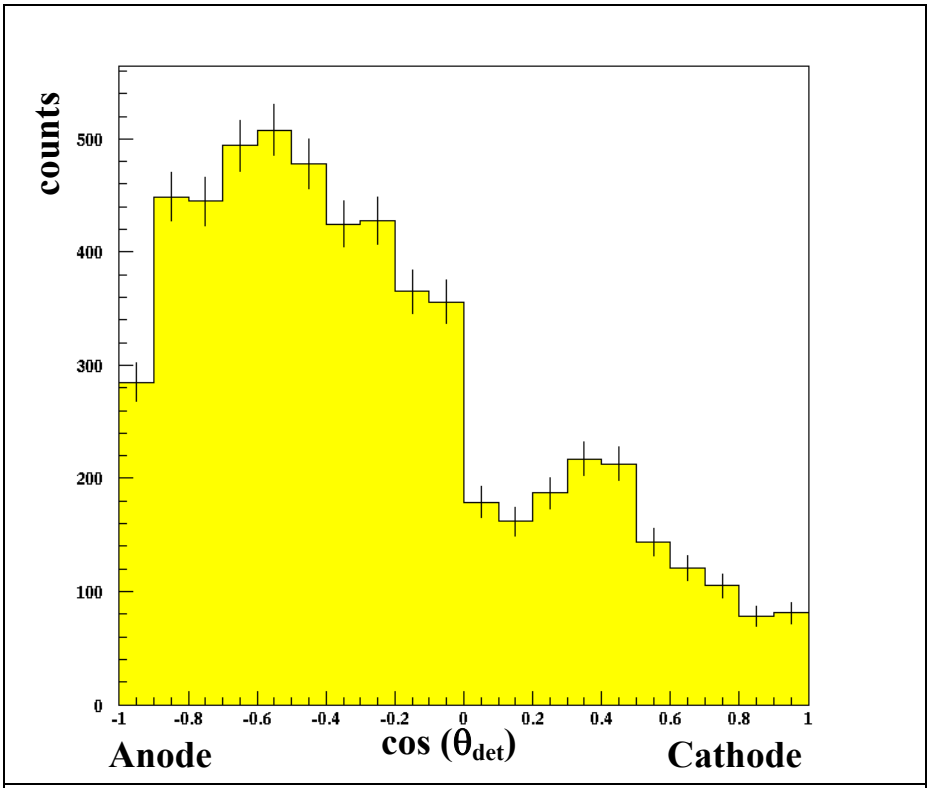

Fig.91. Cos(θ_{det}) distribution of the fully contained single electrons.

To avoid the background originated from the anode itself we select as in the other analysis only the electrons from the cathode side: cos $\theta_{det} > 0$ ($\theta_{det} < 90°$). This results in a smaller acceptance (50 %), but better selection of neutrino candidates.

IV.6.3. Background in the source direction

We use the same definition of the source and antisource cones (Cf. III.3.4 and fig.39) as before in order to examine the background in the source direction in 1-bar period.

IV.6.3.1. φ_{det} distribution and cos(θ_{rea}) distributions of the source and anti source electrons

In the source: φ_{det} *(10°; 90°)* and antisource: φ_{det} *(-180°; -100°)* cones there are only background electrons.

The φ_{det} distributions of the source and antisource electrons are given in fig.92.

The smaller acceptance in the region of $\varphi_{det} = \pm 90°, 0°, \pm 180°$ was already explained (Cf. III.1.2.1) and results from the events perpendicular to *x* and *z*, or *y* and *z* axis (which are classified in the class ‘’other 1’’).

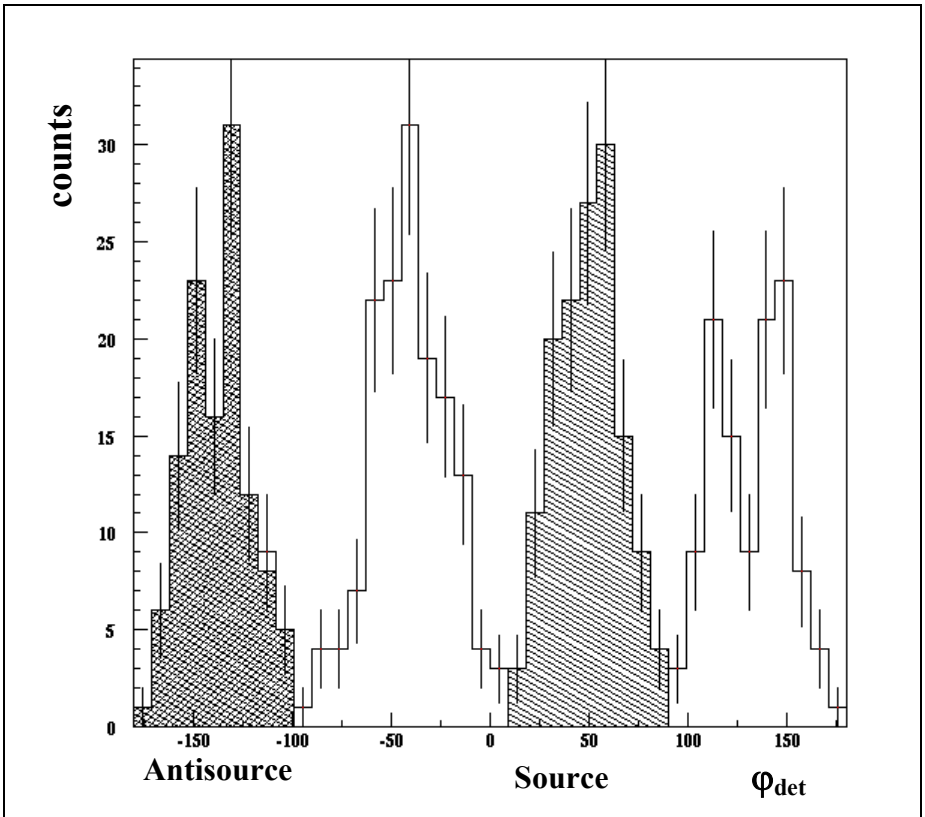

Fig.92. The φ_{det} distribution of antisource electrons (left) and source electrons (right).

The *cos* (θ_{source}) distributions of the source and antisource electrons are shown in fig.93.

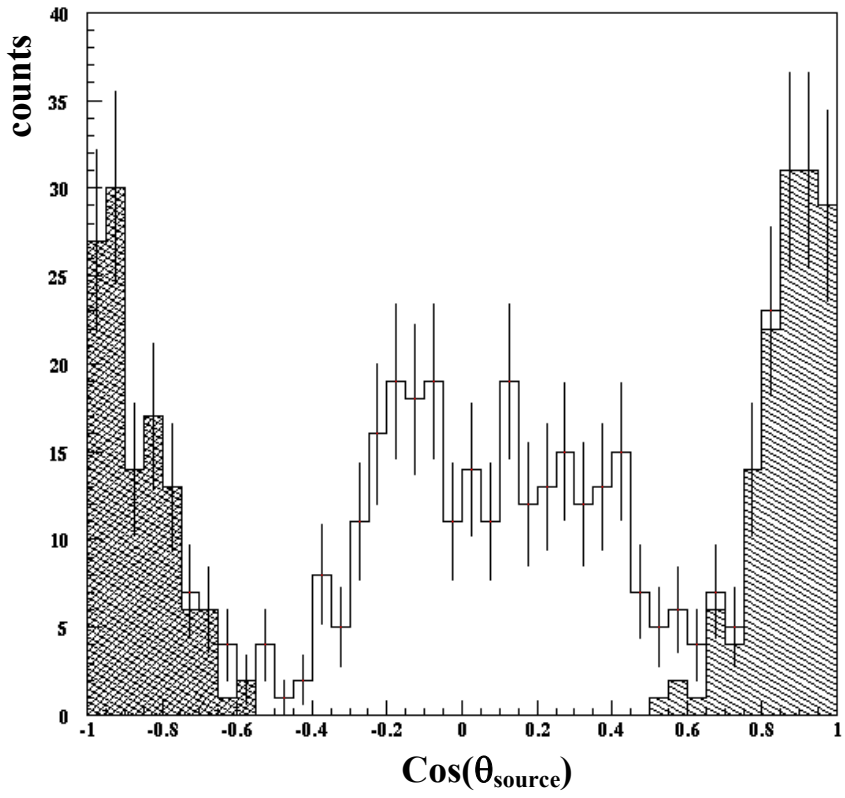

Fig.93. The $\cos(\theta_{source})$ distribution for source electrons (right) and antisource electrons (left)

The smaller acceptance of $cos\ (\theta_{source})$ in the regions of $\pm 0.7 \pm 0.1$ could be explained taking as an example the electron in fig.29.

We recall here the definition of θ_{source} (34).

$$\theta_{source} = \arccos \frac{\Delta y \cos \varphi_{source} - \Delta x \sin \varphi_{source}}{\sqrt{(\Delta x)^2 + (\Delta y)^2 + (\Delta z)^2}}$$

$$\varphi_{source} = \varphi_{drea} + 90° \ (\varphi_{drea} = - 46.7°)$$
$$\varphi_{source} = - 46.7° + 90°$$
$$\varphi_{source} = + 43.3°$$

$$cos\ (\varphi_{source}) = 0.73$$
$$sin\ (\varphi_{source}) = 0.69$$

For an electron with $\Delta y \sim 0$ and $\Delta z = 0$, $cos\ (\theta_{source}) \sim +0.7$ ($\Delta x < 0$) or, $cos\ (\theta_{source}) \sim -0.7$ ($\Delta x > 0$) (for an electron with $\Delta x = 0$ and $\Delta z = 0$, $cos\ (\theta_{source}) \sim -0.7$ ($\Delta y < 0$) or, $cos\ (\theta_{source}) \sim 0.7$ ($\Delta x > 0$)).

The number of events difficult to reconstruct at 1-bar is 10 % of the total number of events, resulting in holes in the calculated regions of the *cos* (θ_{source}) distribution and in an accumulation of events in the neighbourhood of these regions (see fig.93).

IV.6.3.2. Energy distributions of the source, antisource and source minus antisource electrons

The energy distributions of the source (141) and antisource (116) electrons are given in fig.94.

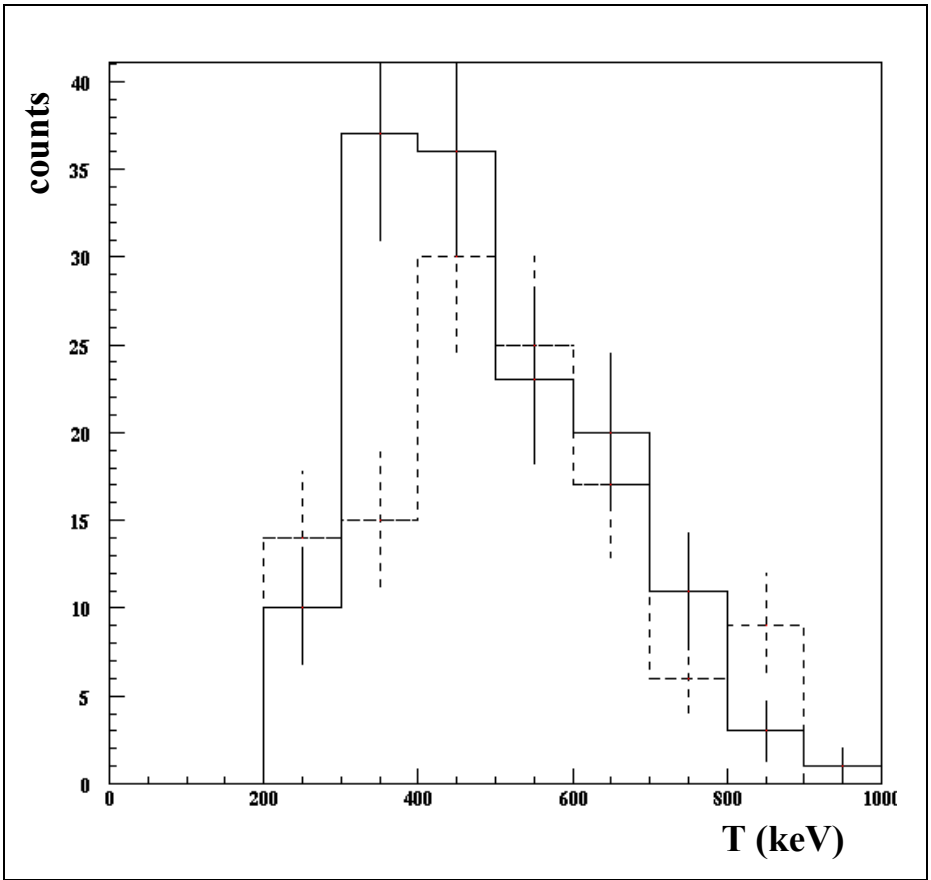

Fig.94. Energy distribution of source (solid line) and antisource (dashed line) electrons.

The energy distribution of the source minus antisource electrons is presented in the fig.95.

The measured asymmetry in the source direction is 25 ± 16 counts for 5.3 days and it results mainly in an accumulation of events in the second channel from 300 keV to 400 keV (see fig.95). Above and below this channel the energy distribution is compatible with zero.

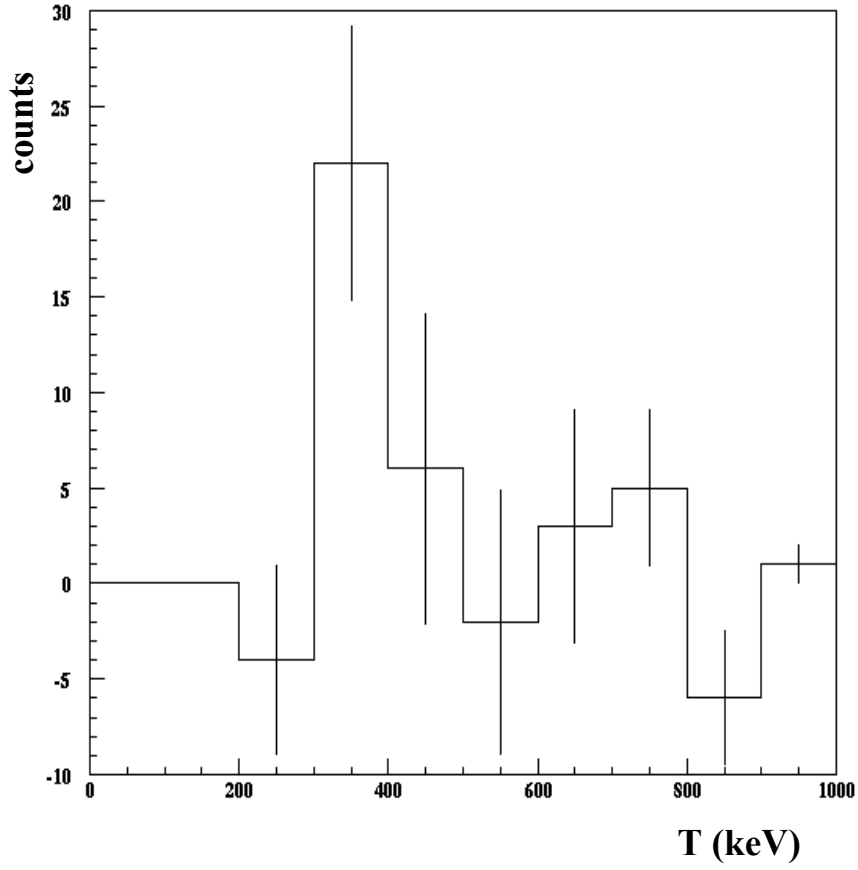

Fig.95. Energy distribution of source minus antisource electrons.

IV.7. 1-bar data analysis

Here we present an analysis of the data, recorded by the MUNU TPC at 1-bar pressure (3.8 kg of CF4).

The data are collected when the reactor is operated, which was shortly after the reactor was shut down.

IV.7.1. Filters for 1-bar data

A software filter is constructed to select single electrons and reject the background from cosmic hits, muons and Compton electrons.

IV.7.1.1. Muon filter

A filter for rejecting muons is applied by comparing of the distributions of two variables *msci* and *dzsci* for electrons and muons.

The distributions of *msci* (puls maximum in Anti Compton detector) for muons and electrons are given in fig.96.

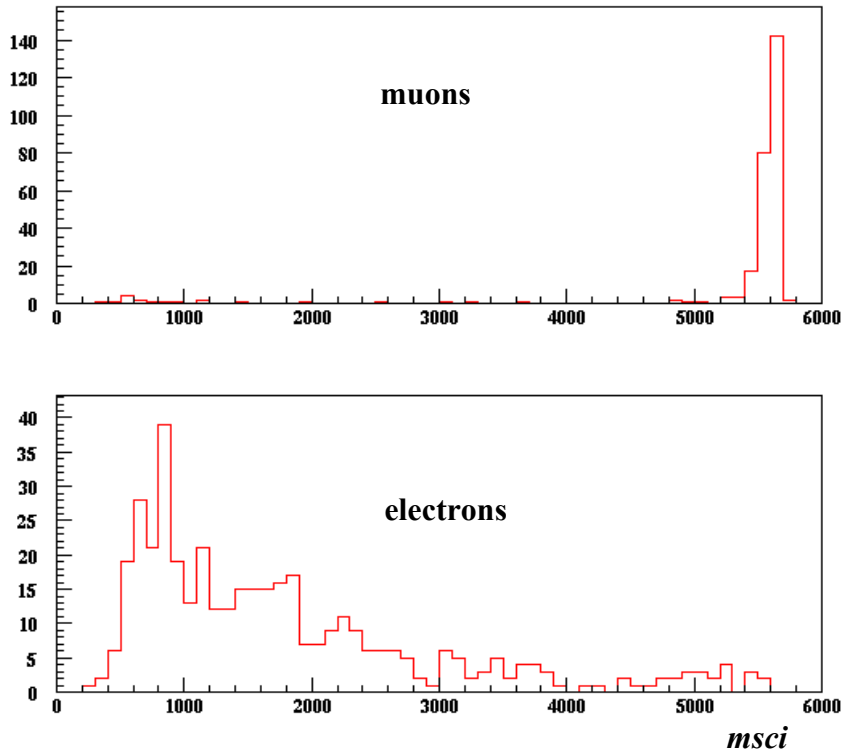

Fig.96. The distribution of *msci* for muons (top) and for electrons (bottom)

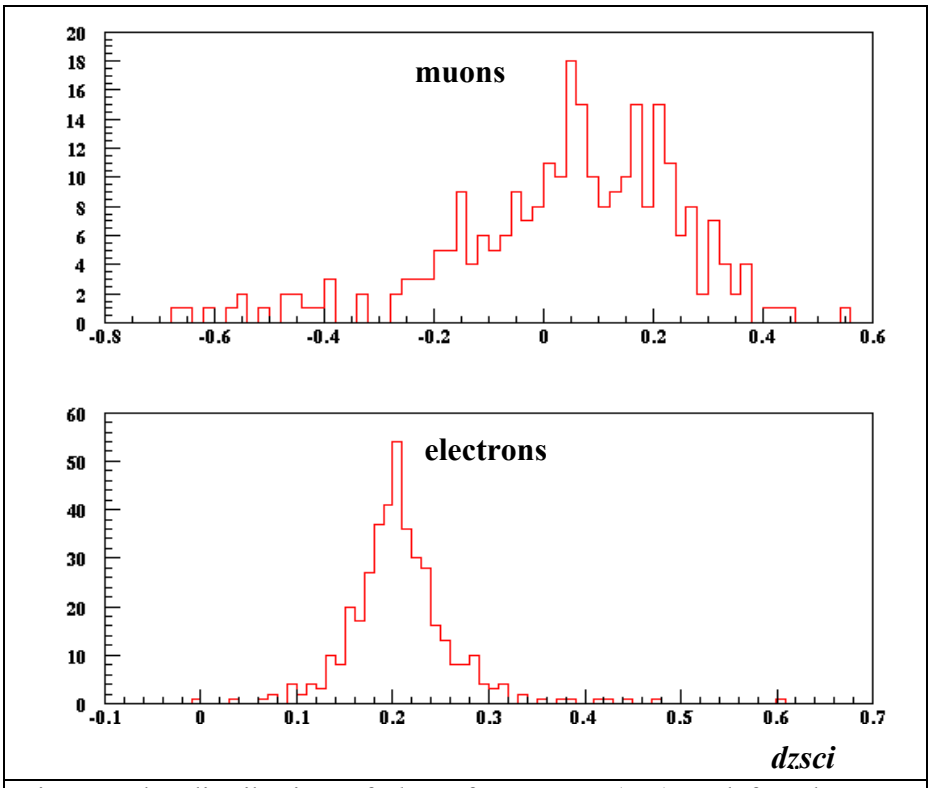

Fig.97. The distribution of *dzsci* for muons (top) and for electrons (bottom)

One can see from fig.96 that for muons, *msci* is larger than *5000*, while for electrons *msci* is below *6000*. To select only electrons *msci* is set at *msci < 5200.*

In Fig.97 are shown the distributions of *dzsci* (asymmetry in the sum of the Photomultipliers) for muons and for electrons. One can see that for the muons *dzsci* is *-0.6 ÷ 0.6,* while for the electrons *dzsci* is *0.1÷ 0.3.*

dzsci is settled as *dzsci > 0.1* for selecting only the electrons.

The efficiency of the muon filter for rejecting muons is found to be 94 %.

IV.7.1.2. Compton electron filter

The filter for rejecting the Compton electrons is constructed in the same way as the muon filter.

To select only electrons we use the difference in the distribution of *qac* (energy deposited in the Anti Compton) for gammas and electrons (see fig.98). One can see that the muons have *qac (0:25000*), while the electrons have *qac = 0*

qac is set at *qac > 500* in order to select only electrons.

The efficiency of the filter for rejecting the Compton electrons is found to be 95 %.

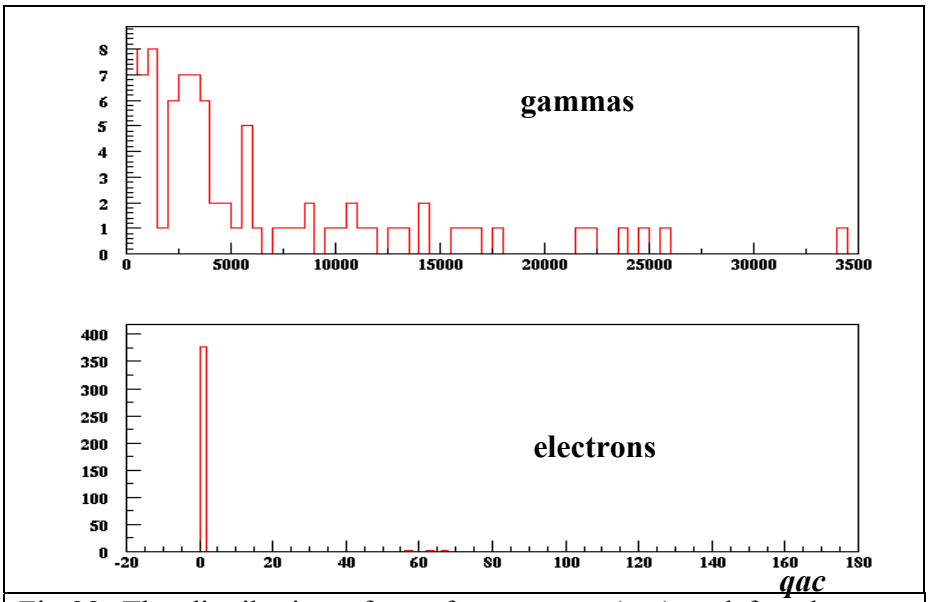

Fig.98. The distribution of *qac* for gammas (top) and for electrons (bottom)

A summary of the above filters is given in the table below

Type of filter	Count rate for 5.3 days	Count rate per sec	Filters efficiency
Anode 70 keV	0.19×10^6	0.42 Hz	-
Software muons	0.17×10^6	0.37 Hz	94%
Software Anti Compton	2.7×10^4	59 mHz	95%
Energy 150 keV	2.6×10^4	57 mHz	-

IV.7.2. Visual scan of events above 200 keV

The events above 200 keV are scanned visually and analysed.

In the analysis as described before we select neutrino candidates and suppress the background, which is mainly due to the cosmic muons, Compton electrons, uncontained and discharges.

The energy distribution of all contained single electrons above 200 keV is given in fig.99.

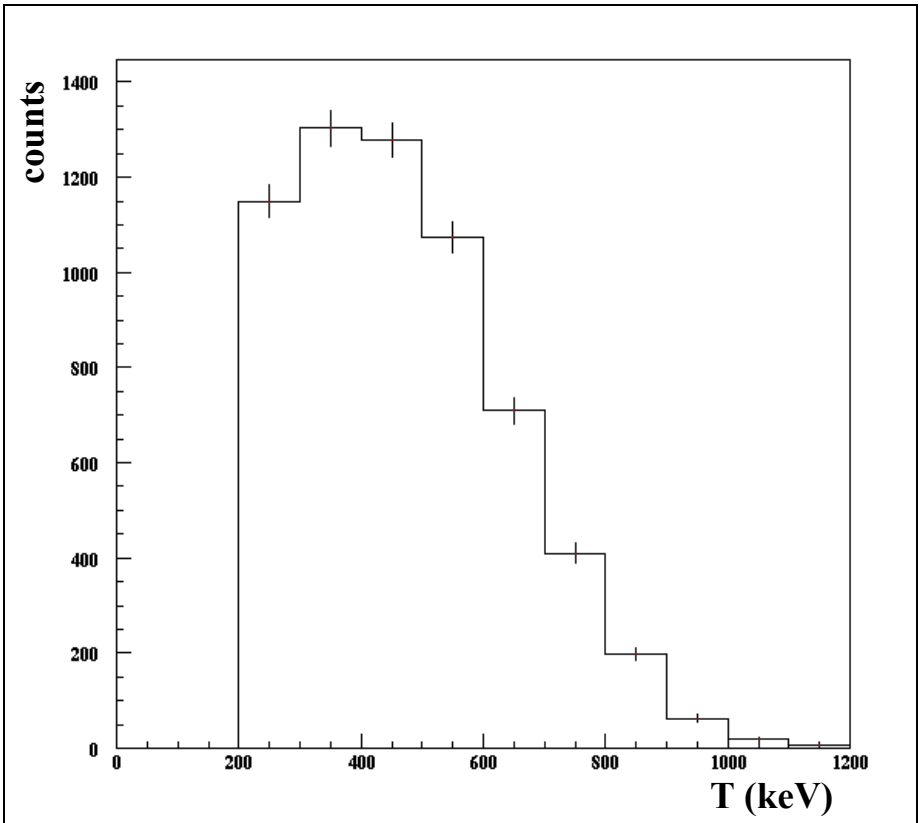

Fig.99. The energy distribution of all contained electrons

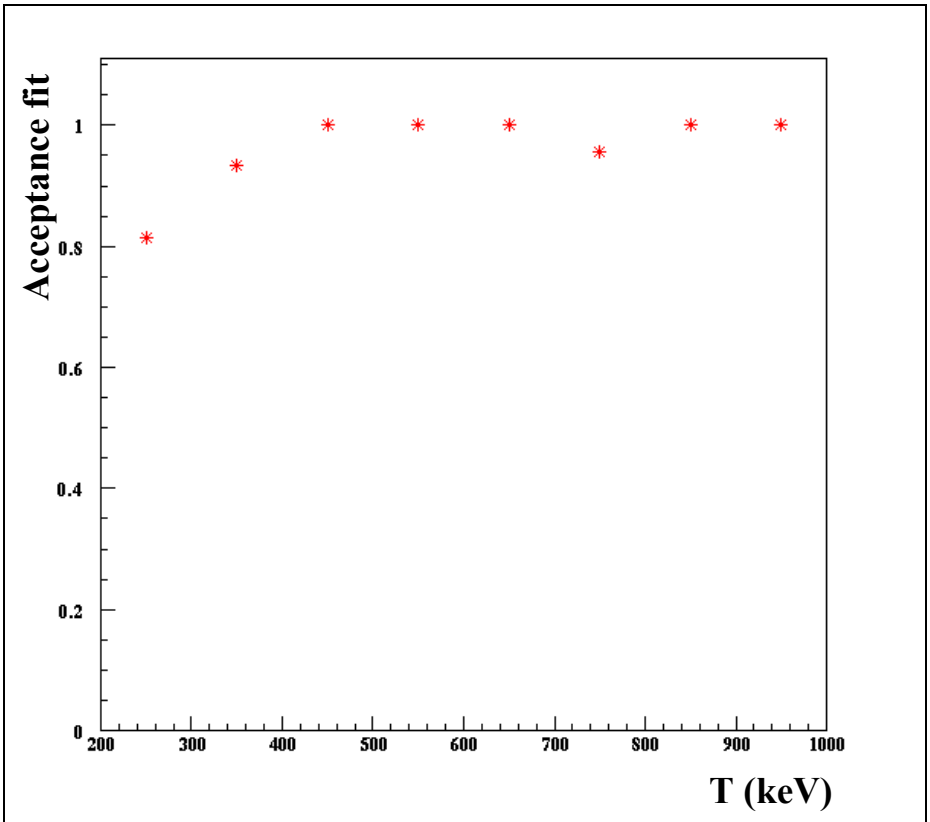

Fig.100. Acceptance fit as a function of energy.

Some electrons in the interval from 200 keV to 400 keV could not be fitted, because they are too small (‘’point like’’).

This results in a smaller acceptance (**Acceptance fit)** for these energies, hence the number of the events in the interval from 200 keV to 400 keV is smaller then the number of the events above 400 keV.

All of the results presented later on are corrected with respect to the following numbers of acceptance fit**:** 81.5 % at 200 keV – 300 keV, 93 % at 300 keV – 400 keV and 100 % above 400 keV (see fig.100); the result is obtained by scanning simulated electrons:

IV.7.3. Forward - Backward analysis

The fully contained ($R < 42$) single electrons from the cathode side ($\theta_{det} < 90$ °) are only treated in the forward - backward analysis.

The forward and backward kinematical cones have already been defined (Cf. II.2.1).

In the forward kinematical cone there are the signal - plus - background events, while in the backward kinematical cone only background events.

IV.7.3.1. φ_{det} and cos (θ_{rea}) distributions of forward and backward electrons

φ_{det} distributions of forward and backward electrons above 200 keV are given in fig.101.

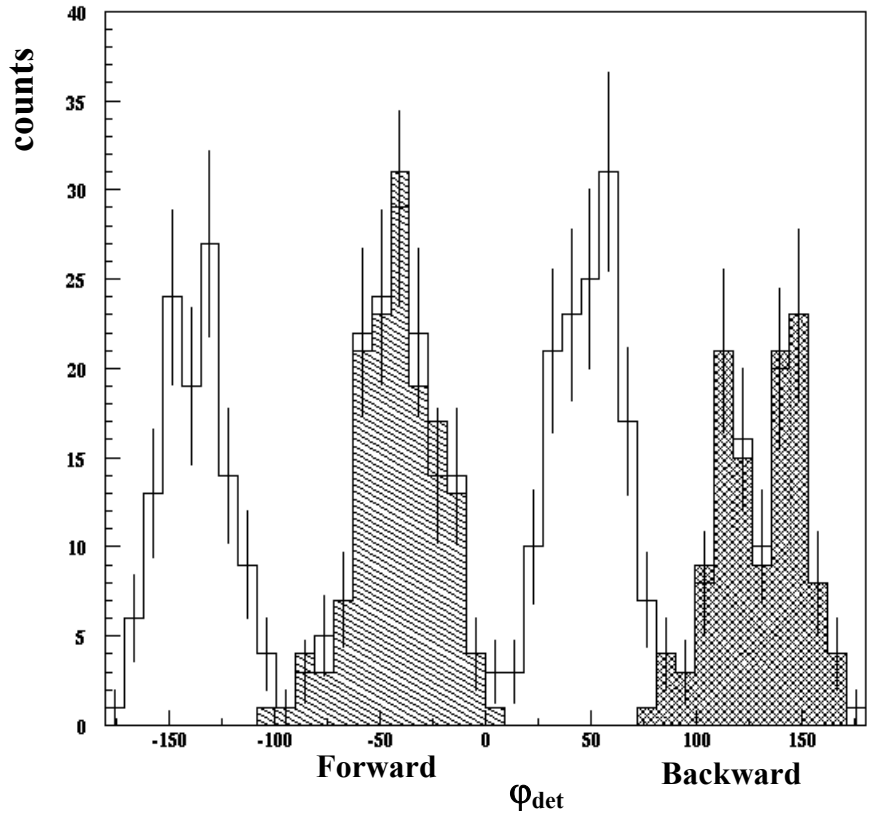

Fig.101. The φ_{det} distribution of contained electrons (solid line). The forward electrons (left) and backward electrons (right) are marked.

Cos (θ_{rea}) distributions of the forward and backward electrons above 200 keV are plotted in fig.102.

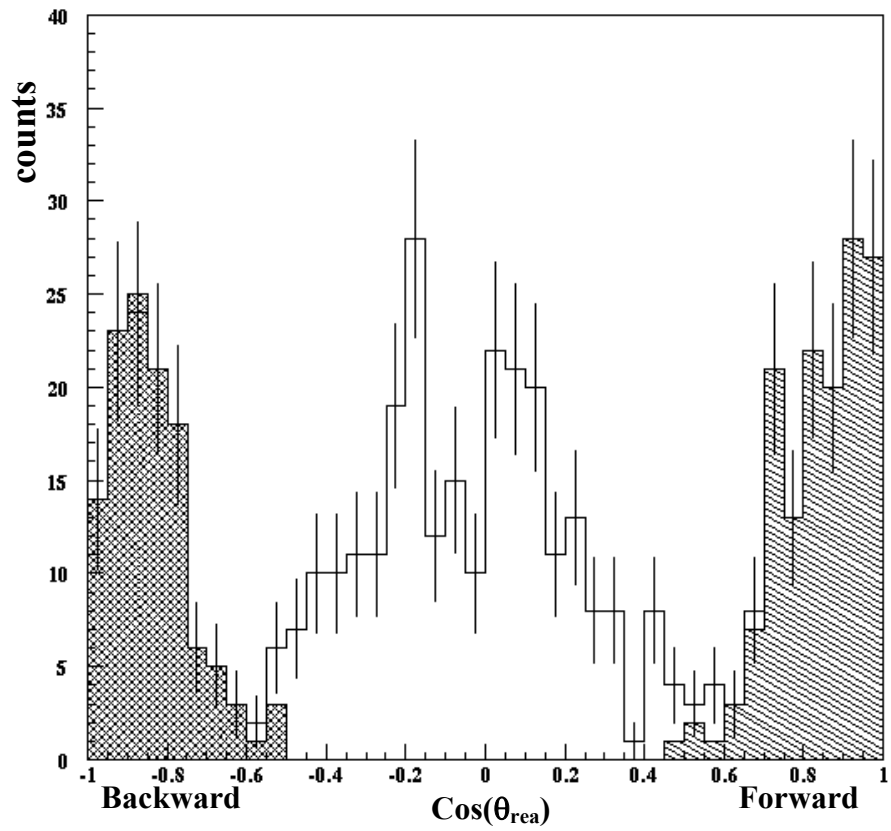

Fig.102. Cos (θ_{rea}) distribution of contained electrons from the cathode (solid line), forward electrons (right) and backward electrons (left).

The smaller acceptance in the $\varphi_{det} = 0°, \pm 90°, \pm 180°$ and $cos\ (\theta_{rea}) = \pm 0.7 \pm 0.2$ was explained already (Cf. III.1.2.).

The number of the events perpendicular to *x* and *z* or *y* and *z* axis however is bigger at 1 bar (10 %) than at 3 bar (4 %). The consequence of the increase of the number of events difficult for reconstruction for the 1-bar period are the larger holes in the φ_{det} and $cos\ (\theta_{rea})$ distributions in the above mentioned regions.

IV.7.3.2. Energy distributions of the forward, backward and forward minus backward electrons

The energy distributions of both forward (151) and backward (124) electrons above 200 keV are given in fig.103. An excess of events is observed in the forward direction.

The energy distribution of the forward minus backward electrons is shown in fig.104.

The integral of forward minus backward is 27 for 5.3 days, which gives 5.1 ± 3.1 cpd.

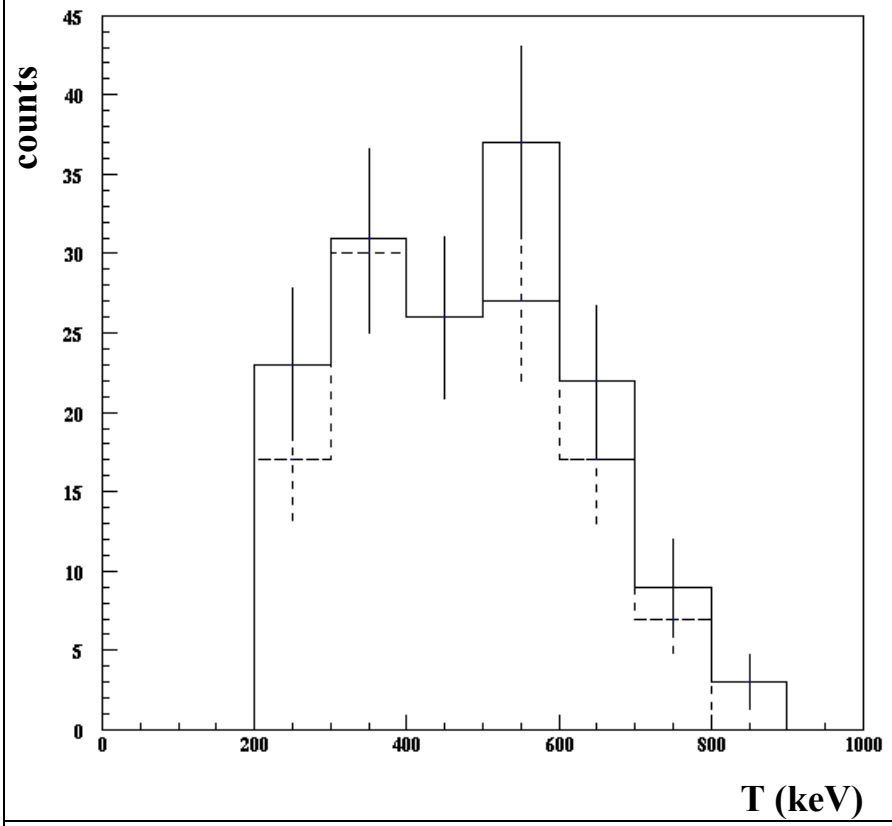

Fig.103. Energy distribution of the forward (solid line) and backward (dashed line) electrons.

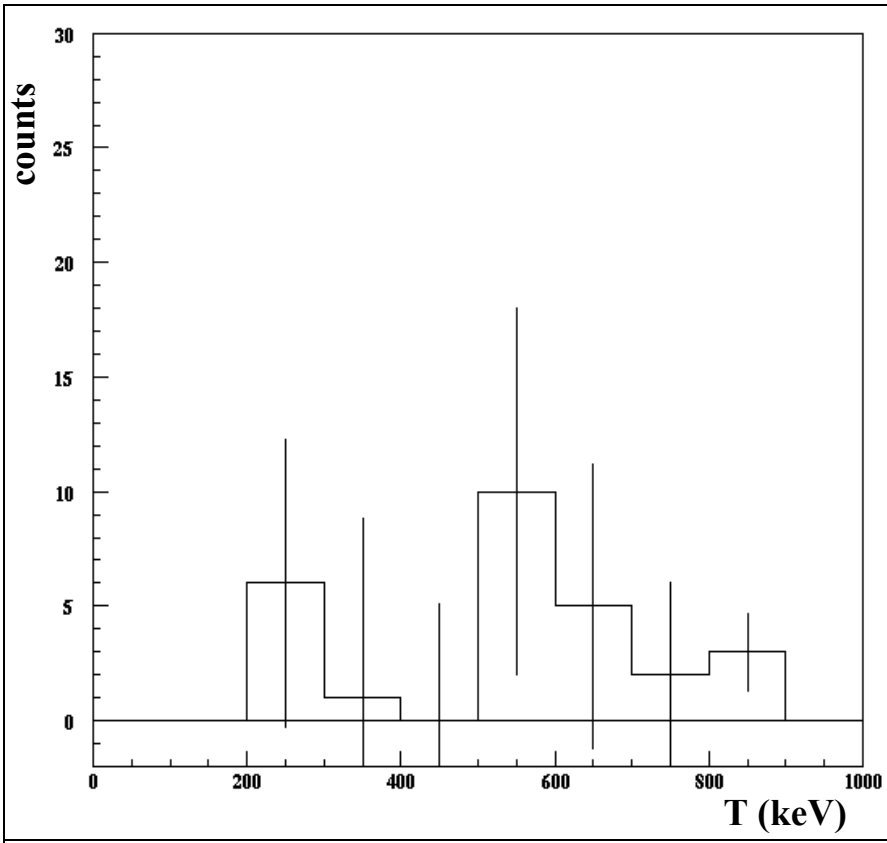

Fig.104. Energy distribution of forward minus backward electrons.

IV.7.3.3. χ^2 analysis

The measured 5.1 ± 3.1 cpd and the predicted 0.55 ±0.2 cpd, Cf. IV.5.3 spectra are shown in fig.105.

The χ^2 method is described in (Cf. III.4.3.3) for minimization of the errors and comparison of both spectra.

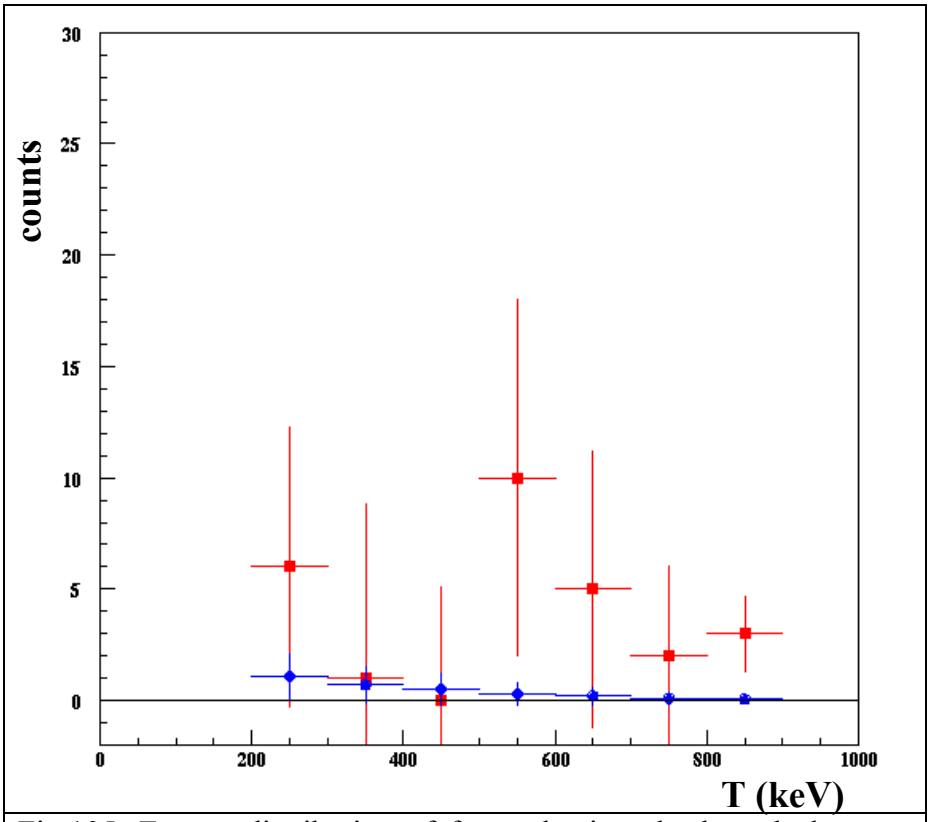

Fig.105. Energy distribution of forward minus backward electrons (red rectangles) as compared to the weak interactions $\mu = 0$ (blue circles)

To calculate the χ^2 we divide the region between 200 keV and 900 keV into 7 channels of 100 keV and vary μ^2 as a free parameter. Thus the number of degrees of freedom (d.o.f.) is 6.

The result of the χ^2 (μ^2) analysis for electron energy above 200 keV is shown in fig.106.

The minimum χ^2 is found to be 4.87. The best fit is χ^2_{min} / d.o.f = 4.87 / 6 = 0.81.

We find a 68 % confidence interval of $\mu^2 = 3.42 \pm 3.54 \times 10^{-20}\ \mu^2_B$ and at 90 % C.L. $\mu^2 = 3.42 \pm 5.78 \times 10^{-20}\ \mu^2_B$ (see fig.106.). These results are compatible with a 1vanishing magnetic moments.

After the renormalization of the above results to the physical region of μ^2 ($\mu^2 > 0$) we find the limits:

$\mu < 2.87\ (2.36) \times 10^{-10}\ \mu_B$ at 90 % (68 %) C. L.

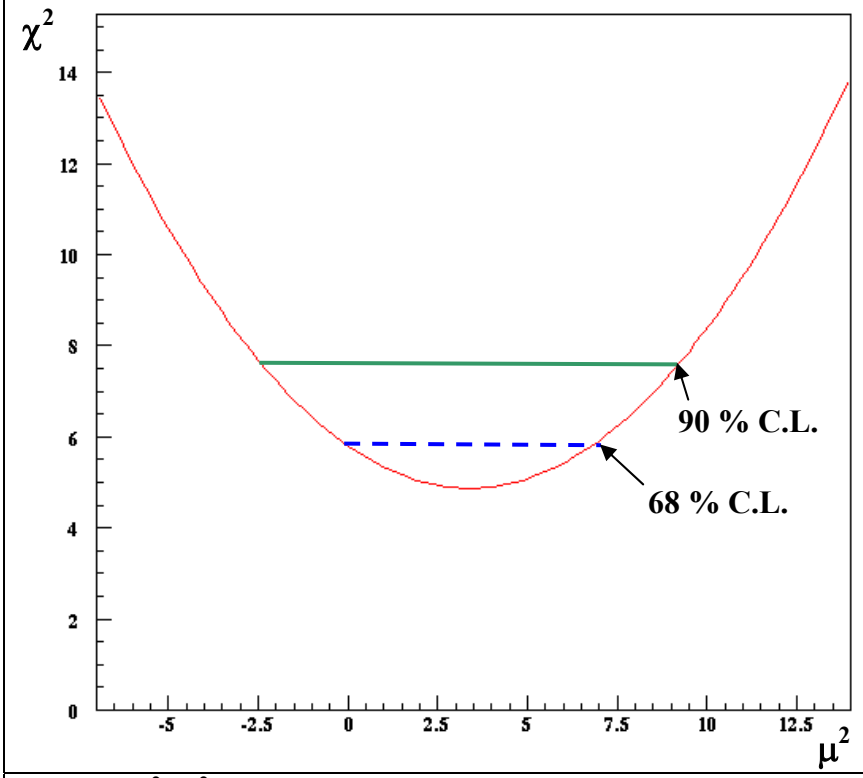

Fig.106. χ^2 (μ^2). 90 % C.L. (line) and 68 % C.L. (dashed line) are shown.

The larger limits in comparison to the ones obtained in the 3-bar data analysis are due to the larger statistical uncertainties at low energies.

IV.7.3. Forward Normalized Background Analysis

We perform here the same analysis that has been presented already in the paragraph III.4.4.

With this analysis we estimate better the background originating from the gas itself and we are able to reduce the statistical errors.

The four kinematical cones are already been defined (Cf. III.4.4.): forward, backward, source and antisource.

In the forward cone there are signal plus background events, while in the source, antisource and backward cones there are only background events.

To avoid an overlap of the contained electrons the four kinematical cones are defined in the following intervals of the φ_{det} angle (see fig. 107):

- antisource electrons φ_{det} = [–180 ; –100]
- forward electrons φ_{det} = [–100 ; 10]
- source electrons φ_{det} = [10 ; 90]
- backward φ_{det} = [90 ; 180]

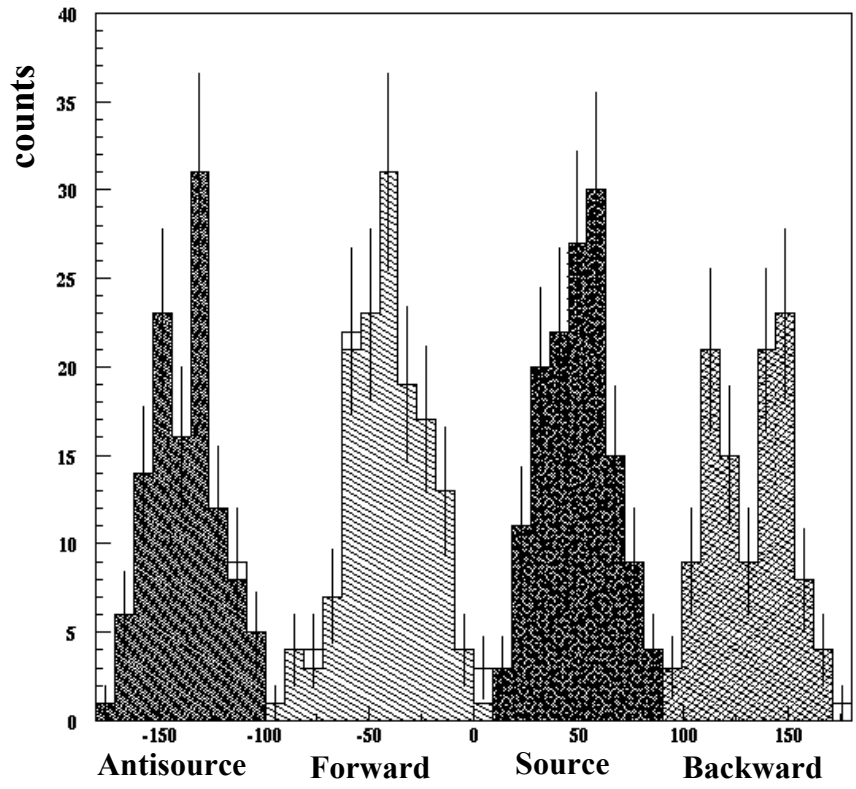

Fig.107. φ_{det} distributions of antisource, forward, source and backward electrons (from left to right).

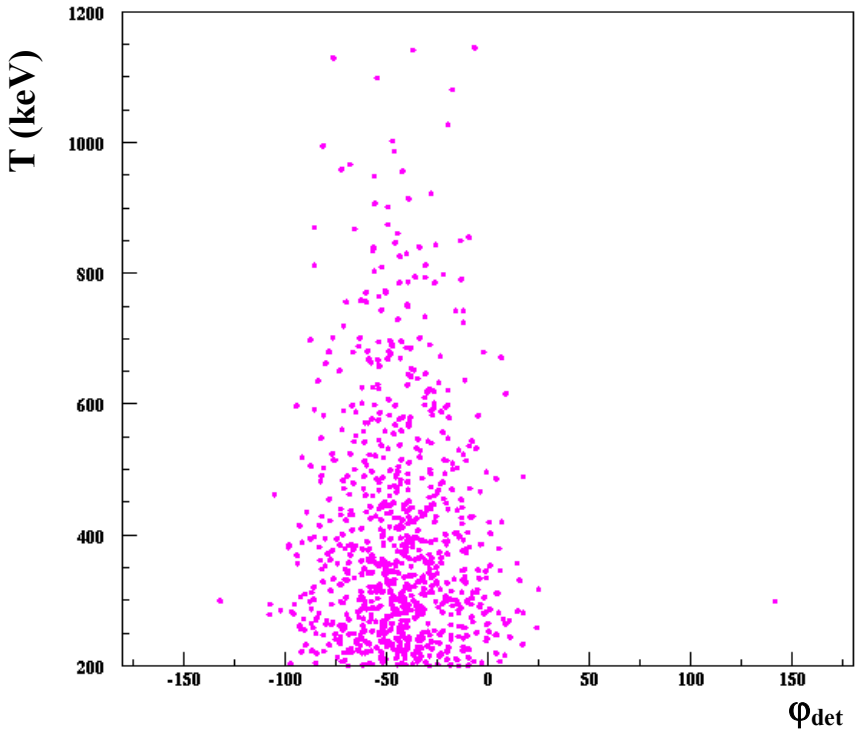

Fig.108. MC simulation of φ_{det} as a function of energy (T) for forward electrons (from neutrino electron scattering)

The angular cut of angle φ_{det} = [−100 ; 10] has an acceptance of 98.6 % above 200 keV, determined from Monte Carlo simulations of the forward electrons (see fig.108).

From the above definition of the cones we can see that the volume of the forward cone is bigger than the volume of each of the three other cones. However, the larger angle of the forward cone (55 °) has an error of a few percent and it will not change the normalization result presented above. The latter result from an estimate of the reactor-off data with the same definition of the cones volume: in the forward cone (55 °) are found 8.2 cpd, which has to be compared with 8.6 cpd in the normalized background cone (42 °).

IV.7.3.1. Energy distributions of forward, normalized background electrons and forward minus normalized background electrons

The number of normalized background electrons in each energy interval (from 200 keV to 900 keV) is obtained using eq.39. The errors for normalized background electrons are calculated according to eq.40.

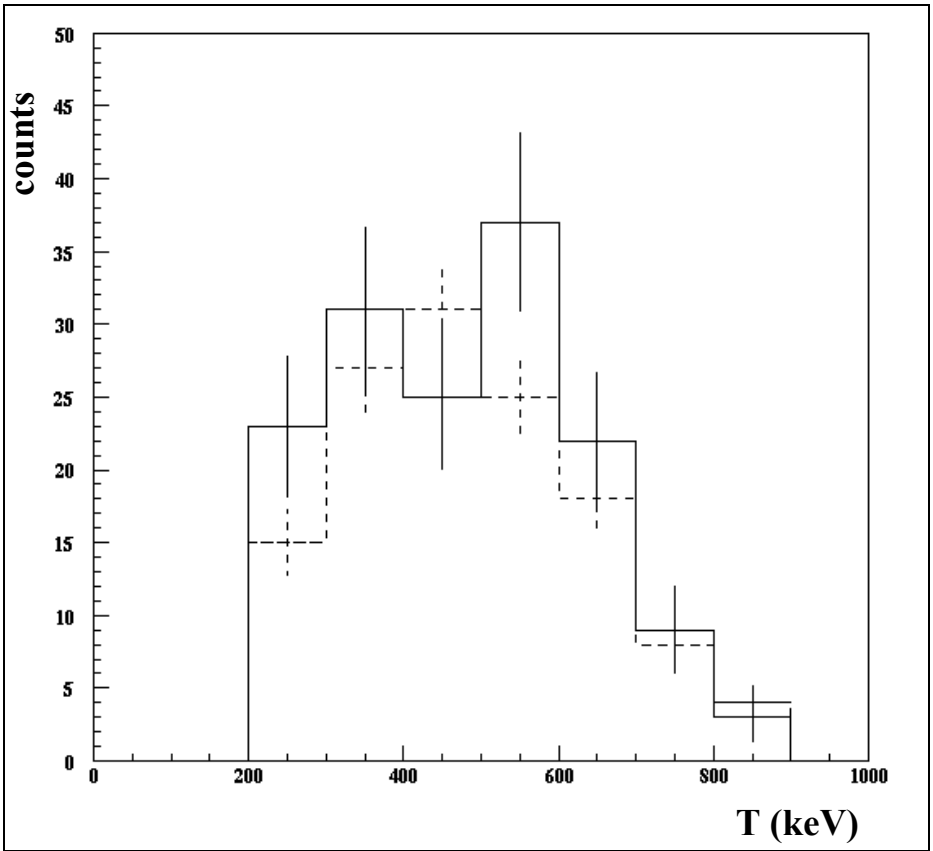

Fig.109. Energy distribution of forward (solid line) and normalized background (dashed line) electrons

The analysed normalized background electrons from eq.39 is given by

$$(146_{\text{source}} + 120_{\text{antisource}} + 118_{\text{backward}}) / 3 = 128_{\text{normal background}}$$

The energy distributions of forward (150) and normalized background (128) events above 200 keV are shown in fig. 109.

The measured signal is calculated according to (eq.41). The errors on the signal are calculated using eq.42.

The energy distribution of the difference of forward electrons and normalized background electrons is given in fig.110.

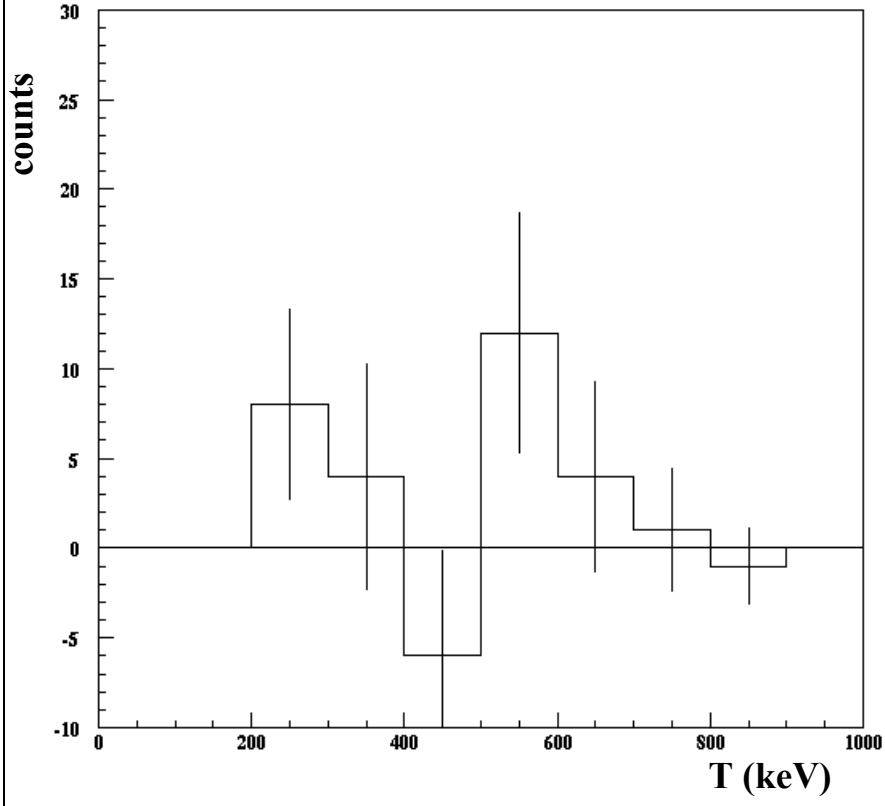

Fig.110. The energy distribution of forward minus normalized background electrons

The total forward - minus - normalized background rate above 200 keV is 22 counts for 5.3 days, which gives 4.1 ± 2.6 cpd. This result is compatible with the earlier obtained with forward – backward analysis (5.1 ± 3.1 cpd); but in this case the estimation of the background is better and the statistical errors are smaller.

IV.7.3.2. χ^2 analysis

Finally we compare the measured result (4.1 ± 2.6 cpd) with the expecting from weak interaction alone *(*0.55 ± 0.2 cpd) (see fig.111).

We divide the region between 200 keV and 900 keV into 7 channels of 100 keV.

The result of the χ^2 (μ^2) for electron energies above 200 keV is presented in fig.112.

The minimum of χ^2 is found to be 5.26. The best fit is $\chi^2_{min}/\ d.o.f.$ = 5.26 / 6 = 0.87.

For minimum χ^2, the squared magnetic moment μ^2 is 3.96 x 10^{-20} x μ^2_B.

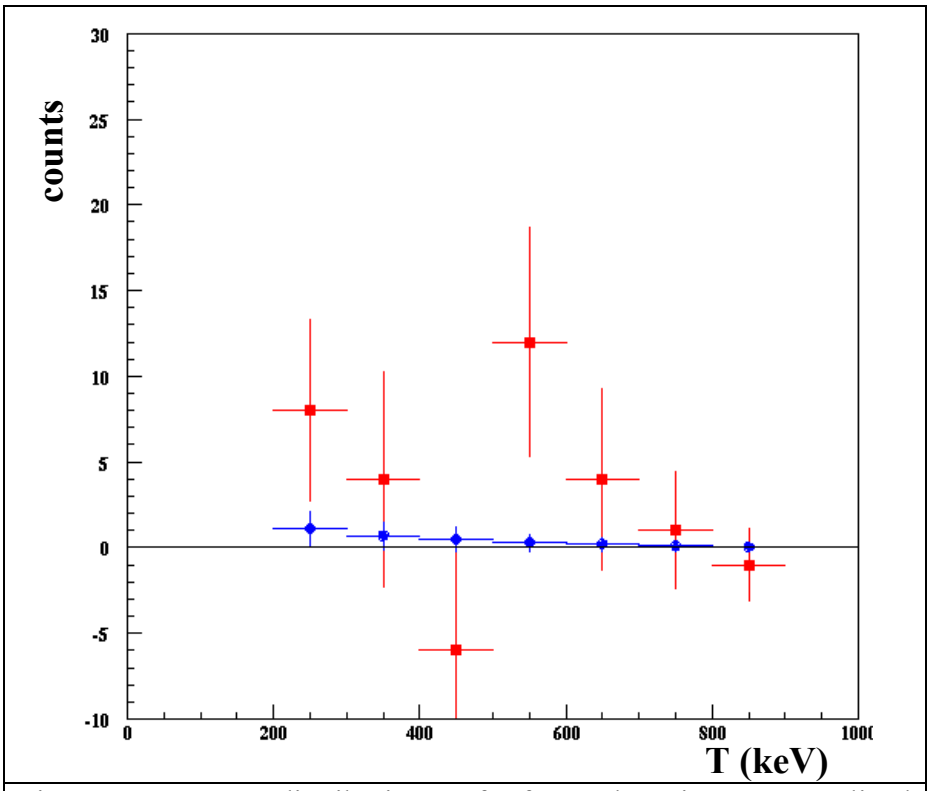

Fig.111 Energy distribution of forward minus normalized background electrons (red rectangles) as compared to the purely weak interaction μ = 0 (blue circles).

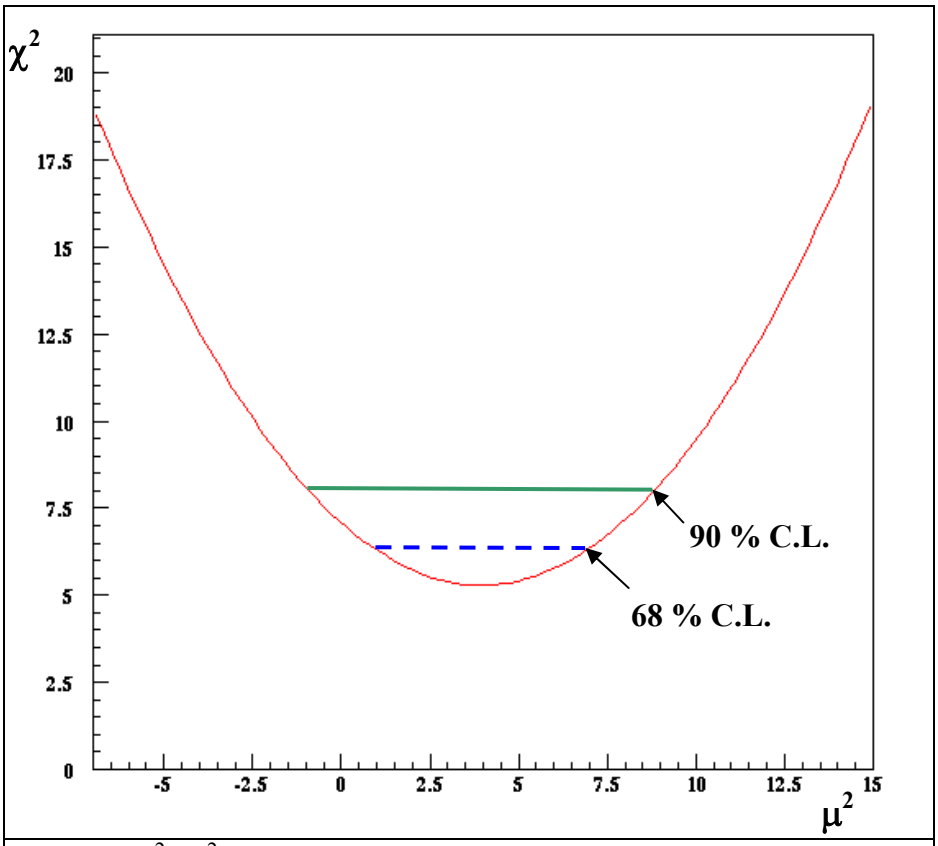

Fig.112. χ^2 (μ^2). 90 % C.L. (line) and 68 % C.L. (dashed line) are shown.

At 68 % confidence interval we find $\mu^2 = 3.96 \pm 2.96 \times 10^{-20}\ \mu^2_B$ and at 90 % confidence interval $\mu^2 = 3.96 \pm 4.84 \times 10^{-20}\ \mu^2_B$ (fig.112). This is consistent with zero magnetic moment.

After renormalization of the above results to the physical region of μ^2 *($\mu^2 > 0$)* we find the limits:

$\mu < 2.81\ (2.36) \times 10^{-10}\ \mu_B$ at 90 % (68 %) C. L.

The limits obtained with the forward - normal background analysis are compatible with those obtained with the forward - backward analysis, but with smaller statistical errors and better background estimation. However, they are still larger than the limits obtained in the 3-bar data analysis. The explanation of the latter is due to the larger uncertainties of the neutrino spectrum at the low energies and the larger statistical errors.

Conclusion

In this work we presented analyses of data recorded by the MUNU detector at two different pressures: 1-bar and 3-bar.

For operation of 3-bar and above an energy threshold of 700 keV, the obtained electron recoil energy spectrum is compared with the predicted one with the help of the two analyses namely: Forward-Backward and Forward-Normal Background (which is a completely new analysis).

From these two analyses we can derive the following limits of the magnetic moment of the electron antineutrino:

$\mu < 1.0\ (0.8) \times 10^{-10}\ \mu_B$ at 90 % (68 %) C. L. above 900 keV (Forward-Backward) [41]

$\mu < 0.95\ (0.71) \times 10^{-10}\ \mu_B$ at 90 % (68 %) C. L above 700 keV (Forward-Normalized Background)

We could show here that with the new Forward-Normalized Background analysis one achieves better estimation of background and smaller errors above 700 keV.

Within this work we also showed that at 1bar pressure the MUNU detector can measure and resolve the recoil electrons down to 200 keV energy, i.e. neutrino energy down to 400 keV.

For 1-bar pressure and above 200 keV an electron recoil energy spectrum is obtained and compared with the predicted one with the help of the same two analyses, namely: Forward-Backward and Forward-Normal Background.

From the two analyses above 200 keV we can derived the following limits of the magnetic moment of the electron antineutrino:

$\mu < 2.86\ (2.36) \times 10^{-10}\ \mu_B$ at 90 % (68 %) C. L. (Forward-Backward)

$\mu < 2.81\ (2.36) \times 10^{-10}\ \mu_B$ at 90 % (68 %) C. L. (Forward-Normalized Background)

The larger limits result from the larger uncertainties, larger background and statistical errors in the neutrino spectrum at lower energy (below 1.8 MeV only the calculations exist).

Although the results from the 1-bar analyses are not as good as those from the 3-bar analyses, we could show for the first time a measurement of the neutrino elastic cross section down to 400 keV, i.e. electron recoil energy down to 200 keV.

The energy resolution of the detector at 1-bar is found to be about a factor of two better than the measured at 3-bar.

References

1. C.L. Cowan and F. Reines, Science 124, 103 (1956).

2. The Super - Kamiokande Collaboration, Y. Fukuda et al., Phys. Rev. Lett. 81, 1562 (1998).

3. SNO, Q.R. Ahmad et al., Phys. Rev. Lett. 87, 071301 (2001).

4. Super-Kamiokande, S. Fukuda et al., Phys. Rev. Lett. 86, 5651 (2001).

5. KamLAND, K. Eguchi et al., Phys. Rev. Lett. 90, 011301 (2003).

6. B. Kayser, Phys. Rev. D 26, 1662 (1982).

7. R. E. Shrock, Nucl. Phys. B 206, 359 (1982).

8. J. Beacom and P. Vogel, Phys. Rev. Lett. 83, 5222 (1999).

9. B. W. Lee and R. E. Shrock, Phys. Rev. D 16, 1444 (1977).

10. J. Morgan, Phys. Lett. B 102, 247 (1981).

11. J. Bernstein and et al., Phys. Rev. 132, 1227 (1963).

12. J. M. Lattimer and J. Cooperstein, Phys. Rev. Lett. 61, 23 (1988).

13. R. Barbieri and R. N. Mohaparta, Phys. Rev. Lett. 61, 27 (1988).

14. D. Notzold, Phys. Rev. D 38, 1658 (1988).

15. G. Raffelt, Phys. Rev. Lett. 64, 2856 (1990).

16. F. Reines, H.S. Gurr et al., Phys. Rev. Lett. 37, 315 (1976).

17. The MUNU collaboration, C. Amsler et al., Nucl. Inst. and Meth. A 396, 115 (1997).

18. G. 't Hooft, Phys. Lett. 37B, 195 (1971).

19. P. Vogel and J. Engel, Phys. Rev. D 39, 3378 (1989).

20. V. I. Kopeikin, L. A. Mikaelyan et al., Phys. At. Nucl. 60, 172 (1996).

21. V. I. Kopeikin, L. A. Mikaelyan et al., Phys. At. Nucl. 60, 172 (1997).

22. G. Zacek and et al., Phys. Rev. D 34, 2621 (1986).

23. F. Boehm and et al., Phys. Lett. 97B, 310 (1980).

24. F. von Feilitzsch and et al., Phys. Lett. 118 B, 162 (1982).

25. Schreckenbach and et al., Phys. Lett. 325 (1985).

26. Hahn and et al., Phys. Lett. B 218, 365 (1989).

27. Y. Declais and et al., Phys. Lett. B 338, 383 (1994).

28. B. Achkar and et al., Phys. Lett. B 374, 243 (1996).

29. S. Ishimoto, J. Nucl. Science and Technology 39, 670 (2002).
30. R. B. Nguyen, Thesis Univ. de Grenoble, (1992).
31. V. I. Kopeikin, L. A. Mikaelyan et al., Phys. At. Nucl. 64, 849 (2001).
32. V. I. Kopeikin, Phys. At. Nucl. 66, 500 (2002).
33. J. L. Vuilleumier, University of Neuchatel Private Communication, (2002).
34. The MUNU collaboration, M. Avenier et al., Nucl. Inst. and Meth. A 482, 408 (2002).
35. The MUNU collaboration, C. Amsler et al., Phys. Lett. B 545, 57 (2002).
36. J. M. Lamblin, Thesis Univ. de Grenoble, (2002).
37. A. Tadsen, University of Neuchatel Private Communication, (1997).
38. O. Link, ETH Zürich Private Communication, (2003).
39. M. Abbes and et al., Nucl. Inst. and Meth. A 374, 164 (1996).
40. P. R. Bevington and D. K. Robinson, Data reduction and error analysis for the physical sciences (2003).
41. MUNU collaboration, Z. Daraktchieva et al., Phys. Lett. B 564,, 190 (2003).
42. The TEXONO collaboration, H. B. Li et al., Phys. Rev.Lett. 90, 131802 (2003).
43. The Super - Kamiokande Collaboration, Phys. Rev. Lett. 93, 021802 (2004).
44. G. F. Knoll, Radiation detection and measurement John Wiley&Sons, (1999).
45. J. Busto, University of Neuchatel Private Communication, (2002).
46. C. Cerna, Thesis Univ. de Grenoble, (2001).
47. L. Ounalli, Nucl. Inst. and Meth. A 525, 205 (2004).

Acknowledgements

I would like to particularly thank my thesis advisor, Professor J.-L. Vuilleumier, for accepting me in his group and for his generous support during these four years and guidance of my thesis with inexhaustible enthusiasm and patience.

I wish to express my thanks to Professor J. Busto for helpful discussions, for his constructive remarks and advices during the time he was in our group.

I am very grateful to Dr. F. Juget. He was always available for efficient discussions, being continually tolerant and open-minded.

J. M. Vuilleumier deserves much appreciation for his efficiency and support during all these years. Without his help the 1bar data analysis will not be possible.

I would like to thank Professor V. Zacek for his support and advices during the time he was in our group.

It was an advantage and pleasure to interact with Dr. C. Broggini and Dr. D. H. Koang within the framework of the MUNU experiment.

Finally, I would like to thank my husband, Maren, and my parents who have been always encouraging and supporting me during these years. I would also say excuse me to my daughter, Jasmin, for the time I did not spend with her.